

Oscillatory Computational Networks based on Coupled VO₂ Oscillators via Tunable Thermal Triggering

**Dissertation
zur Erlangung des
Doktorgrades der Ingenieurwissenschaften (Dr. -Ing.)**

der

Naturwissenschaftlichen Fakultät II
Chemie, Physik und Mathematik

der

Martin-Luther-Universität Halle-Wittenberg

vorgelegt von

Herrn Guanmin Li

Gutachter:

Prof. Dr. Stuart S. P. Parkin

Prof. Dr. Kathrin Dörr

Prof. Dr. Kerem Çamsarı

Tag der öffentlichen Verteidigung:
Halle (Saale), 29.09.2025

Zusammenfassung

Traditionelle tiefe neuronale Netzwerke haben in rechenintensiven Aufgaben wie der Musterklassifikation und Spracherkennung große Erfolge erzielt. Der rapide Anstieg des Energieverbrauchs, der für die Durchführung dieser Aufgaben erforderlich ist, macht jedoch die Suche nach recheneffizienteren Netzwerkarchitekturen dringend notwendig. Netzwerke, die auf gekoppelten Oszillatoren basieren, sind von großem Interesse für energieeffizientes Computing. Ein entscheidender Aspekt bei der Entwicklung solcher Technologien ist die steuerbare Kontrolle der Wechselwirkungen zwischen Oszillatoren, die heute durch zusätzliche elektronische Komponenten realisiert wird. In dieser Arbeit wird eine neuartige Methode zur Steuerung der Synchronisation von eng benachbarter Vanadiumdioxid (VO_2) Oszillatoren vorgestellt, die über ein einfaches thermisches Auslöseelement aus VO_2 erfolgt. Der gesamte Energieverbrauch der Oszillatoren ist bei thermischer Kopplung geringer im Vergleich zu der Situation, in der sie unabhängig voneinander oszillieren. Basierend auf solchen Oszillatoren mit aktiver Abstimmung werden experimentell AND, NAND und NOR Logikgatter sowie verschiedene Feuermuster demonstriert, die das Verhalten Spiking Neuron nachahmen. Großskalige Spiking-Neuron Netzwerke, die auf diesen experimentellen VO_2 -Oszillatoren basieren, erreichen eine Genauigkeit von 90% bei der Erkennung handgeschriebener Ziffern aus dem MNIST-Datensatz. Die Ergebnisse dieser Arbeit zeigen einen innovativen Ansatz für Rechenmethoden, die auf Netzwerken von thermisch gekoppelten Oszillatoren basieren.

Abstract

Traditional deep neural networks have gained success in computational heavy tasks such as pattern classification and voice recognition. However, the rapid increase in power consumption to carry out these tasks due to significant amount of data have made it imperative to search for more efficient and novel computational network architectures. Computational network based on coupled oscillators are of great interest for energy efficient computing. A key to develop such technologies is the tunable interaction among the coupled oscillators which today can be realized by additional electronic components. In this thesis, a novel way to control the synchronization of closely spaced vanadium dioxide (VO_2) oscillators via a simple thermal triggering element formed from VO_2 is introduced. The net energy consumed by the oscillators is lower during thermal coupling compared with the situation where they are oscillating independently. Based on such oscillators with active tuning, AND, NAND, and NOR logic gates and various firing patterns that mimic the behavior of spiking neurons are experimentally demonstrated. Large-scale spiking neural networks based on such experimental VO_2 spiking neurons show a 90% accuracy in the recognition of MNIST hand-written digits. The findings in this thesis demonstrate an innovative approach towards computational techniques based on networks of thermally coupled oscillators.

Contents

| | |
|--|-----------|
| List of Figures | I |
| List of Tables | II |
| Chapter 1 Introduction | 1 |
| Chapter 2 Oscillatory Computational Networks | 3 |
| 2.1 Oscillator-based computational network (OCN) | 3 |
| 2.1.1 Fundamentals of OCN..... | 3 |
| Human Brain as Network of Oscillators | 3 |
| General Concept of OCN | 4 |
| 2.1.2 Different types of OCN | 5 |
| Oscillatory Hopfield Network | 5 |
| Oscillatory Reservoir network | 6 |
| 2.1.3 Physical Implementations of Oscillators | 7 |
| LC Oscillator | 8 |
| Ring Oscillator | 9 |
| Spin-based Oscillator | 9 |
| Phase transition-based Oscillator | 11 |
| 2.2 Spiking Neural Network (SNN)..... | 13 |
| 2.2.1 Neural Network Generations..... | 14 |
| 2.2.2 Different Types of Spiking Neurons | 17 |
| The Hodgkin-Huxley (H-H) Neuron Model | 17 |
| The Leaky Integrate-and-fire (LIF) Neuron Model | 18 |
| 2.2.3 SNN Architectures and Algorithms | 20 |
| Unsupervised learning with STDP rule..... | 20 |
| Supervised learning with Surrogate Gradients | 23 |
| Chapter 3 VO₂ Thin Film Preparation and Device Fabrication | 28 |

| | | |
|-------------------------|---|-----------|
| 3.1 | Pulsed Laser Deposition (PLD) | 28 |
| 3.1.1 | Fundamentals of PLD..... | 28 |
| 3.1.2 | Substrate selection..... | 30 |
| 3.1.3 | VO ₂ Deposition parameters..... | 30 |
| 3.2 | VO ₂ Thin Film Characterization | 31 |
| 3.2.1 | XRD measurement | 32 |
| 3.2.2 | XRR measurement | 35 |
| 3.2.3 | AFM measurement..... | 36 |
| 3.3 | Single VO ₂ Device Set Lithography | 38 |
| 3.4 | VO ₂ 2.5D Crossbar Array Lithography | 39 |
| Chapter 4 | Thermally Coupled VO₂ Oscillators for Boolean Computation | 45 |
| 4.1 | Scalability of VO ₂ Oscillators..... | 45 |
| 4.2 | Tunable Thermal Triggering..... | 52 |
| 4.3 | VO ₂ Oscillator-based Boolean Logic Gates | 59 |
| Chapter 5 | Spiking Neural Network based on VO₂ Neurons | 64 |
| 5.1 | VO ₂ Oscillators-based H-H Neuron..... | 64 |
| 5.2 | VO ₂ Oscillators-based LIF Neuron..... | 66 |
| 5.3 | Large-scale SNN based on VO ₂ LIF Neurons | 71 |
| Chapter 6 | Conclusion and Outlook | 77 |
| References | | 80 |
| Appendix | | 88 |
| Acknowledgements | | 95 |

List of Figures

| | |
|---|----|
| Fig 2.1. Theta and gamma oscillations coupling mechanisms. | 4 |
| Fig 2.2. Comparison between traditional von-Neumann architecture and oscillator computational network. | 5 |
| Fig 2.3. Oscillatory Hopfield network and reservoir network. | 7 |
| Fig 2.4. Schematic illustration of the LC oscillator. | 8 |
| Fig 2.5. Schematic illustration of the LC oscillator. | 9 |
| Fig 2.6. Spin transfer torque oscillator. | 11 |
| Fig 2.7. Phase transition-based oscillator. | 13 |
| Fig 2.8. The first generation of neural network. | 14 |
| Fig 2.9. The second generation of neural network. | 15 |
| Fig 2.10. The Hodgkin-Huxley neuron model. | 17 |
| Fig 2.11. The leaky integrate-and-fire neuron model. | 19 |
| Fig 2.12. Equivalent electric circuit for the leaky integrate-and-fire neuron model. | 20 |
| Fig 2.13. The architecture of spiking neural network with unsupervised learning mechanism. | 22 |
| Fig 2.11. “The dead neuron” problem and surrogate gradients. | 26 |
| Fig 2.11. The backpropagation through time (BPTT) learning rule. | 27 |
| Fig 3.1. Pulsed laser deposition (PLD) system. | 29 |
| Fig 3.2. Modular architecture of the Bruker D8 diffractometer. | 33 |
| Fig 3.3. Schematic of X-ray diffraction. | 34 |
| Fig 3.4. X-ray diffraction (XRD) measurement of a typical VO ₂ film grown on sapphire [0001] substrate. | 35 |
| Fig 3.5. Schematic of X-ray diffraction (XRR). | 35 |
| Fig 3.6. X-ray diffraction (XRD) measurement of a typical VO ₂ film grown on sapphire [0001] substrate. | 36 |
| Fig 3.7. Atomic force microscopy (AFM). | 37 |
| Fig 3.8. VO ₂ device lithography steps. | 38 |
| Fig 3.9. Typical VO ₂ device after fabrication process. | 39 |
| Fig 3.10. VO ₂ 2.5D array design. | 40 |
| Fig 3.12. VO ₂ 2.5D array second layer morphology. | 42 |
| Fig 3.13. VO ₂ 2.5D array third layer morphology. | 43 |
| Fig 3.14. VO ₂ 2.5D array. | 44 |
| Fig 4.1. ρ - T curves of VO ₂ devices with different sizes. | 46 |
| Fig 4.2. I-V curves of VO ₂ devices with different sizes. | 47 |
| Fig 4.3. I-f curves of VO ₂ devices with different sizes. | 47 |
| Fig 4.4. Driving power of VO ₂ devices with different sizes. | 48 |

| | |
|---|----|
| Fig 4.5. Direct observation of thermal coupling effect with trigger delay time between two coupled VO ₂ oscillators..... | 50 |
| Fig 4.6. Driving power of VO ₂ devices with different sizes. | 50 |
| Fig 4.7. Measurement of trigger delay time for two VO ₂ devices with various device spacing. | 52 |
| Fig 4.8. Thermal coupling strength versus device spacing. | 52 |
| Fig 4.9. Tunable thermal coupling device set geometry. | 53 |
| Fig 4.10. VO ₂ oscillators with tunable thermal coupling strength. | 54 |
| Fig 4.11. Temperature-dependent VO ₂ oscillator characteristics. | 55 |
| Fig 4.12. Single device oscillation waveform at different supply currents and thermal cell voltages..... | 55 |
| Fig 4.13. Double device oscillation waveforms under synchronization and desynchronization situations..... | 56 |
| Fig 4.14. Tunable thermal triggering between two VO ₂ oscillators..... | 57 |
| Fig 4.15. Voltage-mode (V-I) and current-mode (I-V) measurements for a thermal cell..... | 58 |
| Fig 4.16. VO ₂ nano oscillators with tunable thermal triggering. | 59 |
| Fig 4.17. Oscillation states used for Boolean computation..... | 60 |
| Fig 4.18. Logic “0” represented by different oscillation states of VO ₂ device 2. | 61 |
| Fig 4.19. Boolean logic gates based on coupled VO ₂ oscillators with tunable thermal coupling strength. | 62 |
| Fig 5.1. Thermal spike driven VO ₂ oscillation with different firing modes. | 65 |
| Fig 5.2. VO ₂ leaky integrate-and-fire (LIF) neuron. | 67 |
| Fig 5.3. Operation and tunability of VO ₂ leaky integrate-and-fire (LIF) neuron..... | 69 |
| Fig 5.4. Temporal integration function realized by two VO ₂ LIF neurons..... | 69 |
| Fig 5.5. Temporal modulation function realized by two VO ₂ LIF neurons. | 70 |
| Fig 5.6. Experimental neuron potential and fitting of the relaxation process. | 72 |
| Fig 5.7. Experimental neuron potential and fitting of the refractory period. | 72 |
| Fig 5.8. Large-scale spiking neural network based on VO ₂ LIF neurons. | 73 |
| Fig 5.9. Tuning the learning parameter. | 74 |
| Fig 5.10. Training accuracy based on different percentage of defects. | 75 |
| Fig 5.11. 2-layer SNN with 150 VO ₂ LIF neuron. | 76 |
| Fig 6.1. Frequency modulated information transmission in an oscillatory neural system..... | 78 |

List of Tables

| | |
|---|----|
| Table T1. Deposition parameters for different VO ₂ samples. | 30 |
| Table T2. Calculation table of Boolean logic gates. | 62 |

Chapter 1 Introduction

Nowadays, more and more artificial intelligent (AI) technologies are applied in our daily life: Target recognition, natural language processing, auto-pilot and etc. However, traditional computing technique based on von-Neumann architecture falls short of competing with human brain in term of energy efficiency. For a very simple pattern recognition task such as handwritten digits or animals, it takes computer to run at a power of 800 W in order to train the neural network, while human brain needs much lower power for similar tasks [~ 20 W, empirical value]. Such significant difference in power consumption for executing the same task has raised interests and demands to develop next-generation computing architecture that approaches the human brain. Traditional von-Neumann architecture has separated process units and memory units- data needs to be constantly transferred back and forth in sequence between them during every operation, which leads to the additional latency and considerable power consumption. Network of oscillators with inherent dynamical coupling strength, mimics periodic activities of biological neurons in the brain (Chapter 2.1). This oscillatory network can offer faster and more efficient means of computation by their integrated process and memory units, and the ability to process data in parallel [1, 2]. Two critical aspects for the further development of such systems are mutual interactions and the control of the interactions between neighboring oscillators for their synchronization.

Spiking neural networks (SNNs, Chapter 2.2), as a special type of oscillatory computational network, have garnered ever increasing interest in recent years due to their similarity with our own biological system in terms of sparse connections, and better capability to deal with temporal data by its inherent recurrent feature [3 - 5]. As distinct from second-generation ANNs (artificial neural networks) that generate continuous analog outputs, third-generation neurons in SNNs communicate with each other by discrete spikes [6].

Highly interesting oscillators can be formed from strongly correlated oxide materials that display an insulator to metal transition. The controlled oscillation between the low and high resistance states in such materials is possible under an external stimulus such as current, magnetic field, or electric field [7, 8]. Oscillators based on vanadium dioxide (VO_2 , Chapter 2.1.3) are of particular interest since the material undergoes an insulating to metallic phase transition near room temperature [9 - 12]. Coupling between the VO_2 oscillators is essential to the operation of the oscillatory computational network and can be realized either via external

electronic components [13 - 17] or by thermal links [18, 19]. So far, computational schemes based on the phase relationship between oscillators has been the most common technique used in coupled VO₂ networks [14 - 16]. These schemes rely on binary logic where the two states correspond to the phase of the oscillator (0° or 180°) relative to a reference oscillator. However, additional electronic elements are required for generating the oscillation and for tuning the coupling among the VO₂ devices [13 - 19]. This not only increases the complexity of the design of any computational circuit, but also limits the degree of freedom to tune the dynamics of the network during operation.

This thesis offers a simple but effective mean to actively tune the thermal coupling between VO₂ oscillators, without any extra electronic components needed. The effective tuning mechanism introduced in this thesis can generate a multiplicity of synchronous oscillatory states with distinct frequencies and amplitudes for both Boolean-type (logic gates operations) and non-Boolean-type (spiking neural network) computation.

The thesis is organized as follows: Firstly, the basic concepts, working principle of oscillator-based computational network (OCN), and comparison between different implementations of oscillators will be introduced in Chapter 2. Then, spiking neural network (SNN), as one of the OCNs, will be discussed and compared with the previous generations of artificial neural network (ANN). Two types of basic computational nodes from SNN: Leaky integrate-and-fire (LIF) neuron and Hodgkin–Huxley (H-H) neuron, together with the network architecture and training algorithm utilized in this thesis, will also be introduced in this chapter. In Chapter 3, physical deposition of VO₂ thin films, and fabrication process of VO₂ devices will be introduced in details. Afterwards, implementations of VO₂ oscillators for both traditional Boolean logic gates computation (Chapter 4), and unconventional neuromorphic computing based on spiking neural network (Chapter 5) will be introduced. Finally, in Chapter 6, the findings of this thesis will be concluded and further applications with other type of memristor (i.e. magnetic Racetrack memory) will be briefly discussed for outlook.

Chapter 2 Oscillatory Computational Networks

In this chapter the general concepts for oscillator-based computational network (OCN), and different types of oscillators are the basic building block for the network will be introduced and discussed. Spiking neural network (SNN), as a special type of OCN, together with the network architecture and training algorithm that are utilized in this thesis will be studied. Two types of building blocks for SNN: Leaky integrate-and-fire (LIF) neuron and Hodgkin–Huxley (H-H) neuron will also be introduced in this chapter.

2.1 Oscillator-based computational network (OCN)

2.1.1 Fundamentals of OCN

Human Brain as Network of Oscillators

Imagine our brain is a large-scale network formed from oscillators, while each neuron behaves like an oscillator with its own frequency. Neurons don't act in isolation. In the cell assembly theory, Hebb described the formation of neuron groups through the principle “Neurons that fire together, wire together”, and suggested that these assemblies work as units for learning and forming memories [20]. Individual neurons, each with their own activity rhythm, are locally synchronized. These locally assembled neurons act as a unified group, generating a collective rhythm to carry out specific functions, or represent a specific memory pattern.

Oscillations across various frequency bands are strongly evident in different regions of the brain. Extensive research has been conducted on Theta-frequency oscillations (4-8 Hz) in the rodent hippocampus region. It was found that theta band oscillation has a critical impact, particularly on spatial navigation, memory encoding, and retrieval [21]. Gamma oscillations (40 - 80 Hz), which are commonly observed in various regions of the brain, contribute to the encoding and integration of information through precise temporal coordination [22]. The brain performs a complex function through communication among different neuron assemblies. Local gamma oscillations modulated in amplitude by theta oscillations can synchronize and communicate with other regions by phase-phase frequency coupling, cross-frequency phase-amplitude coupling, gamma phase-phase coupling, or cross-frequency phase-phase coupling methods [22], as shown in **Fig 2.1**. Such oscillation-based synchrony is energy-efficient and helps neurons work cooperatively [23].

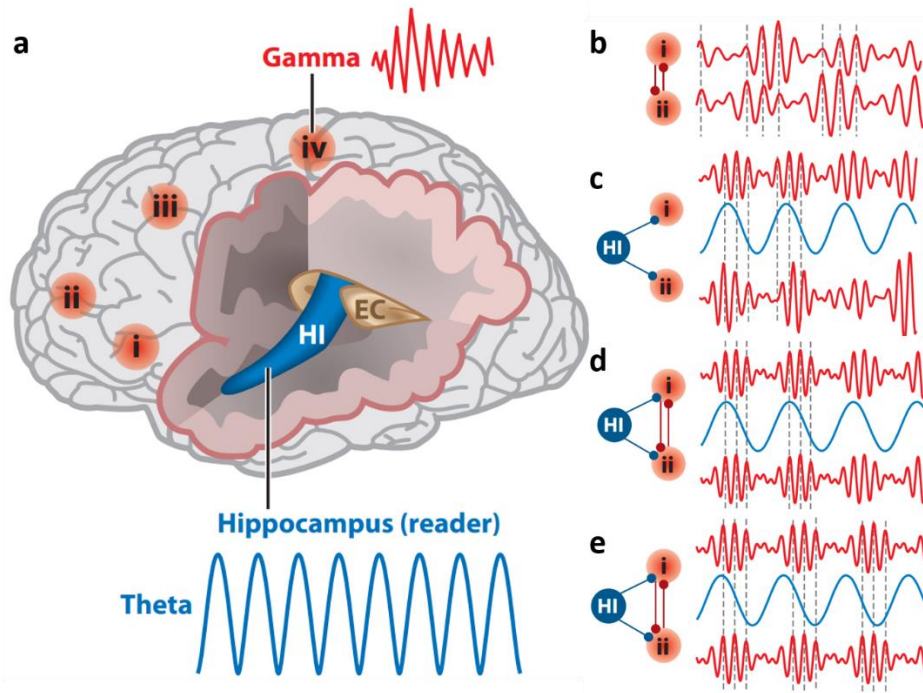


Fig 2.1. Theta and gamma oscillations coupling mechanisms. **a**, Scheme of the brain region that are nested with gamma oscillations and theta oscillations. **b**, Phase-phase frequency coupling between gamma oscillations. Though the two gamma oscillations are not exactly the same, their phases are matched. **c**, Cross-frequency phase-amplitude coupling between gamma oscillation and theta oscillation. Though the phases of gamma-frequencies are not matched, the amplitude of gamma oscillation is regulated by same phase of theta oscillation. **d**, Gamma phase-phase coupling. **(e)** Cross-frequency phase-phase coupling between gamma and theta oscillation. Both the phase of gamma oscillation and theta oscillation are in coherence. Modified from [22].

General Concept of OCN

Inspired by the effectiveness of the human brain, von Neumann in 1957 first proposed the idea of constructing an oscillatory computational network that utilized phase information of the oscillators for computing [24, 25]. It was truly surprising that he already realized the inherent limitations (processing speed, “memory bottleneck” problem, and huge power consumption) of the existing von Neumann computing architecture (proposed by him earlier and named after him) back at that time, which has become the main computing architecture nowadays.

In contrast to the traditional von Neumann architecture, which is based on binary Boolean logic, the information in OCN can be represented by continuous frequencies and/or amplitudes and/or phases of the oscillators [26]. In traditional Boolean machine computational elements (transistor) are working independently, and binary digits flow through each element in sequence. Quite differently, oscillators in the OCN are coupled, and the interaction between them will

converge the whole system simultaneously into energy-favorable collective state (stationary) [27, 28], or certain collective behavior pattern in time sequence (dynamic) [29]. Network models for these two different collective states (stationary/dynamic) will be introduced in details in the following section 2.1.2. The collective patterns from the oscillator network will provide the final computation results. Thus, mutual interaction (coupling) between oscillators and tunable coupling strength are two critical aspects for constructing such network. The former allows every computational element in the OCN to process incoming information in parallel, while the latter serves as the memory of the system. These two aspects combined can efficiently overcome the problem of large power consumption caused by constantly transferring data between process unit and memory unit in the traditional von Neumann architecture based on Boolean machine, as shown in Fig 2.2.

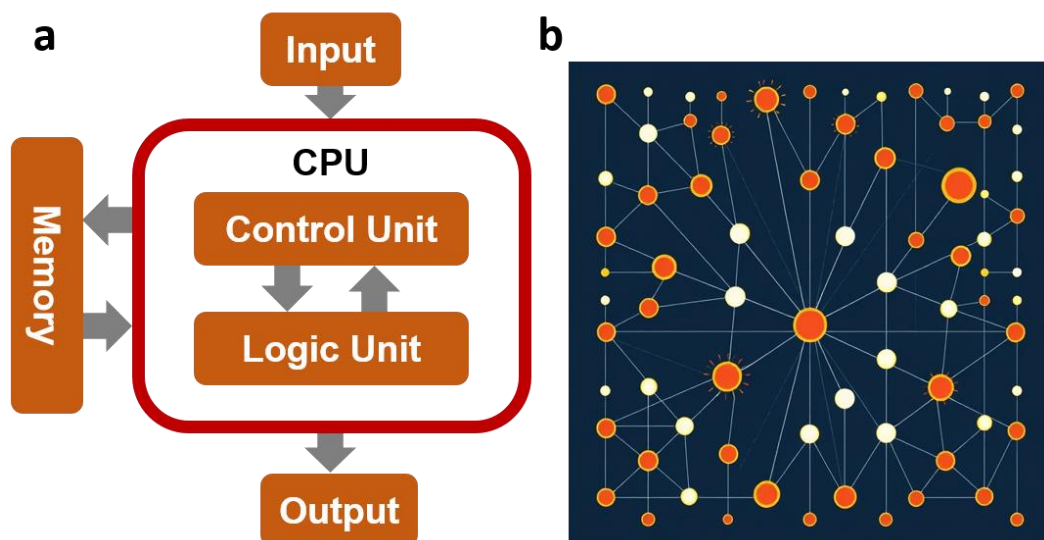


Fig 2.2. Comparison between traditional von-Neumann architecture and oscillator computational network. **a**, Typical von-Neumann architecture with separated process unit (CPU) and memory unit. **b**, Schematic illustration of oscillator computational network. Different sizes/colors of circles stand for computing nodes operating in different frequency/amplitude/phase. Lines between computing nodes represent the interactions (coupling strength).

2.1.2 Different types of OCN

Oscillatory Hopfield Network

The Hopfield network [27] is one of the most well-known oscillatory networks. In such system, information is encoded as frequency or phase signals and fed into the network as the initial states of the oscillators. Due to the mutual interaction (pre-trained weight) between oscillators,

synchronization in frequency/phase will evolve the system into the stationary energy minimum state [27, 28, 30].

One of the most studied models for describing the phase relation during synchronization process is the Kuramoto model [31, 32]. The phase dynamics $\dot{\theta}_i(t)$ of the i^{th} oscillator in a system consisting of N coupled phase oscillators can be modeled as

$$\dot{\theta}_i = \omega_i + \sum_{j=1}^N K_{ij} \sin(\theta_j - \theta_i), i = 1, 2 \dots N \quad (2.1.2.1)$$

With ω_i is the natural frequency of the oscillator, and K_{ij} the coupling matrix describing the interactions strength between the i^{th} and j^{th} oscillator. In the case where all oscillators have the same frequency ω_0 , they will try to correlate their phases (in-phase or out-of-phase) depending on the particular coupling strength (pre-train weight, described by the K_{ij} coupling matrix). Each oscillator attracts/repels phases of other oscillators proportionally to their phase difference, and finally the whole system reaches the energy minimum ground state. The collective phase state of the oscillator network serves as the output [26, 31, 32]. Such oscillatory network with computing nodes that can self-correlate has been successfully applied for auto-associative memory, like image recognition and reconstruction [14, 16, 33], as shown in **Fig 2.3a**.

Oscillatory Reservoir network

Different from the above-mentioned oscillatory network that outputs stationary energy minimum state of the system, reservoir network operates with computing nodes with highly non-linearity and short-term memory, and outputs collective states that vary with time [34]. Typical reservoir computational network has 3 layers: The input weight matrix layer, reservoir computing nodes layer, and output weight matrix layer, as shown in **Fig 2.3b**. At time t comes the input signal $X(t)$, after weighted by the input matrix then fed into the reservoir layer. The computing nodes in the reservoir layer are connected in a random manner. Depending on the input signal, all of the computing nodes will form a collective state $r(t)$ at time t . The outputs in time sequence from the reservoir layer are then mapped with a fixed readout matrix layer to form the desired results. Such system with complex temporal dynamics can be applied for solving tasks that are in time-domain like voice recognition [1] and time-series prediction [35].

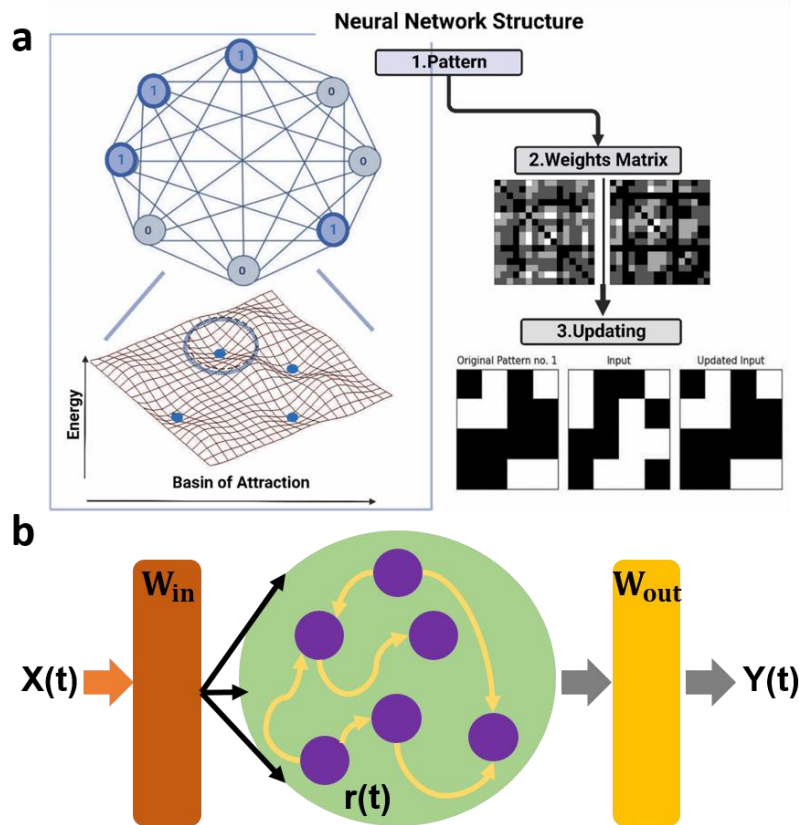


Fig 2.3. Oscillatory Hopfield network and reservoir network. **a**, Hopfield network configuration with an all-to-all connection between computing nodes. Depending on different input initial states of the oscillators, the system will converge to the energy minimum point determined by the connection strength (memory). Taken from [33]. **b**, Schematic illustration of reservoir network with input weight matrix layer (orange), reservoir computing layer (green, purple circles as computing nodes), and output weight matrix layer (yellow).

2.1.3 Physical Implementations of Oscillators

Oscillator is the basic building block for computational oscillatory network. It is generally defined as device/system that converts DC input signals into AC output signals with a certain period, amplitude and frequency [26]. A large variety of oscillators that can be realized by different electronic elements, ranging from traditional LC circuit, transistor, to unconventional solid-state devices, will be introduced in the following parts. Their working principles, CMOS compatibility and power consumption issue will also be discussed.

LC Oscillator

When an inductor is connected with a charged capacitor (as shown in **Fig 2.4**), oscillation of both the current from the circuit can be observed. And the oscillation of current can be described by the following equation:

$$\frac{d^2}{dt^2} i(t) + \frac{1}{LC} i(t) = 0 \quad (2.1.3.1)$$

With L the inductance and C the capacitance. The oscillating voltage from the inductor can be derived as:

$$V_L = L \frac{di}{dt} = -\omega_0 L I_0 \sin(\omega_0 t + \phi) \quad (2.1.3.2)$$

With $\omega_0 = \frac{1}{\sqrt{LC}}$ the resonant frequency of the circuit, I_0 the initial current, and ϕ the initial phase angle.

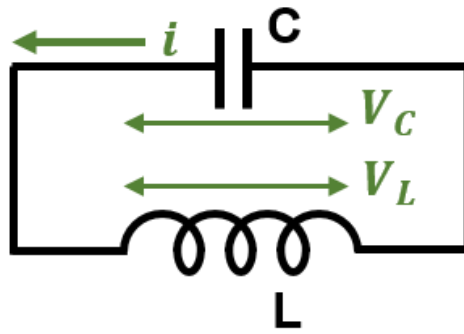


Fig 2.4. Schematic illustration of the LC oscillator. The circuit includes a capacitor C , and an inductor L without serial resistance (R), ideally.

The LC oscillator was first utilized for building the oscillator-based computer in 1959 [36]. Such oscillator (typical LC circuit) is characterized by quality factor Q , which quantifies the goodness of the LC circuit and determines how efficiently the energy is transferred in a given LC circuit. It is expressed as

$$Q = \frac{1}{R} \sqrt{\frac{L}{C}} \quad (2.1.3.3)$$

For such oscillator it is a high Q factor indicates less energy loss and high efficiency. However, when it comes to on-chip (CMOS -based) LC oscillator, the Q factor becomes relatively low. It is because micro size inductor already has very large serial resistance (R), resulting in considerable resistive loss during the operation of the oscillator [37]. Besides, the inductor needs very large chip area ($\sim 200 \mu\text{m}^2$) to improve the Q -factor [37, 38].

Ring Oscillator

The ring oscillator consists of an odd number of inverters connected in series with positive feedback, and each inverter is formed from the combination of PMOS and NMOS to realize the NOT gate function, as shown in **Fig 2.5**. The output oscillates between two voltage levels either high (1) or low (0).

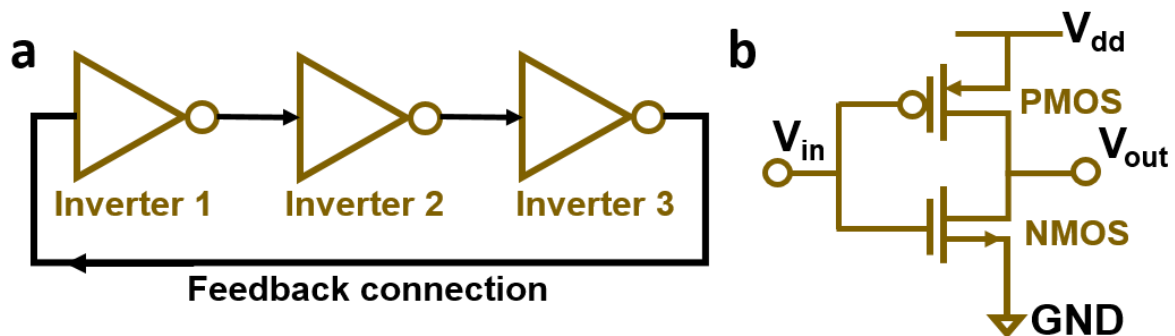


Fig 2.5. Schematic illustration of the LC oscillator. a, Circuit diagram of ring oscillator consists of three inverters and feedback connection. **b,** A typical inverter, also known as NOT gate, formed from PMOS and NMOS.

The oscillation frequency of the ring oscillator can be calculated as

$$f = \frac{1}{2N\tau} \quad (2.1.3.4)$$

With N the number of inverters in the oscillator, and τ the time delay of a single inverter. In order to achieve more gain than a single inverting amplifier, more inverter can be added to the oscillator. However, a large number of inverters will significantly reduce the oscillation frequency f . Thus, a good compromise between total gain of the circuit and oscillation frequency has to be reached. Since ring oscillator is built up by transistor, it has very good CMOS compatibility and very low power consumption ($\sim 10^{-15}$ J per oscillation cycle) [39 - 41], which can serve as the baseline when comparing the emerging oscillator formed from new solid-state devices.

Spin-based Oscillator

Unlike the above mentioned two oscillator that operate with charge current, spin-based oscillator generates AC output by the precession of the magnetic momentum caused by spin current injection. The electrons flowing in the current not only carry charges, but also spin,

whose projection along the spin axis can point up or down. In spin-polarized current, it has a majority of spin-up/down carriers, while in unpolarized charge current there is no such property. Such spin-based devices have faster switching times and lower power consumption than normal charge-based devices due to the fact that spins can be transferred faster and consumes lower energy than charges.

When spin-polarized electrons flow through a domain wall, or a ferromagnet, where the direction of the spins in the spin current is different from the local magnetization, the motion for the magnetization can be described by the LLG equation [42 - 44]:

$$\frac{\partial \mathbf{M}}{\partial t} = \gamma [\mathbf{H}_{eff} \times \mathbf{M}] + \mathbf{T}_\alpha + \mathbf{T}_s \quad (2.1.3.5)$$

With the M the magnetization, H_{eff} the effective field, T_α the damping term, and T_s the Slonczewski spin-transfer torque. The effective field can be written as the sum of externally applied field H_{ext} , the magneto-dipolar field H_{dip} , the anisotropy field H_k , the exchange field H_{ex} , and the Oersted field H_{oe} when a drive current is present. Typical memory cell based on the spin transfer torque is shown in **Fig 2.6**. It has three layers: A free layer, in which its magnetization can be switched by spin current; A fix layer where the magnetization is fixed; A spacer that is in the between the fix layer and free layer, and servers as the magnetic tunneling junction. When the free layer and the fix layer have anti-parallel magnetization (AP, shown in **Fig 2.6a**), the resistance of the memory cell is larger than the case when the free layer and the fix layer have parallel magnetization (P, shown in **Fig 2.6b**). Write current with certain amplitude can switch the memory cell between high resistance state (AP) and low resistance state (P). Normally, the energy barrier between AP and P states is designed to be high enough, so that once the memory cell is configured to one state (AP/P state) it can be stable against possible external noise, i.e. thermal fluctuation. When the energy barrier between AP and P states is engineered to be sufficiently low, sustained magnetization precession at high frequency (MHz to GHz) be observed through the conversion of magnetization oscillation to voltage oscillation [45] upon supply current, as shown in shown in **Fig 2.6c**.

Previous studies have shown that two spin transfer torque (STT) oscillator can be coupled without external electronic components needed [46, 47]. Such mutual interaction between oscillators is considered to be caused by spinwave excitations emitted from both oscillators, or by AC dipole magnetic-field interactions [46, 48]. Besides, such spin-based oscillator has good CMOS compatibility [49] with low energy consumption ($\sim 4.7 \times 10^{-15}$ J) [50] that is comparable with the ring oscillator (transistor-based) introduced in the previous section. These outstanding

properties make spintronic devices become one of the promising candidates for unconventional energy-efficient computational element.

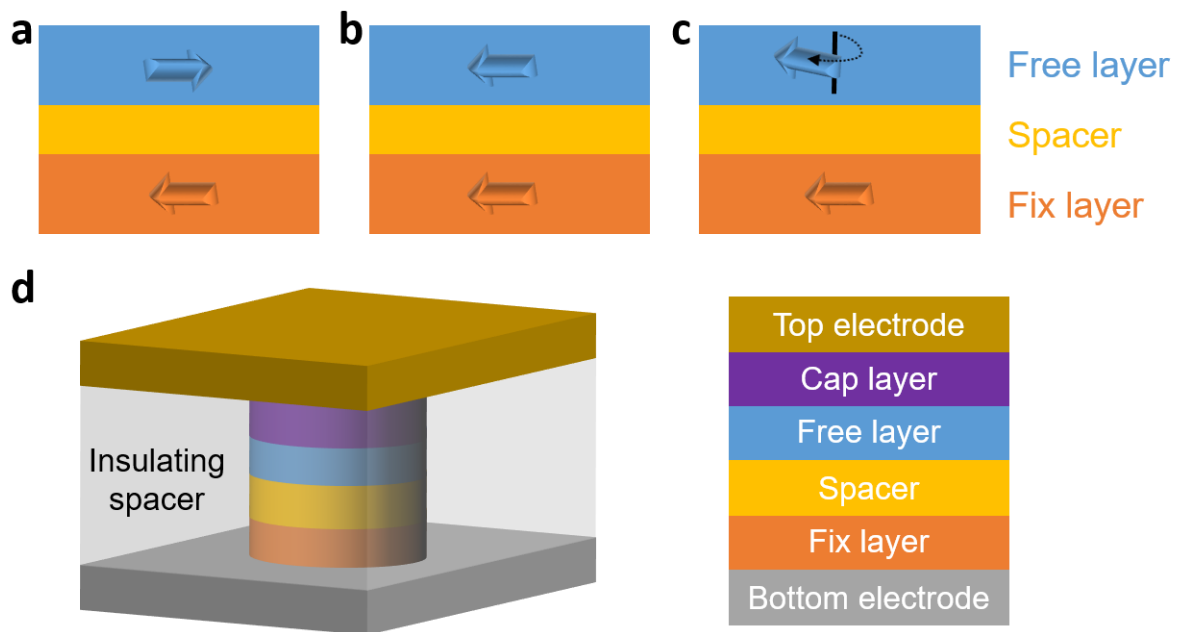


Fig 2.6. Spin transfer torque oscillator. **a**, Free layer and the fix layer have anti-parallel magnetization (AP). **b**, Free layer and the fix layer have parallel magnetization (P). **c**, The magnetization in free layer is in precession. **d**, Typical spin transfer torque (STT) oscillator with bottom electrode, fix layer, spacer, free layer, cap layer and top electrode.

Phase transition-based Oscillator

Strongly correlated oxide materials that display an insulator-to-metal transition (MIT) under an external stimulus such as temperature, magnetic field, or electric field etc. [7 - 9]. A large variety of phase transition materials include binary oxides (TiO_x , NbO_x , and VO_x) [8, 9, 51], perovskite oxide formed from rare-earth nickelate (LaNiO_3) [52], and the Ruddlesden-Popper ruthenate Ca_2RuO_4 [53] and etc. [54]. Among the phase transition-based oscillator materials, vanadium dioxide (VO_2) is of interest since the phase transition temperature T_c of this material is near room temperature (300 – 400 K) [9 - 12, 54], as shown in **Fig 2.7a**, which is highly desirable for room temperature computational devices (atmosphere pressure, room temperature, limited power supply). High temperature (~ 1080 K) MIT materials like NbO_2 require much more energy to reach phase transition temperature, while low temperature (100 – 200 K) MIT materials like NdNiO_3 need external equipment to maintain its working condition ($T < T_c$), which will also cause extra energy consumption.

VO₂ shows a large change in resistivity at around 340 K that is due to the well-known transition from a monoclinic (M1) insulating phase to a rutile (R) metallic phase (**Fig 2.7b**). The oscillation in VO₂ occurs as follows: When the system is in the high resistance state, applying a DC current source results in Joule heating (I^2R), thereby raising the device temperature and, finally, triggering a phase transition into a low resistance state [56 - 61]. This lowers the Joule heating and is accompanied by the dissipation of the accumulated heat into the surroundings [62, 63]. This leads to cooling and eventually a phase transition back to the high resistance state. The process repeats itself autonomously leading to an oscillatory output voltage, as shown in **Fig 2.7c**. Such a behavior without any external capacitor or resistor required only occurs in the current-driven mode and not in the voltage-driven - mode [64]. VO₂ oscillator that operates at room temperature is estimated to consume very low energy ($\sim 10^{-16}$ J per cycle), which is very competitive to other technologies (ring oscillator and spin-based oscillator as introduced above), and shows good CMOS compatibility [65 - 67]. Besides, Vanadium is a rather abundant element in the earth's crust with relatively low supply risk [68], when considering mass product for commercialization.

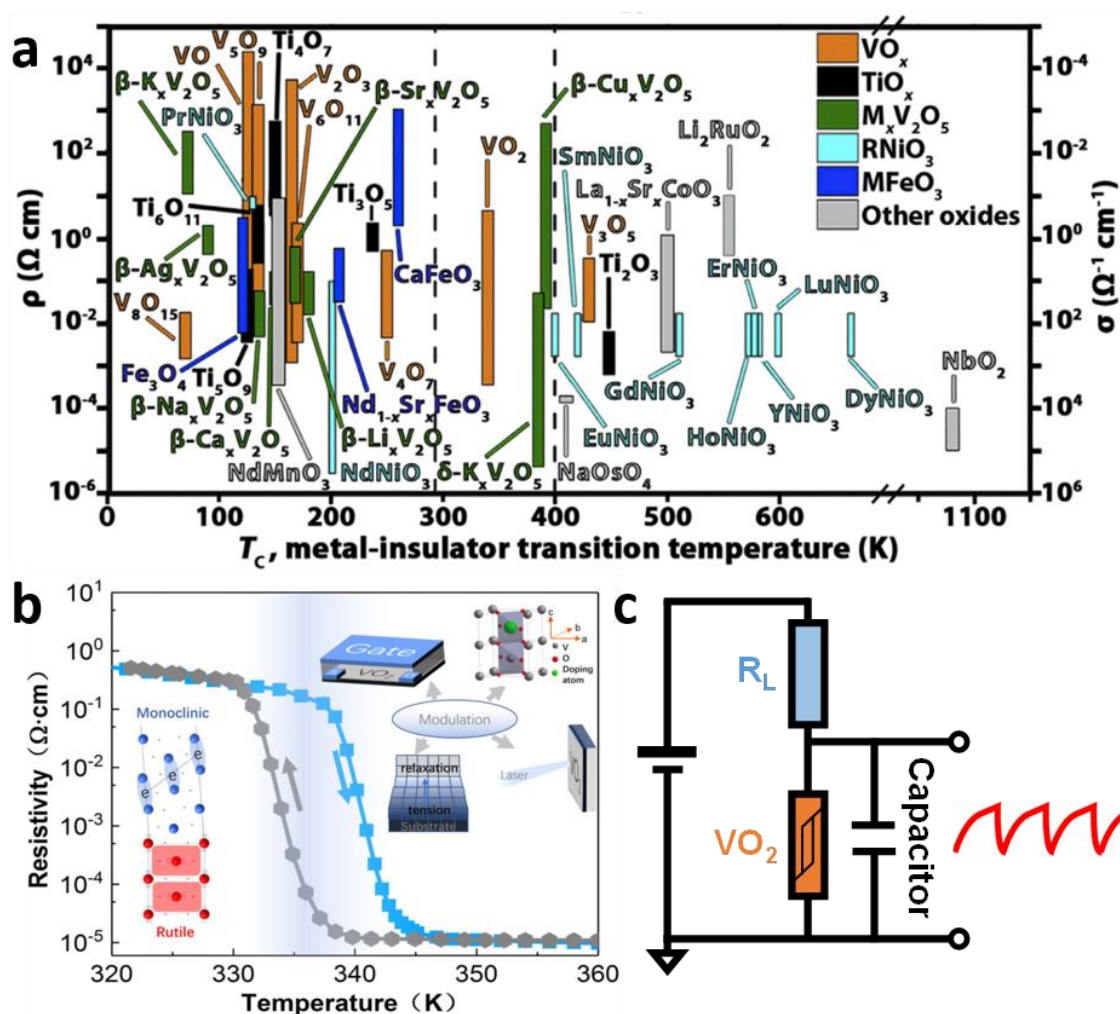


Fig 2.7. Phase transition-based oscillator. **a**, Different metal-insulator transition temperature T_c and the order of resistivity (ρ) change from a large variety of oxide materials. Taken from [54]. **b**, Typical resistivity (ρ) vs temperature (T) curve of VO_2 thin film shows more than 4 orders of change at about 340 K. The left down insert shows phase transition of VO_2 between the insulating monoclinic phase (M1) and the metallic rutile phase (R). Upper right several modulation methods for tuning the resistance state of VO_2 including doping, electric field gating, strain, and light are demonstrated. Taken from [110]. **c**, Typical circuit diagram of a VO_2 oscillator connected with external resistor (R_L) and capacitor (C) to generate oscillating voltage, modified from [15].

Another attractive aspect for efficient oscillator is the energy-recycling mechanism, which can be understood as the energy being reversibly converted, or reused, instead of being totally dissipated [26]. The former can be realized by converting energy between two forms (electrical and magnetic energy) in an LC oscillator. The latter can be realized in this thesis between thermally coupled VO_2 oscillators: The released heat during one part of the oscillation cycle from one device can thermally trigger the nearby device to oscillate. The exchange of thermal energy between oscillators during coupling substantially reduced total energy consumption, and further increases the total energy efficiency.

Due to the reasons mentioned above, heat-driven VO_2 device that works at room temperature is a promising candidate. It is chosen to construct thermally coupled oscillators for energy-efficient computational element in this thesis. Tunable thermally coupled VO_2 oscillators will be introduced in details in Chapter 4.

2.2 Spiking Neural Network (SNN)

Traditional artificial neural networks (ANN) have gained success in our daily complex tasks such as image recognition, automatic drive and etc. However, with increasing network size and connection complexity between each layer, the rapid increase in computational cost (tuning every single connection strength) during network training have made it imperative to search for more efficient network architectures with powerful computing units. Spiking neural network (SNN), which utilizes oscillators to generate temporal signals (spiking/bursting), is a special type of oscillatory computational network with sparse connection between computing nodes. By taking advantage of the oscillation states formed from neurons interacting with each other dynamically, computationally hard tasks with spatiotemporal data that requires complex feedback connection in traditional ANN can be efficiently processed in the SNN architecture.

2.2.1 Neural Network Generations

The first-generation artificial neural network (ANN) was based on the McCulloch-Pitts neurons [69] that output value 1 or 0 depending whether the weighted input value has exceeded a certain threshold, as shown in **Fig 2.8**. The neuron model can be described as:

$$y = f(\sum_{i=1}^N W_i x_i - \theta) = \begin{cases} 0 & \text{if } \sum_{i=1}^N W_i x_i - \theta < 0, \\ 1 & \text{if } \sum_{i=1}^N W_i x_i - \theta \geq 0 \end{cases} \quad (2.2.1.1)$$

With N is the number of input neurons, $x_i \in \mathbb{R}$ is the input of neuron i , W_i is the synaptic weight between the input neuron i and the output neuron, and θ is the activation threshold. It was the first type of neural network applied in perceptual recognition tasks [70, 71].

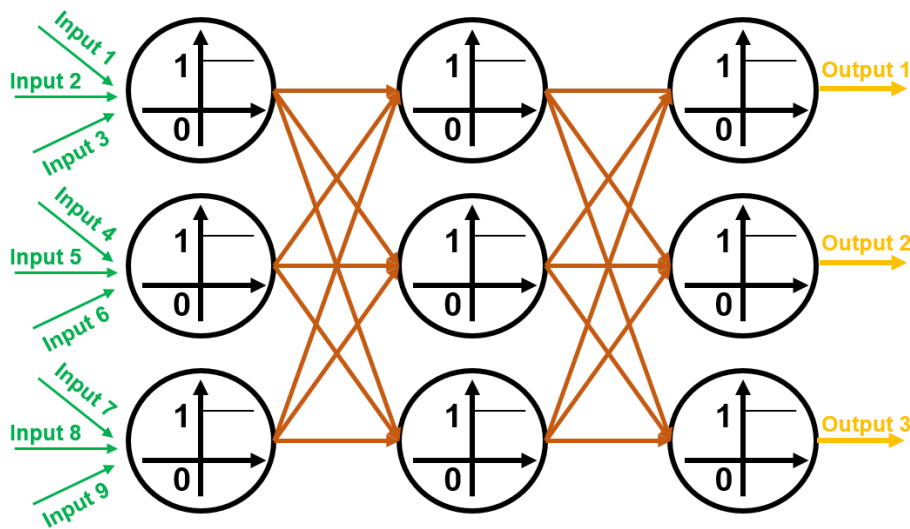


Fig 2.8. The first generation of neural network. Each neuron computing node in one layer either outputs “0” or “1” to the next layer. The brown lines represent the synaptic connection weight between each layer.

The second-generation ANN are based on computational neuron units that apply a continuous nonlinear activation function to process the input data [72, 73], as shown in **Fig 2.9a**. The neuron model can be described as:

$$y(W_i, x_i) = f(\sum_{i=1}^N W_i x_i + b) \quad (2.2.1.2)$$

With N is the number of input neurons, x_i is the input of neuron i , W_i is the synaptic weight between the input neuron i and the output neuron, and b is the bias. Most commonly seen nonlinear activation functions $f(x)$ applied in the second-generation neural network are like:

$$\text{Sigmoid function: } f(x) = \frac{1}{1+e^{-x}} \quad (2.2.1.3)$$

$$\text{Hyperbolic tangent function: } f(x) = \tanh(x) = \frac{e^x - e^{-x}}{e^x + e^{-x}} \quad (2.2.1.4)$$

$$\text{Rectified linear unit (ReLU) function: } f(x) = \begin{cases} 0 & \text{if } x \leq 0 \\ x & \text{if } x > 0 \end{cases} \quad (2.2.1.5)$$

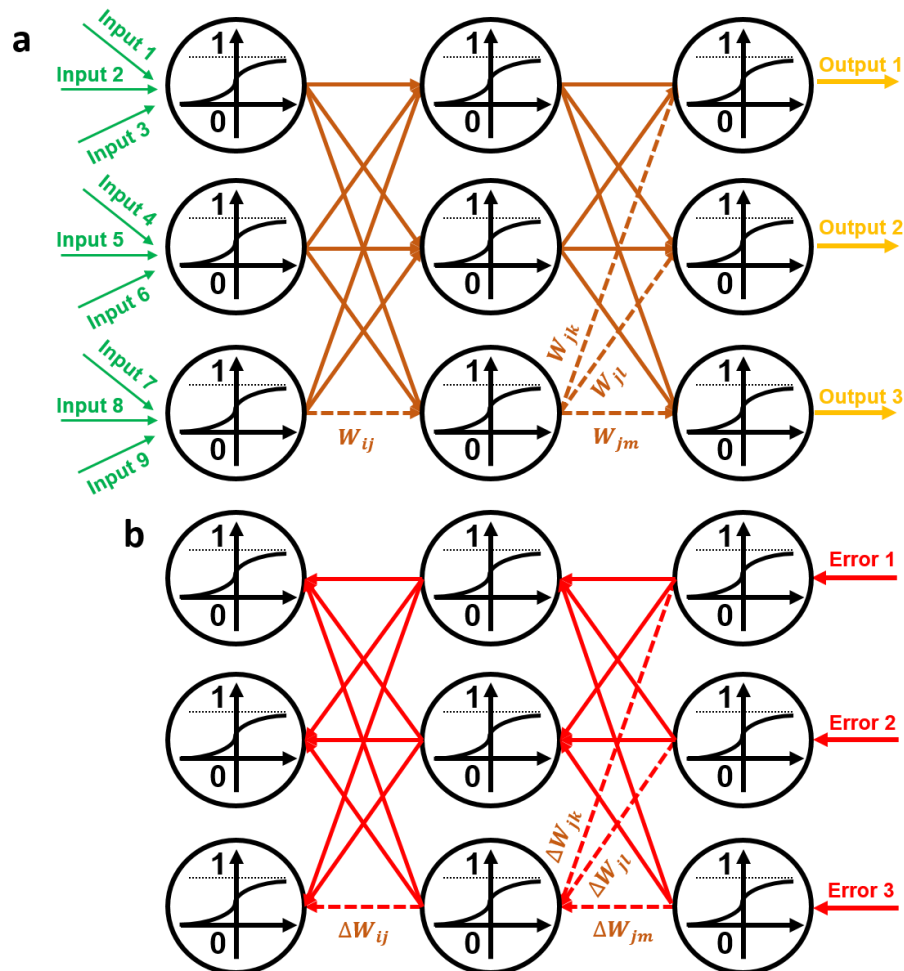


Fig 2.9. The second generation of neural network. a, Forward pass when processing incoming data. Each neuron computing node in the previous layer outputs an analog value described by the nonlinear activation function to the next layer. The brown lines represent the synaptic connection weight between each layer. **b,** Backward pass (red lines) during training stage. Here the updates for synaptic weight W_{ij} backpropagate through the network is demonstrated.

The AI technologies widely applied in technologies are based on the second-generation neural network. Such network model has gained great success thanks to the famous learning procedure called backpropagation (BP) algorithm. The network is first designed as different numbers of neuron layers and how they are connected. After that, an error function is defined to quantify the performance of the network in achieving its desired goal. The error function computes how much the network's l^{th} actual outputs (y_{out}) deviate from their target outputs (t_{out}), and is commonly expressed as the square error [74]:

$$E(W) = \frac{1}{2} \sum_l [y_{out,l}(W) - t_{out,l}]^2 \quad (2.2.1.6)$$

In order to let the network “learn” how to approach the desired output, the synaptic weights W that determines the network output y as introduced in equation (2.2.1.2) have to be changed during training. Backpropagation learning algorithm computes the gradient of the error at the current setting of all the weights, and use this gradient to change each weight proportional to the negative of its gradient. The update for weight in a non-output layer can be expressed by the chain rule of calculus:

$$\Delta W_{ij} = -\eta \frac{\partial E}{\partial W_{ij}} = -\eta \frac{\partial E}{\partial y_{out}} \frac{\partial y_{out}}{\partial W_{ij}} \quad (2.2.1.7)$$

With W_{ij} is the synaptic weight that connects neuron i to neuron j . The updates of synaptic weights start in the final layer and flow backwards to previous layers, which illustrates the meaning “backpropagation” through network, as shown in **Fig 2.9b**.

Different from the above-mentioned traditional ANN (second generation) where data is represented and process as analog-valued vector (in multi-bit precision), information is encoded as sparse and binary spikes in SNN, which saves a lot of memory and efforts in computing exact value for the matrix. Neurons in SNN can communicate with other to process the data depending on the frequency and/or phase relation, which is similar to the work principle of biological brain [22], as introduced in **2.1.1**.

Besides, unlike the artificial neuron in traditional ANN that only serves as a non-linear activation filter with no memory, spiking neurons in SNN process a certain short-term memory that can memorize the incoming information from a close past while applying integration and non-linear activation function. Such unique inherent recurrent characteristic enables SNN to become a more efficient network architecture to handle more complex tasks that need to deal with spatiotemporal information, like natural language processing, voice recognition, time series data prediction and etc. Two basic types of spiking neuron: Hodgkin-Huxley (H-H) neuron and leaky integrate-and-fire (LIF) neuron as the building block for the third-generation neural network will be introduced in details in the following section.

2.2.2 Different Types of Spiking Neurons

The Hodgkin-Huxley (H-H) Neuron Model

Based on the experimental observation of the voltage-dependent conductance in the squid giant axon, Alan Hodgkin and Andrew Huxley established a model (Hodgkin-Huxley neuron model) that provided the first quantitative description of the action potential generation in the biological system [75 - 78]. The Hodgkin-Huxley neuron model described the structural and functional properties of ion channels (Sodium channel, Potassium channel etc.), and the mechanisms of ion permeation, selectivity, and gating at a molecular level. The model also considered the conditions that control the timing of action potential onset, including threshold and refractory periods at a cellular level. Most importantly, their theory provided a mathematical foundation for modeling complex neuron behavior for the computational neuroscience. The Hodgkin-Huxley model can be described by the neuron's membrane potential in three channels dynamics:

$$I_{in}(t) = \frac{U_{mem}(t) - V_K(t)}{R_K} + \frac{U_{mem}(t) - V_{Na}(t)}{R_{Na}} + \frac{U_{mem}(t) - V_L(t)}{R_L} + C \cdot \frac{dU_{mem}(t)}{dt} \quad (2.2.2.1)$$

Where I_{in} is a current injected into the neuron (by an extracellular medium), U_{mem} is the neuron's membrane potential, V_K is the potential of the Potassium channel, R_K is the resistance of the Potassium channel, V_{Na} is the potential of the Sodium channel, R_{Na} is the resistance of the Sodium channel, V_L is the potential of the leakage channel, R_L is the resistance of the leakage channel, C is the capacitance of the neuron's membrane. Equivalent circuit diagram for the Hodgkin-Huxley model and the spiking potential generated by this type of neuron are shown in Fig 2.10.

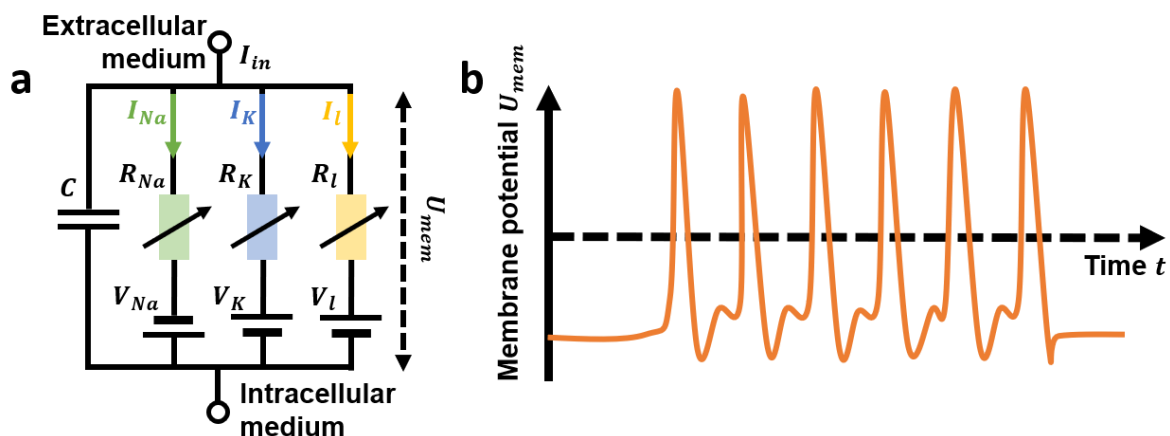


Fig 2.10. The Hodgkin-Huxley neuron model. a, Schematic illustration of the equivalent electric circuit for the Hodgkin-Huxley Neuron Model, with Sodium channel, Potassium channel and a leakage channel. b, Output spiking membrane potential the Hodgkin-Huxley Neuron Model.

The spike-generating dynamics described by the Hodgkin-Huxley model also offers an insight into the mechanism of the synchronization between neurons [79]. The spike timing between two neurons can be adjusted by the flow of current through the gap junctions and chemical synapses, until they are perfectly coincident, or at a stable relative delay. In order to study the correlation among neuron spiking, Schultheiss et al. [80] has developed the theory for phase resetting or phase response curves of the neuronal dynamics, which further reduced the Hodgkin-Huxley model down to one single dimension described by the phase of the neuron within the period of its spiking oscillation. Gouwens et al. [81] provided an example of a fast-spiking cortical cell driven with a conductance stimulus. Such stimulus mimics the current flowing through gap-junctional and synapses generated by spikes in a neighboring fast-spiking cell. It was found that the phase of neuronal oscillation can be advanced or retarded by presynaptic spikes. The degree of synchrony between presynaptic and postsynaptic spikes can thus be determined by the synaptic phase resetting function as the frequency of presynaptic spikes is varied. Besides, due to the difference in phase sensitivity of the effect of input, spiking dynamics of different cell types (neurons) are directly related to how they synchronize [82]. Such a phase-resetting relationship with prominent phase-delay and phase-advance regions (referred to as a type II phase-resetting curve) enhances the ability for stochastic synchrony in a network of coupled oscillators [83].

The Leaky Integrate-and-fire (LIF) Neuron Model

Although the Hodgkin-Huxley model is able to describe complex membrane potential dynamics of the various ion channels, several factors have hindered it to be widely used for constructing the next generation neural network [84]: 1. The expression of multi-channel dynamics with too many tunable parameters makes it very difficult to obtain a model with underlying essential nature that is critical for information processing; 2. When it comes to analytical quantification for such model to evaluate the influence of a certain parameter for model optimization, it is very hard to have meaningful the result only by using numerical simulations; 3. Complex neuron model is very challenging for designing and constructing large-scale network with high efficiency and good robustness at the same time. In order to tackle above mentioned difficulties, the Hodgkin-Huxley model can be approximated by one single response kernel describing the membrane voltage, which has been shown to be equivalent to the form of the leaky integrate-and-fire neuron model [85].

The leaky integrate-and-fire neuron model, modified from the integrate-and-fire neuron model first proposed by Lapicque [86], has become one of the most widely used models for analyzing the behavior of spiking neuron. This model has gained a lot of interest due to its capability of being mathematically simple (one channel dynamics, fewer parameters to tune), and at the same time being sufficiently complex to capture the critical fundamental features for information processing in the neural system. **Fig 2.11a** shows the typical structure of a biological neuron that consists of dendrites, a soma, axon and an axon terminal. As shown in **Fig 2.11b** and **c**, a leaky integrate-and-fire (LIF) neuron receives spikes through dendrites from all pre-synaptic neurons. The soma integrates the incoming spikes, gradually builds up the membrane potential until it reaches the threshold voltage and fires an action potential along the axon. The neuron then undergoes a refractory period. Between successive input spikes, the membrane potential of the LIF neuron slowly “leaks” away. Thus, the membrane potential of the LIF neuron contains a certain short-term memory that depends on the sequence and strength of the incoming stimuli.

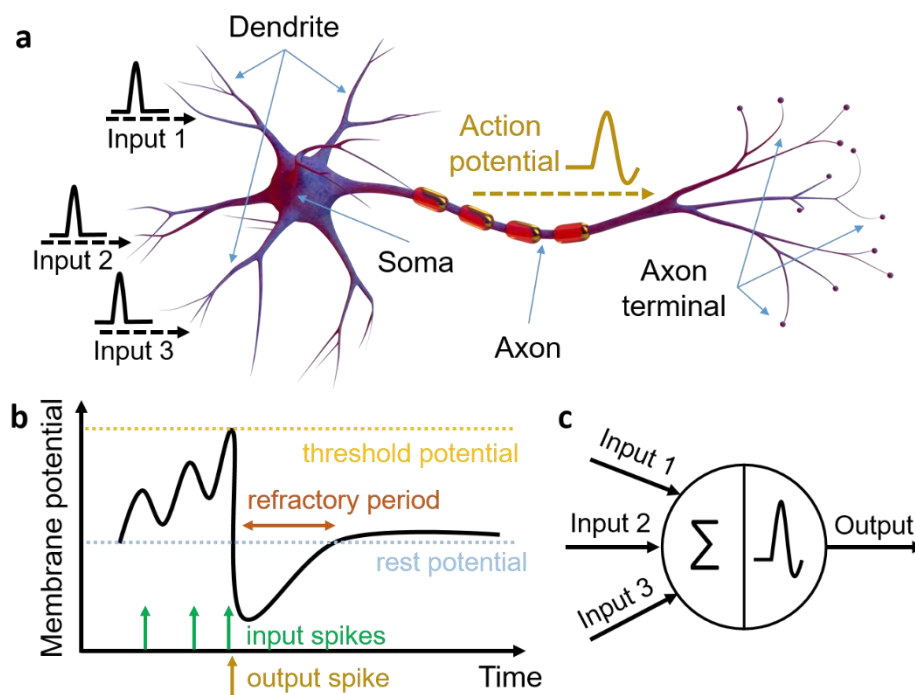


Fig 2.11. The leaky integrate-and-fire neuron model. **a**, Typical structure of a biological neuron. **b**, The potential of a LIF neuron with incoming spikes. **c**, Schematic illustration of a LIF neuron with integration (of input spikes) and triggering (of output spikes) functions.

Lapicque established an equivalent electric circuit with a resistor and capacitor connected in parallel for the leaky integrate-and-fire neuron model, as shown in **Fig 2.12**. The leaky integrate dynamics of the neuron’s membrane potential U_{mem} can be described as:

$$I_{in}(t) = \frac{U_{mem}(t)}{R} + C \cdot \frac{dU_{mem}(t)}{dt} \quad (2.2.2.2)$$

Where I_{in} is the current injected into the neuron, R is the equivalent channel resistance, and C is the equivalent channel capacitance. Later Meffin et al. [87] has modified the model with the spiking output mechanism when the neuron's membrane potential is reached:

$$I_{spike}(t) = C \left[\frac{dU_{mem}(t)}{dt} \right]_{U_{mem}=V_{th}}^{-1} (V_{reset} - V_{th}) \delta[U_{mem}(t) - V_{th}] \quad (2.2.2.3)$$

It describes an output spike is generated when the neuron's membrane potential U_{mem} reaches the threshold voltage V_{th} . After firing, the neuron's membrane potential is reset to V_{reset} level. The Dirac delta function $\delta[U_{mem}(t) - V_{th}]$ is utilized to check if the threshold level is reached.

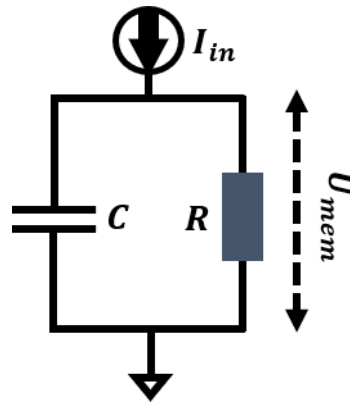


Fig 2.12. Equivalent electric circuit for the leaky integrate-and-fire neuron model. The circuit consists of an equivalent channel resistor R , an equivalent channel capacitor C .

2.2.3 SNN Architectures and Algorithms

Previously, the working principles and functionalities of the leaky-integrate-and-fire (LIF) neuron have been introduced. In this section, two types of spiking neural network (SNN) based on LIF neuron that utilize different learning methods (i.e. unsupervised/supervised learning rule) will be discussed.

Unsupervised learning with STDP rule

In 2015 Diehl and Cook [88] constructed a spiking neural network that was based on a combination of biologically plausible mechanisms, and was trained in an unsupervised way, i.e., the network learns to categorize the input samples without being provided samples with labels during learning. The network was designed to have improved biological plausibility

including conductance-based instead of current-based synapses, spike-timing-dependent plasticity (STDP) with time-dependent weight change, lateral inhibition, and an adaptive membrane threshold for spiking. The network based on 6400 LIF neurons reached an accuracy of 95% for the recognition of MNIST handwritten digits dataset [89].

Different from the current-based synapse implemented in traditional neural network that is independent of the neuron membrane potential, conductance-based synapse takes the effect from the membrane potential of both pre- and post-synaptic neurons into account. When a presynaptic spike arrives at the synapse, its conductance increases. When there is no presynaptic spike, its conductance decays exponentially. The conductance of the excitatory synapse g_e (connection that strengthens the activity of the post-synaptic neuron) can be expressed as:

$$\tau_{g_e} \frac{dg_e}{dt} = -g_e \quad (2.2.3.1)$$

Where τ_{g_e} is the time constant of an excitatory postsynaptic potential. In case of an inhibitory synapse (connection that weakens/inhibits the activity of the post-synaptic neuron), its conductance g_i can be described by the same equation but with the time constant of the inhibitory postsynaptic potential τ_{g_i} . In order to realize the unsupervised learning, spike-timing-dependent plasticity (STDP) learning rule [90] is utilized in the network for updating the conductance of synapse from input neurons to excitatory neurons. Besides, each synapse keeps track of another value during the learning process [91]. The presynaptic trace x_{pre} is increased by 1 when a presynaptic spike arrives at the synapse. When there is no incoming spike, x_{pre} decreases following the equation (2.2.3.1) mentioned above. When a postsynaptic spike arrives at the synapse, based on the presynaptic trace the change of the synaptic weight is calculated as:

$$\Delta W = \eta(x_{pre} - x_{tar})(W_{max} - W)^\mu \quad (2.2.3.2)$$

Where η is the learning-rate, W_{max} is the maximum allowed synaptic weight, and μ determines how strong the update dependent on the previous weight W , x_{tar} is the target value of the presynaptic trace at the moment when a postsynaptic spike arrives [88].

Lateral inhibition is applied in the network to promote the competition among excitatory neurons, so as to prevent multiple neurons learning the same feature. The excitatory neurons are connected in a one-to-one fashion to inhibitory neurons. Each of the inhibitory neurons is connected to all excitatory ones, except for the one from which it receives a connection. Whenever an excitatory neuron is firing, it will trigger a spike into the inhibitory neuron that

prevents other excitatory neuron from firing spikes. The membrane voltage U of the leaky integrate-and-fire model is described as:

$$\tau \frac{dV(t)}{dt} = (E_{rest}(t) - U(t)) + g_e(E_{exc}(t) - U(t)) + g_i(E_{inh}(t) - U(t)) \quad (2.2.3.3)$$

Where E_{rest} is the resting membrane potential, E_{exc} and E_{inh} the equilibrium potentials of excitatory and inhibitory synapses, and g_e and g_i is the conductance of excitatory and inhibitory synapses, respectively.

Excitatory neurons with significant different firing rates caused by the inhomogeneity of the input are modulated by lateral inhibition: In order to prevent single neuron from dominating the response pattern (maintains the highest firing rate all the time), and to ensure that the receptive fields of the neurons differentiate [88], excitatory neurons are also equipped with certain intrinsic plasticity as adaptive membrane threshold [92]. The excitatory neuron's membrane threshold is increased by a fixed value θ every time when the neuron fires, and decays exponentially back to the initial level V_{th} when the neuron becomes quiet [93]. This mechanism ensures that during learning, the firing rate of a single excitatory neurons is limited and no neuron will become dominant.

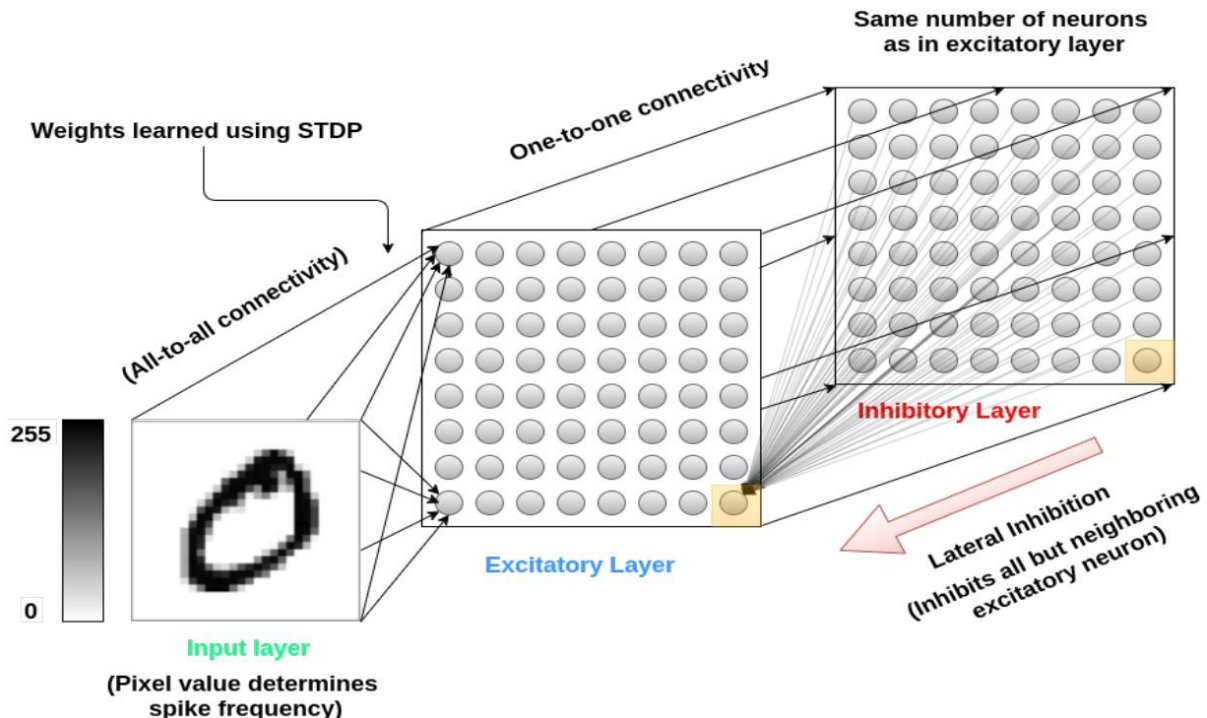


Fig 2.13. The architecture of spiking neural network with unsupervised learning mechanism. The network consists of an input layer that converts static pixel into dynamic spike train, an excitatory layer that learns to classify different handwritten digits, and an inhibitory layer that applies the lateral inhibition function. Taken from [88].

The network architecture is shown in **Fig 2.13**. The first layer is the input layer that contains 28×28 neurons (one neuron per image pixel). Each pixel is encoded into a series of spike-train, such that firing rate of the neuron corresponds to the Poisson-distribution determined by the pixel value. The output spikes of the first layer are then injected through the synaptic layer into the excitatory neurons in the second layer. The excitatory neurons of the second layer are connected to lateral inhibitory neurons in the way introduced above. During training, every neuron in the second layer will learn to extract features from the 10 handwritten digits (0 - 9). After training, based on each neuron's highest response to the ten classes of digits, it will be assigned a class that it has learned to identify. After training is done, we set the learning rate to zero, fix each neuron's spiking threshold, and assign a class to each neuron, based on its highest response to the ten classes of digits over one presentation of the training set. The response of the class-assigned neurons is then used to measure the classification accuracy of the network when the test dataset is presented.

Supervised learning with Surrogate Gradients

In the previous section spiking neural network (SNN) based on unsupervised learning mechanism has been introduced. In order to prevent any neuron from dominating the whole network (one single neuron firing rapidly all the time during training), several necessary mechanisms that balance the activities of all neurons have to be added to the system. This not only requires an additional layer for inhibitory neurons, but also inevitably increases the network complexity. From the hardware implementation perspective, sacrificing a little precision to trade for network simplicity with better efficiency is worthy. In this section, SNN based on supervised learning with less network complexity will be introduced.

The basic computing unit for this SNN is also the leaky-integrate-and-fire (LIF) neuron, whose dynamics can be described similar as equation (2.2.2.2):

$$\tau \frac{dU(t)}{dt} = -U(t) + I_{in}(t)R \quad (2.2.3.4)$$

Where $\tau = RC$ is the time constant of the equivalent RC-circuit, C is the equivalent capacitance, and I_{in} is the injection current. In the case of constant injection current, the neuron's membrane potential can be solved as:

$$U(t) = I_{in}R + [U_0 - I_{in}R]e^{-\frac{t}{\tau}} \quad (2.2.3.5)$$

Where U_0 is the initial membrane potential at $t = 0$. When there is no input current, the neuron's membrane potential will decay exponentially as:

$$U(t + \Delta t) = U_0 e^{-\frac{t+\Delta t}{\tau}} = U(t) e^{-\frac{\Delta t}{\tau}} = \beta U(t) \quad (2.2.3.6)$$

Where β is a decay factor described by the time interval Δt between the inputs. These two equations model the leaky integrate function of the neuron. An output spiking function S_{out} is used to describe the firing event when the neuron's membrane potential exceeds the threshold value θ :

$$S_{out}[t] = \begin{cases} 0, & \text{if } U(t) \leq \theta \\ 1, & \text{if } U(t) > \theta \end{cases} \quad (2.2.3.7)$$

The neuron's membrane potential at $(t + 1)$ time step can be expressed as the following equation by combining the above expressions:

$$U(t + 1) = \beta U(t) + W_{in} X(t + 1) - S_{out}[t] U_{reset} \quad (2.2.3.8)$$

Where W_{in} is the input weight matrix, X is input at each time step, and U_{reset} is reset term subtracted from the membrane potential every time after firing a spike (and then undergoes the refractory period).

As introduced in section 2.2.1, backpropagation (BP) learning algorithm is footstone for the success of traditional neural network (2nd generation). The learning error of the network is defined as the loss function, and it is minimized by applying the chain rule (gradient decent) from the final layer back to each learnable parameter (synaptic weight). As a result, the network requires a "teacher signal" (target output with labels or required value for loss calculation) and hence, the training process is called supervised learning. Different from traditional neural network where all data flows as continuous analog value that is differentiable, information in spiking neural network is represented as discrete binary spikes, which are not differentiable. There are several proposed algorithms to train the SNN with backpropagation (BP) learning algorithm [94]:

Shadow training

In shadow training, a conventional artificial neural network (ANN), that acts as the shadow behind the spiking neural network (SNN), is first trained and then converted into an SNN. The nonlinear activation function of the neuron in ANN is converted into spiking output in the SNN [95, 96]. However, there are some shortcomings when applying such algorithm. Firstly, the

temporal dynamics of spiking neuron is often omitted when using traditional ANN for processing data. Secondly, converting high-precision nonlinear activation function into spikes typically requires extra computation time and power. Thirdly, when the conversion process is not precise, which is the common case, the SNN trained from shadow ANN usually performs worse than the original ANN.

Backpropagation using spike times

Although the spikes are discrete, the spiking time is continuous and thus is differentiable. The loss function is then converted to the spiking time of the neuron. And weights are updated by taking the derivative of spike timing similar as the traditional ANN to minimize the learning error. This learning algorithm was the first proposed method for training multilayer SNNs using backpropagation [97]. However, it requires each neuron must emit a calculable spike for gradient decent during training. When the neuron is silent, it's not solvable [98]. This enforced firing for neurons will distort its temporal processing ability when dealing with input data that is dynamically varying.

Backpropagation using Surrogate Gradients

The loss function in the spiking neural network is defined as

$$L = |W_{out}S_{out} - y_{tar}| \quad (2.2.3.9)$$

Where W_{out} is the output weight matrix, and y_{tar} is the target output value. According to equation (2.2.3.8), the updates for input weight matrix can be written by the chain rule:

$$\frac{\partial L}{\partial W_{in}} = \frac{\partial L}{\partial S_{out}} \frac{\partial S_{out}}{\partial U} \frac{\partial U}{\partial W_{in}} \quad (2.2.3.10)$$

Where S_{out} is the output spiking function described by equation (2.2.3.7), U is the neuron's membrane potential described by equation (2.2.3.8), and W_{in} is the input weight matrix. However, the output spiking function S_{out} is a step-like function ($\frac{\partial S_{out}}{\partial U} \in \{0, \infty\}$), which is non-differentiable (also known as the “dead neuron problem”), as shown in **Fig 2.14a**.

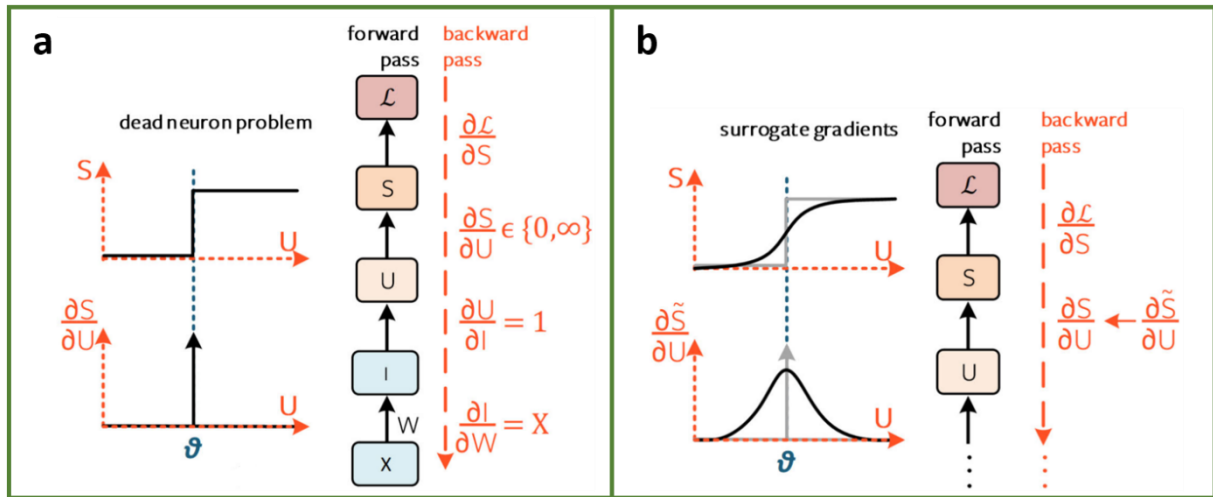


Fig 2.11. “The dead neuron” problem and surrogate gradients. **a**, The non-differentiable spiking function S_{out} makes it not possible to carry out chain rule to update weight parameter. **b**, A sigmoid function \widetilde{S}_{out} is used to substitute the non-differentiable spiking function S_{out} as surrogate gradients during training phase (backward pass). Taken from [94].

In order to overcome this problem, a continuous function, the step like function S_{out} is substituted by a continuous sigmoid function \widetilde{S}_{out} during the training phase (backward pass), as shown in **Fig 2.14b**:

$$\widetilde{S}_{out} = \frac{1}{1+e^{\theta-U}} \quad (2.2.3.11)$$

Where θ is the threshold value described in equation (2.2.3.7), and U is the neuron’s membrane potential described by equation (2.2.3.8). As a result, $\frac{\partial \widetilde{S}_{out}}{\partial U}$ can now be calculated as:

$$\frac{\partial \widetilde{S}_{out}}{\partial U} = \frac{e^{\theta-U}}{(1+e^{\theta-U})^2} \quad (2.2.3.12)$$

And the weights W_{in} will be able to be updated. Such approach is called the Surrogate Gradients. Surrogate Gradients is the most commonly applied training algorithm for the spiking neural network with time-dependent outputs, also known as the backpropagation through time (BPTT) learning rule [99, 100]. As shown in **Fig 2.15a**, the input weight will only have influence on the present and future losses. In order to calculate the global gradient, all weight parameters applied on present and future losses are summed together as:

$$\frac{\partial L}{\partial W_{in}} = \sum_t \frac{\partial L(t)}{\partial W_{in}} \quad (2.2.3.13)$$

For the immediate influence at time step t , there is no decay term contributes to the neuron potential function $U(t)$ according to equation (2.2.3.8). However, as propagating back to several time steps before (prior influence at $t - 1, t - 2, \dots$), the influence of the weight becomes more

Chapter 3 VO₂ Thin Film Preparation and Device Fabrication

In this chapter the growth method and parameters for VO₂ thin films by pulsed laser deposition (PLD) will be first introduced. Then several common thin film characterization techniques like X-ray diffraction (XRD), X-ray reflectivity (XRR), and atomic force microscopy (AFM) will be carried out to check the quality of the VO₂ sample. In the last part, the lithography process and parameters used for fabricating VO₂ oscillator device and 2.5D crossbar array will be introduced.

3.1 Pulsed Laser Deposition (PLD)

3.1.1 Fundamentals of PLD

Different techniques can be utilized to deposit thin film materials. Two major deposition techniques are physical vapor deposition (PVD) and chemical vapor deposition (CVD). The difference between them is that in PVD the vapor consists of atoms and molecules that are vaporized from the target and then deposited on the substrate, while in CVD the vapor (precursor materials) undergoes a chemical reaction at the substrate and finally the thin film material is formed. Typical CVD techniques include Metal-Organic Chemical Vapor Deposition (MOCVD) and atomic layer deposition (ALD). Most commonly used PVD techniques are sputter deposition, pulsed laser deposition (PLD) and thermal evaporation deposition.

Pulsed Laser Deposition (PLD), which has shown to be suitable for growing VO₂ thin films [101, 102], is the PVD technique utilized in this thesis. The PLD system used for VO₂ thin film deposition contains a laser, a deposition chamber, a mechanical pump and a turbo molecular pump, as shown in **Fig 3.1a**. The laser (generated from Coherent LPX pro) is directed by an optical path (a series of optical elements) into the deposition chamber through a window. The turbo molecular pump can provide a base vacuum level of $\sim 10^{-7}$ mBar. Inside the deposition chamber there are two main components: a VO₂ target with a rotator beneath it, and a substrate holder equipped with an integrated heater from the backside, as shown in **Fig 3.1b**. These two

components are separated by a tunable distance, and the surface of the target faces directly to that of the substrate holder.

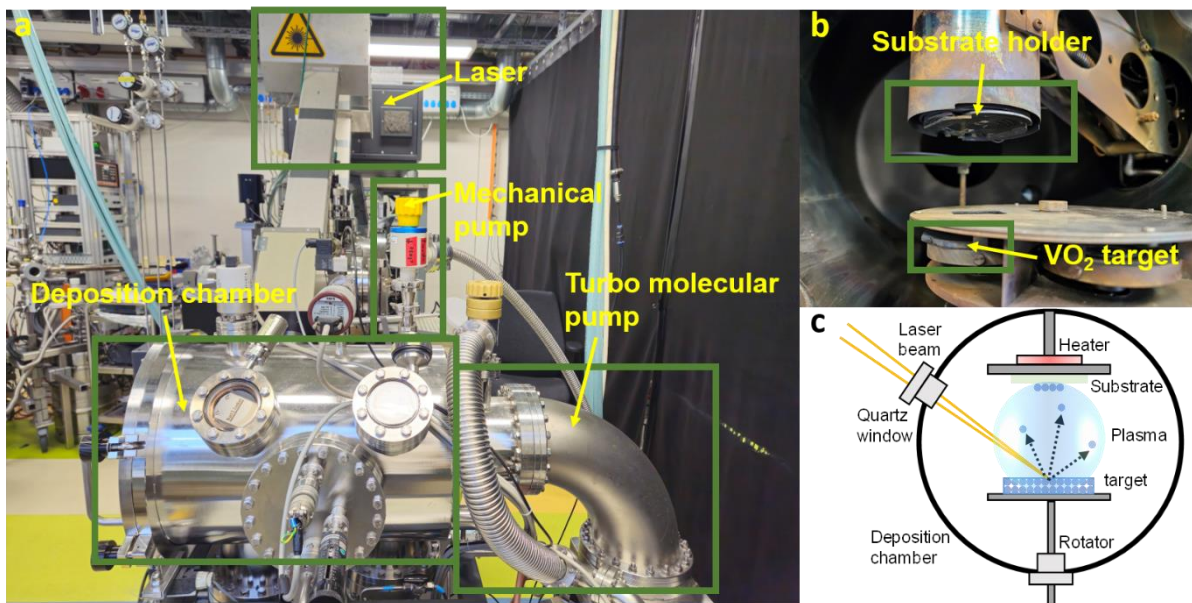


Fig 3.1. Pulsed laser deposition (PLD) system. a, The main components for the PLD system. **b,** Inside view of the deposition chamber (colloquially termed the “Aladin” system). **c,** Schematic illustration of the pulsed laser deposition process.

During the deposition process, a series of laser pulses are focused on the target surface to vaporize the target material, as shown in **Fig 3.1c**. The particles ejected by the laser become a dense cloud of material, with strong inter-particle interactions and with the ambient gas, and, thereby, forming a highly excited plasma. The plasma formed at the surface of the target material expands towards the substrate, and finally particles are deposited on the substrate and form the film. The most important parameters of the laser are its wavelength, pulse energy, and pulse spot size. Common laser wavelengths used in PLD systems are ArF (193 nm - 6.42 eV), KrF (248 nm - 4.99 eV), XeCl (308 nm - 4.03 eV), and Nd:YAG (1064 nm - 1.16 eV) [103]. Due to the absorption photon energy in the UV range for oxide materials, the 248 nm (KrF excimer) is the most commonly used wavelength for oxide deposition. The pulse energy determines how many particles are ejected from the target in a single pulse. The higher the energy, the more particles will be ablated from the target. The laser must be focused to a small spot on the target, so that an energy density which is sufficiently high to ensure plasma formation can be achieved. The distance between target and substrate holder also determines how many particles will arrive at the substrate. The further these two components are separated, the fewer particles will be able to land on the substrate to form the thin film and, most importantly, the energy of these particles can be modified.

3.1.2 Substrate selection

There are several aspects that need to be considered when choosing the proper substrate for growing VO₂ samples: 1. Phase transition temperature. As discussed in Chapter 2 section 2.1.3, a phase transition that lies close to room temperature, in a range from 300 to 400 K, is desired to achieve a low-power oscillator application. If the phase transition temperature is lower or higher than this range, extra power will be needed to maintain its working condition (when it's lower) or to reach the critical temperature (when it's higher). 2. Substrate should be a good electrical insulator. Since the focus of this thesis is thermally coupled VO₂ oscillators, a good insulator as a substrate will eliminate any leakage current between closely located VO₂ oscillators. As a result, the thermal coupling will be the dominant effect for such a system. 3. The substrate should have high thermal conductivity. As mentioned before, a good thermally conducting substrate can enhance the thermal coupling effect between VO₂ oscillators, making it easier to be observed and manipulated.

Previous work has reported on the epitaxial growth of VO₂ (002) on the rutile crystal TiO₂ (001) with a very small lattice mismatch (~ 0.86%) [104, 105]. However, when the VO₂ film is not thick enough, the in-plane tensile strain at the interface between the VO₂ thin film and the TiO₂ substrate will cause the phase transition temperature of VO₂ to decrease [106] below 290 K. In addition, etching a VO₂ device on a TiO₂ substrate is problematic. Because during the etching process, the TiO₂ substrate will become conductive due to oxygen defects caused by the Ar⁺ ion bombardment. Sapphire (0001), on the other hand, has a larger lattice mismatch (~ 12.6%) with VO₂ [107] as compared with a TiO₂ substrate. However, VO₂ (020) grown on sapphire (0001) exhibits a phase transition temperature around 320 - 340 K depending on the thickness and, thereby, the strain [108], which satisfies the requirement for oscillators operated near room temperature. Furthermore, in terms of thermal conductivity, sapphire (40 W·m⁻¹·K⁻¹) is better than TiO₂ (8.7 W·m⁻¹·K⁻¹) [109], and sapphire remains insulating after the etching process. As a result, sapphire (0001) is chosen to be a suitable substrate.

3.1.3 VO₂ Deposition parameters

A KrF excimer laser (Coherent LPX pro) beam with a pulse repetition rate of 3 Hz was focused onto the VO₂ target (99.9 % purity, Plasmaterials) in the Aladdin chamber under an ambient O₂ pressure of 0.020 mbar with the substrate temperature set to be 450 °C. The energy and fluence

of the laser beam on the target surface were 44 mJ and 587 mJ/cm², respectively. After deposition the sample was cooled down in an ambient O₂ pressure of 0.045 mbar. Different combinations of deposition parameters including: Temperature (°C), O₂ pressure (mbar), laser energy (mJ), attenuator, pulse number, and pulse frequency (Hz) were tested for growing various VO₂ samples, as shown in **Table T1**. In order to have a rough estimate of the change in resistance at the IMT, the resistance of each VO₂ sample was probed by a multimeter at room temperature (295 K), and at high temperature (383 K, higher than its MIT temperature) using a hot plate.

| Sample No. | Temperature (°C) | O ₂ pressure (mbar) | Laser energy (mJ) | Attenuator | Pulse number | Pulse frequency (Hz) | High resistance at 295 K (Ω) | Low resistance at 383 K (Ω) |
|------------|------------------|--------------------------------|-------------------|------------|--------------|----------------------|------------------------------|-----------------------------|
| 1 | 400 | 0.019 | 550 | 25% | 3000 | 3 | 6M | 100k |
| 2 | 450 | 0.019 | 550 | 25% | 9000 | 3 | 700k | 0.3k |
| 3 | 450 | 0.020 | 550 | 25% | 9000 | 3 | 1.6M | 0.6k |
| 4 | 450 | 0.020 | 400 | 50% | 9000 | 4 | 0.4M | 0.3k |
| 5 | 460 | 0.020 | 400 | 50% | 4500 | 3 | 1.0M | 0.8k |
| 6 | 480 | 0.020 | 550 | 25% | 9000 | 3 | 2.8M | 0.4k |
| 7 | 480 | 0.022 | 550 | 25% | 12000 | 4 | 1M | 0.5k |
| 8 | 480 | 0.025 | 550 | 25% | 9000 | 3 | 100 M | 8k |
| 9 | 480 | 0.025 | 550 | 25% | 15000 | 4 | 1.5 M | 0.3k |
| 10 | 520 | 0.020 | 550 | 25% | 9000 | 3 | 28M | 3k |

Table T1. Deposition parameters for different VO₂ samples. Different combination of deposition parameters: Temperature (°C), O₂ pressure (mbar), laser energy (mJ), attenuator, pulse number, and pulse frequency (Hz).

3.2 VO₂ Thin Film Characterization

Vanadium dioxide (VO₂), is one of the compounds from the strongly correlated V-O system family (VO, V₂O₃, V₃O₅, V₄O₇, V₅O₉, V₆O₁₁, V₄O₇, V₈O₁₅, VO₂) that exhibits a typical metal-to-insulator transition (MIT) with sharp resistivity changes upon external optical, electrical, thermal, and magnetic stimulus [111 - 117]. VO₂ is of particular interest since the material undergoes a transition from a high resistance state to a low resistance state near room temperature. Typically, the well-known transition from a monoclinic (M1) insulating phase to a rutile (R) metallic phase takes place at around 340 K. The crystal structure of the VO₂ monoclinic phase has a space group P21/c, and unit cell parameters: a = 0.575 nm, b = 0.452 nm, c = 0.538 nm, β = 122.6°, while the crystal structure of the VO₂ rutile phase has a space

group of $P4_2/mnm$, and unit cell parameters: $a = b = 0.455$ nm, $c = 0.286$ nm [118]. In the VO_2 rutile phase, V^{4+} ions occupy the body center and the vertex of the tetragonal structure, and each V^{4+} ion and six surrounding O^{2-} ions constitute an octahedral VO_6 unit. In the z-axis direction, the distance between the nearest V-V atoms is equal to 0.287 nm [110]. During the phase transition (from high to low temperature), the highly symmetrical quadrilateral structure of rutile phase (R) changes to the structure of the monoclinic phase which has low symmetry, with two V-V bonds with different lengths (0.312 nm and 0.265 nm). The localization of the d-electrons bound to these V-V bonds leads to its insulating property. It was presumed that such a V-V dimer formation directly results in the change from the high temperature delocalized state to the low temperature localized state [110]. Recently, new ultrafast techniques have demonstrated that such a phase transition takes place in only approximately 5 picoseconds [119], which has raised new interest in utilizing VO_2 very high frequency oscillator applications.

3.2.1 XRD measurement

X-Ray diffraction, also known as XRD, is a common method used to determine structural parameters of bulk materials and thin films. The X-ray diffractometer used for the characterization of the VO_2 samples in this thesis is the *Bruker D8 Discover* with Cu-K α radiation with a wavelength of $\lambda = 1.5418$ Å, as shown in **Fig 3.2a**.

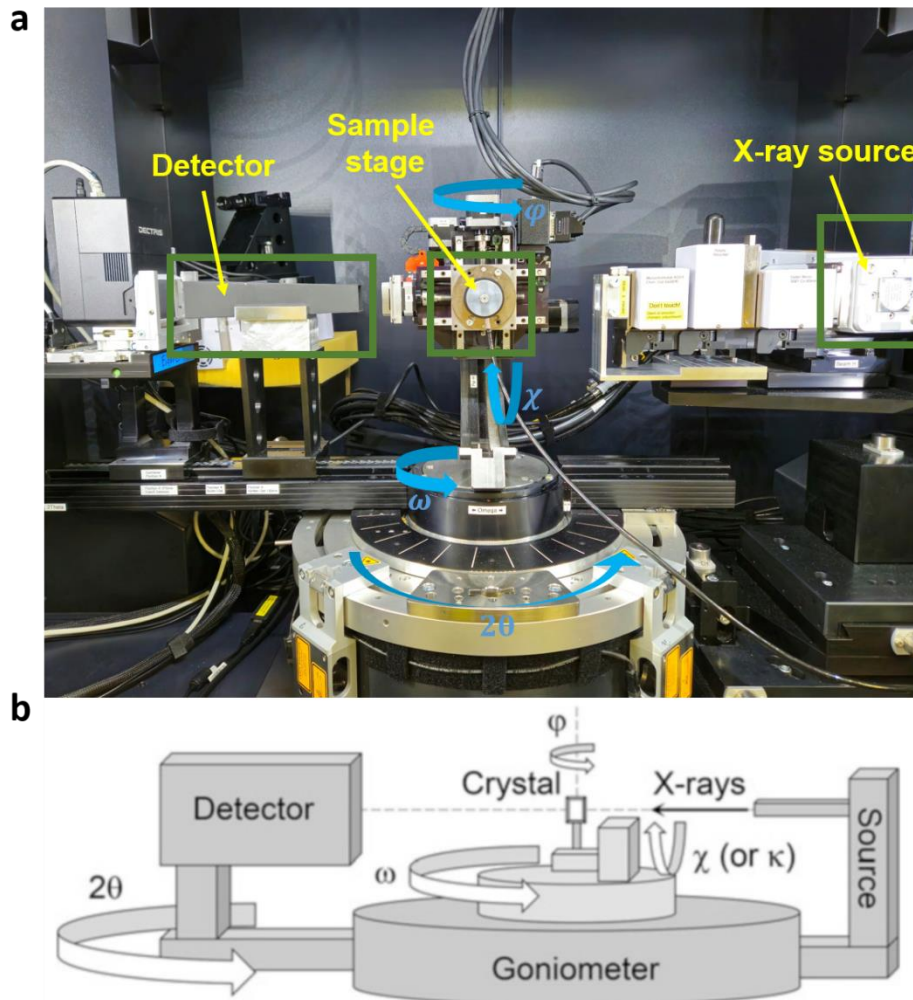


Fig 3.2. Modular architecture of the Bruker D8 diffractometer. a, The main components for the XRD system. **b,** Schematic illustration of the main components and the four-rotation axis, taken from [120].

The instrument consists of X-ray source, sample stage, detector and a motorized goniometer used to orient and move the crystal. The goniometer typically has four axes of movement to orient the crystal with the incident X-ray beam. As shown in **Fig 3.2b**, the detector is rotated around the 2θ -axis within the instrument's horizontal plane. Movement around the ω -axis takes place in the horizontal plane of the instrument, the χ -axis refers to elevation in the vertical plane, and movement around ϕ rotates the crystal around its local mount axis. The condition for constructive interference of X-ray diffraction condition is described by von Laue's law in reciprocal space as:

$$k' - k = S \quad (3.2.1.1)$$

And is described by the Bragg's law in real space as:

$$2 d_{hkl} \cdot \sin(\theta) = n \cdot \lambda \quad (3.2.1.2)$$

With d_{hkl} the spacing between lattice planes (hkl), θ the incidence angle, and λ the wavelength of the incident beam, as shown in **Fig 3.3**. The Bragg's law is satisfied when the scattering vector S equals to the reciprocal lattice vector Q_{hkl} , which can be converted from the diffraction angle 2θ by the equation:

$$|Q_{hkl}| = 4\pi \sin(\theta)/\lambda \quad (3.2.1.3)$$

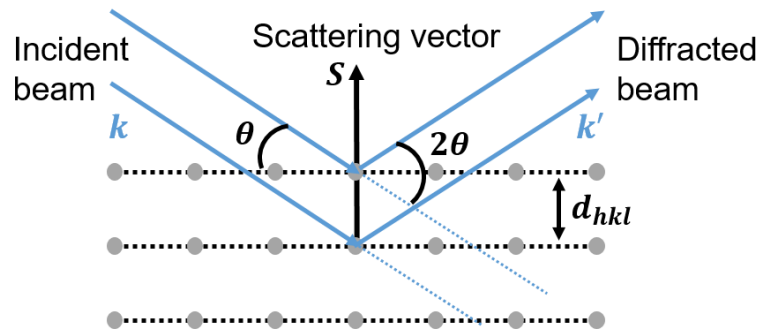


Fig 3.3. Schematic of X-ray diffraction. Illustration of the conditions required for Bragg diffraction to occur.

The constructive interference of a family of lattice planes (hkl) will occur as a Bragg peak at a specific angle θ (with a fixed wavelength of X-Ray) in the XRD pattern. The out-of-plane $\theta - 2\theta$ scan, is firstly applied to obtain the information from the lattice planes parallel to the sample surface. In a $\theta - 2\theta$ scan when changing the angle θ of the incident beam, the angle of the detector is always kept at 2θ to be aligned with the direction of the diffracted beam. As a result, the reciprocal lattice vector Q_{hkl} , which is equal to the scattering vector, will be always normal to the sample surface.

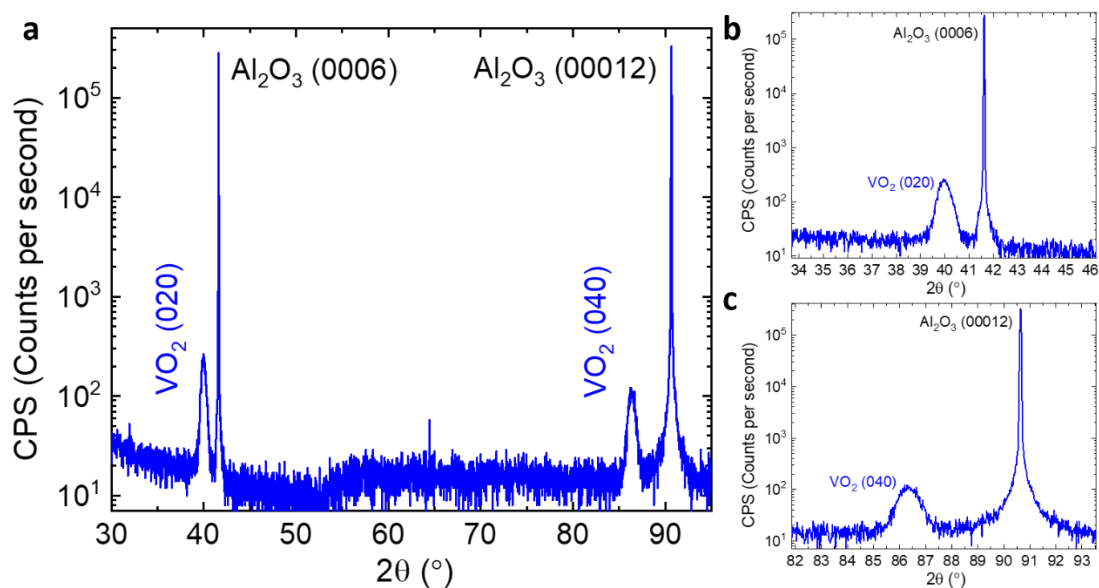


Fig 3.4. X-ray diffraction (XRD) measurement of a typical VO₂ film grown on sapphire [0001] substrate. **a**, Theta (θ) - 2Theta (2θ) scan shows (020) peak at $2\theta = 39.99^\circ$ and (040) peak at $2\theta = 86.30^\circ$. **b**, Zoom-in view of the (020) peak at $2\theta = 39.99^\circ$. **c**, Zoom-in view of the (040) peak at $2\theta = 86.30^\circ$. Data from [121].

The XRD $\theta - 2\theta$ of the VO₂ sample is shown in **Fig 3.4**. It can be observed that the VO₂ thin film is well textured on the sapphire [0001] substrate. Two dominant peaks from (020) and (040) appear at the position $2\theta = 39.99^\circ$ and $2\theta = 86.30^\circ$, respectively. Such result is similar as the previously reported work [107].

3.2.2 XRR measurement

The geometry of the X-ray reflectivity (XRR) measurement setup is similar to the one used in the XRD measurement shown in **Fig 3.2**. The only difference is the angle of the incident beam 2θ is kept within a very small range ($< 5^\circ$). When the incident angle is below the critical angle, the X-Ray will only be reflected by the sample surface and the intensity of the reflected beam doesn't change too much, as shown in **Fig 3.5a**. As soon as the incident angle is larger than the critical angle, the reflectivity of the X-Ray decreases rapidly as the incident beam penetrates the material, as shown in **Fig 3.5b**.

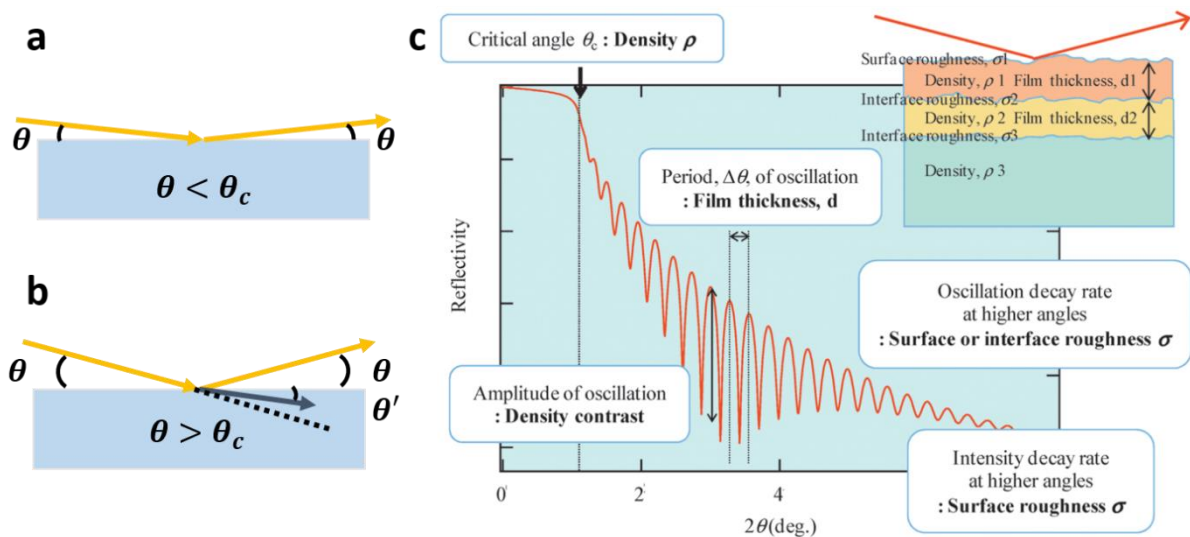


Fig 3.5. Schematic of X-ray diffraction (XRR). **a**, The incident angle is below the critical angle. **b**, The incident angle is above the critical angle. **c**, Parameters of thin film determined by X-ray reflectivity (XRR) measurement, taken from [122].

The Interference effect starts to occur when the incident angle is larger than the critical angle, due to the interaction between the reflected beams from the sample surface and beams from the interface between different layers. For X-ray, the refractive index only depends on the electron density, for known composition the electron density can be translated to the mass density of the

probed material. For samples with monolayer, the oscillation frequency is dependent on the film thickness, while for samples with multiple layers the different reflections are superposed. The X-Ray reflectivity profile shows an oscillation pattern based on the parameters of the sample films and the substrate. The XRR measurement can be used to determine: 1. The density ρ of the material from the critical angle θ_c ; 2. The film thickness d from the fringes of oscillation of the X-Ray reflectivity curve; 3. Surface or interface roughness σ from the oscillation decay rate at higher angles, as shown in **Fig 3.5c**. The XRR measurement of the VO₂ sample is shown in **Fig 3.6**. The VO₂ thin film thickness is determined to be 28.78 ± 2.54 nm.

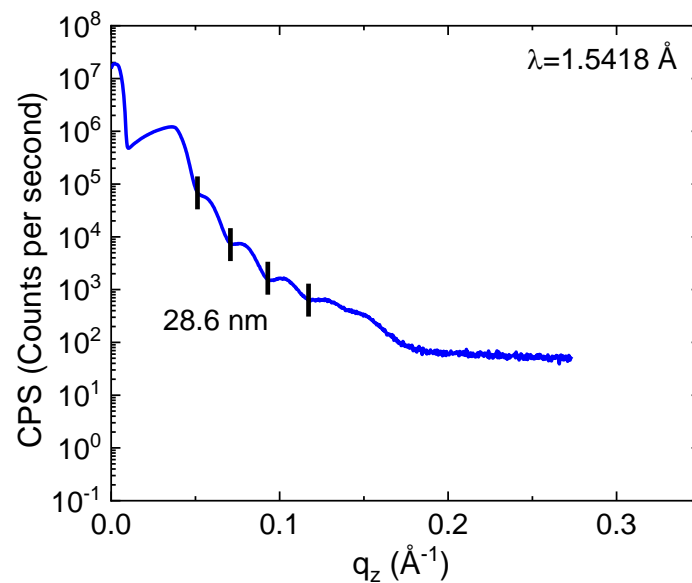


Fig 3.6. X-ray diffraction (XRD) measurement of a typical VO₂ film grown on sapphire [0001] substrate. The film thickness determined from the XRR measurement is 28.78 ± 2.54 nm. Data from [121].

3.2.3 AFM measurement

Surface morphology is also important for the property analysis of the sample and device fabrication. AFM is mainly used to check the surface morphology of the device after each fabrication step, so that the quality of the interface can be checked. The surface morphology is examined by the *Bruker AFM* in this work. The setups of the AFM are schematically illustrated in **Fig 3.7**. The components of AFM include a probe that has a sharp tip ending with an apex of several nanometers of diameter mounted on a soft cantilever. A laser beam that hits the edge of the cantilever is reflected on a photodetector, acting as an optical lever. A photodetector is used to monitor the angstrom movements of the cantilever, due to the changing of the interacting forces between the tip and sample. An external electronic controller acts as an important role

for controlling the probe by the feedback loop of the system. During the measurement, the cantilever is operated in tapping mode. As the tip comes into contact with the surface for each oscillation, it is deflected due to the distance related to Coulomb-repulsion between the tip and sample. The initial height of the cantilever is chosen so that the tip will never break contact with the sample. The amplitude will thus directly reflect changes on the surface, the feedback loop is used to shift z to restore the target amplitude, and the positions (xyz) of the piezoelectric scanner are captured. The VO_2 thin film was probed by the AFM and its surface RMS roughness was determined to be 0.78 nm.

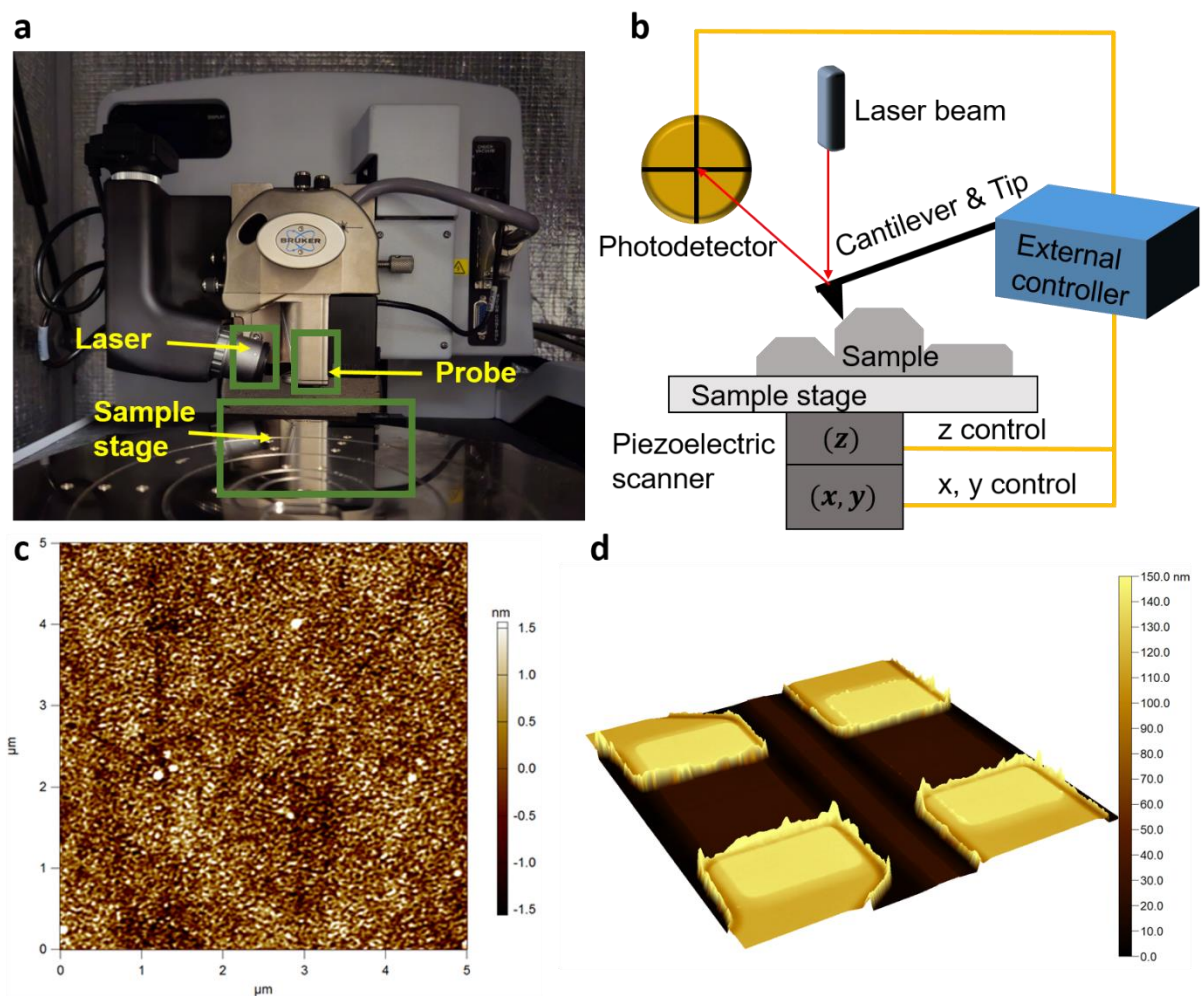


Fig 3.7. Atomic force microscopy (AFM). **a**, Inside view of the *Bruker AFM*. **b**, Schematic illustration of the AFM setup, including an external electronic controller, laser, photodetector, piezoelectric scanner and sample stage. **c**, AFM scan of a typical VO_2 thin film, data from [121]. **d**, AFM scan of a typical VO_2 device set.

3.3 Single VO₂ Device Set Lithography

The prepared thin films were patterned into microscopic devices by conventional optical lithography techniques - maskless aligner (Heidelberg MLA 150), and ion beam etching (scia coat 200) were used. As shown in **Fig 3.8** the lithography steps: **a**: VO₂ thin film (shown as blue) was deposited on the sapphire substrate (shown as light gray); **b**: Negative tone photoresist (shown as brown, ARN-4340, Allresist) was patterned on the VO₂ thin film to define the device area (dose: 230, defocus: -8); **c**: Ion beam etching carried out by Ar⁺ bombardment was used to etch away the non-device area down to the sapphire substrate; **d**: After ion beaming etching, only pre-defined VO₂ device area was left under the photoresist; **e**: The photoresist was removed by remover solvent (Remover AR 300-70, Allresist); **f**: Positive tone photoresist (shown as dark gray, ARP-3540T, Allresist) was patterned on the VO₂ thin film to define the contact pad area (dose: 110, defocus: -6); **g**: Ti and Au (~ 77 nm) was deposited by sputtering deposition in scia coat 200 sequentially (shown as gold); **h**: Lift-off process - The photoresist was removed by remover solvent (Remover AR 300-70, Allresist). **Fig 3.8i** shows the top view of the two VO₂ devices after lithography, they have two independent signal lines and share one common ground line.

For fabricating nanoscopic device, the electron beam lithography was used, a JEOL EBL machine (JBX-8100FS; 100 kV) with an ARN-7520-18 resist was utilized for the lithography.

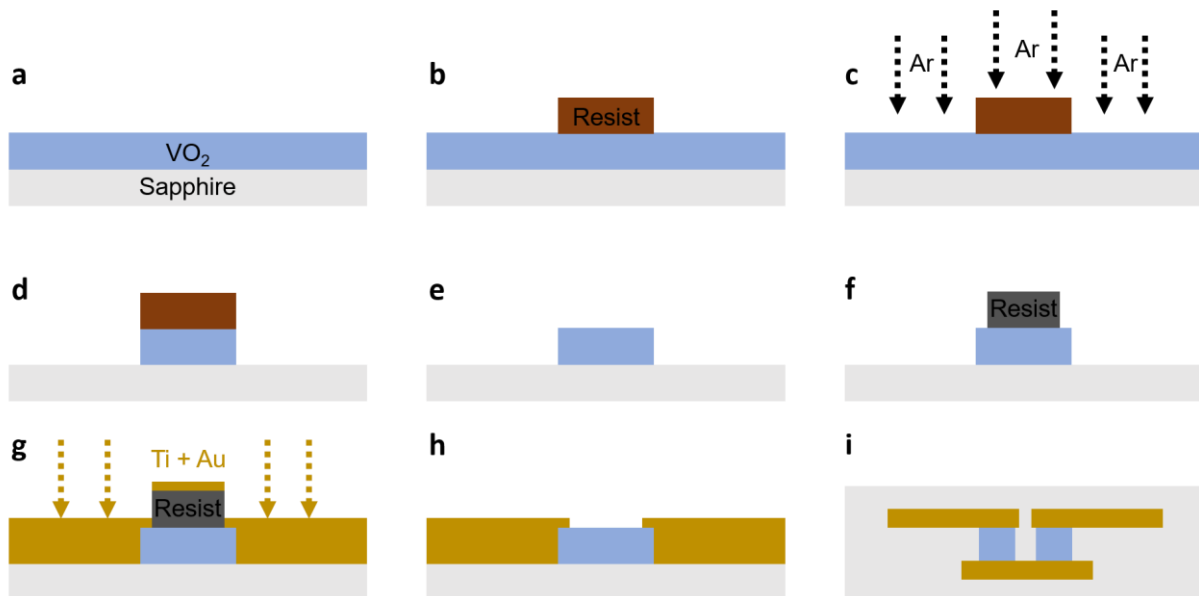


Fig 3.8. VO₂ device lithography steps. **a**, VO₂ thin film on sapphire substrate. **b**, Negative tone photoresist patterning. **c**, Ion beam etching by Ar⁺ bombardment. **d**, VO₂ device after etching. **e**, Removal of negative photoresist. **f**, Positive tone photoresist patterning. **g**, Deposition of Ti and Au for contact pad. **h**, Lift-off process, removal of positive photoresist. **i**, Top view of two VO₂ device.

Deposition of ~ 200 nm AlO_x capping layer on VO_2 device is optional. When there is no capping layer, the device test kit was operated in the probe-station in vacuum ($\sim 10^{-4}$ mBar) at 295 K to prevent oxidation of the device due to the exposure to water vapor and air. In order to carry out the tests of the VO_2 device more conveniently anytime at normal atmosphere, AlO_x capping layer was added to the new test kit by adding an extra lithography step after **Fig 3.8h**. The device with AlO_x capping layer is shown in **Fig 3.9a** and **b**. The calibration bar ($5 \times 10 \mu\text{m}^2$) used for checking alignment shows good alignment precision in **Fig 3.9c**, only about $< 0.5 \mu\text{m}$ alignment error is observed, which is acceptable for two $3 \times 3 \mu\text{m}^2$ VO_2 devices separated with $1.5 \mu\text{m}$ gap.

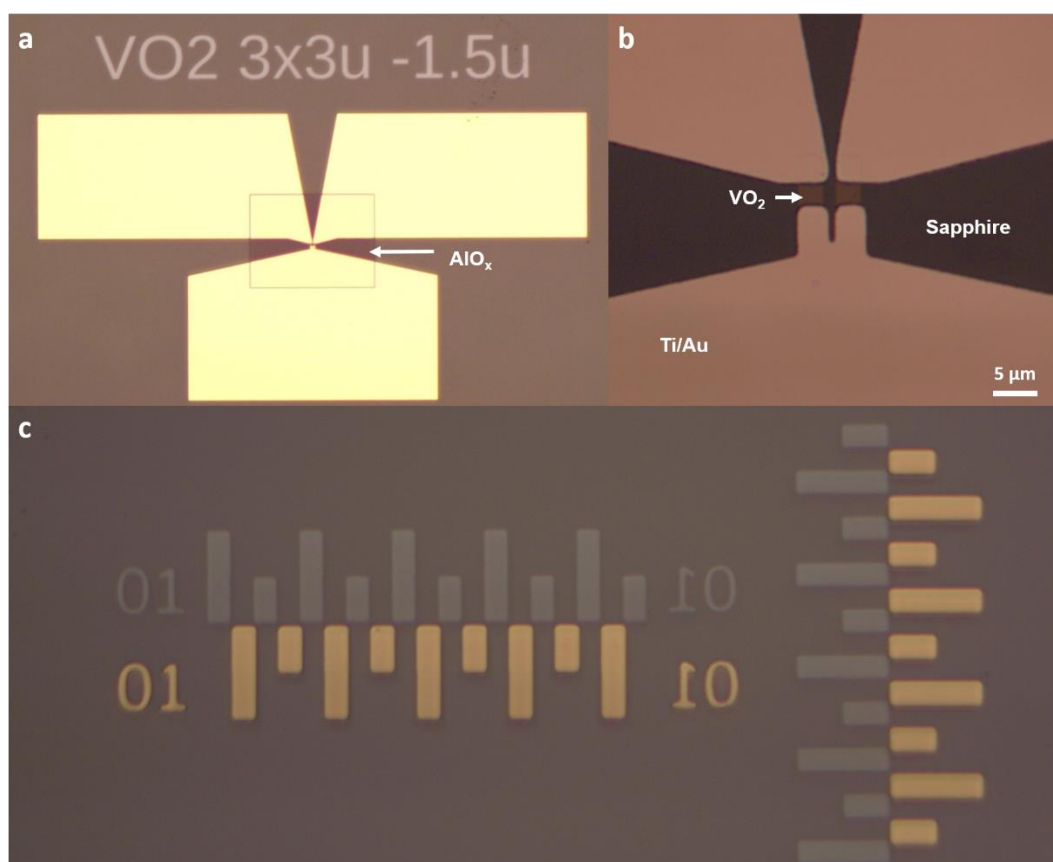


Fig 3.9. Typical VO_2 device after fabrication process. **a**, Device set that is capped with AlO_x layer to prevent oxidation. **b**, Two $3 \times 3 \mu\text{m}^2$ VO_2 devices separated with $1.5 \mu\text{m}$ gap. **c**, The calibration bars ($5 \times 10 \mu\text{m}^2$) used for alignment precision check.

3.4 VO_2 2.5D Crossbar Array Lithography

As introduced in the previous section 2.2.3, large-scale spiking neural network with supervised learning mechanism based on VO_2 leaky integrate-and-fire (LIF) neuron is studied in this thesis. In order to fabricate the large-scale VO_2 LIF neuron array, the layout for the 2.5D integrated

crossbar array has been specially designed, as shown in **Fig 3.10a**: Two VO₂ oscillator devices closely located to each other are placed at the bottom layer. They are connected with two independent signal lines (left and right), respectively. They share the same ground line. Then a 230 – 260 nm AlO_x insulating spacer is deposited to cover the bottom layer, but leaving the ground line contact pad part vacant. In the end, the ground line is deposited on the top of the AlO_x insulating spacer to form the crossbar array structure. The layout design for a 10×10 crossbar array is demonstrated in **Fig 3.10b**. And the schematic illustration of electrical connection for the 10×10 VO₂ LIF neuron crossbar array is shown in **Fig 3.10c**. In each VO₂ LIF neuron computing node: The spike current input is injected through left signal line (L+ pad in **Fig 3.10b**), and will be leaky integrated by the left VO₂ device. The triggered spiking function can be realized by the right VO₂ device supplied with sub-threshold current/voltage through right signal line (R+ pad in **Fig 3.10b**). The spiking voltage can be readout from right signal line. The two VO₂ devices share the same ground line (GND pad in **Fig 3.10b**).

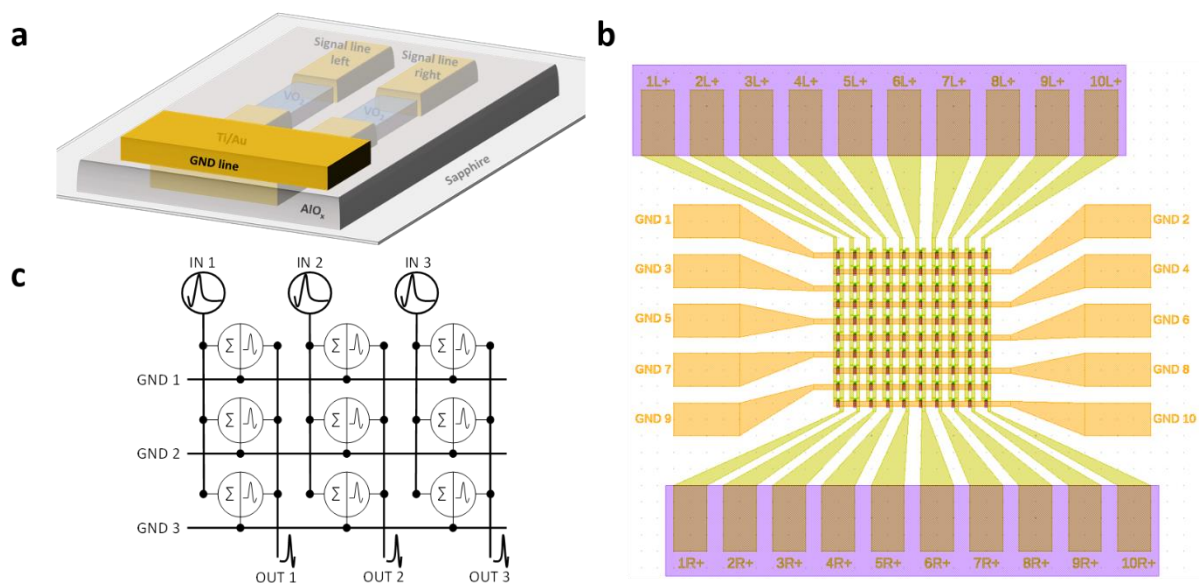


Fig 3.10. VO₂ 2.5D array design. **a**, A detailed view of a single VO₂ LIF neuron computing node, which contains two VO₂ devices and 2 signal line at the bottom, an AlO_x insulating spacer in the middle, and a shared ground line on the top. **b**, The layout design for a 10×10 crossbar array. L+ pads correspond to the left signal lines, R+ pads correspond to the right signal lines **c**, Schematic illustration of electrical connection for the 10×10 VO₂ LIF neuron crossbar array.

The details of the lithography utilized to fabricate the VO₂ 2.5D array will be introduced and demonstrated in the following part. Firstly, same as introduced in section 3.3, negative tone photoresist (ARN-4340, Allresist) was patterned on the VO₂ thin film to define the device area (dose: 230, defocus: -8). Ion beam etching carried out by Ar⁺ bombardment was used to etch away the non-device area down to the sapphire substrate. After ion beaming etching and

removal of the resist, the VO₂ devices in first layer were examined by the AFM technique introduced in section 3.2.3. Two plateaus of VO₂ with a width of about 3 μm separated with 1.5 μm can be observed from the AFM (Atomic force microscopy) scan, indicated a satisfying device morphology, as shown in Fig 3.11. However, it can also be observed, due to the harsh ion beaming etching, there is about ~ 3 nm roughness at the edge of the device. But luckily, such fabrication defect of edge roughness wasn't critical to the device performance, and hardly had any influence on the overall crossbar array (will be shown in the Chapter 5).

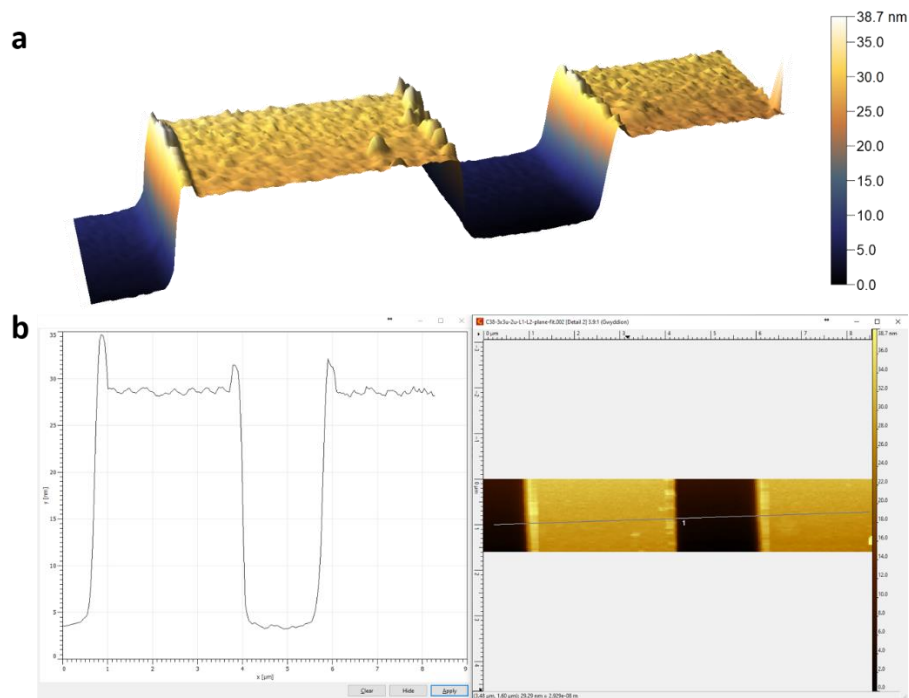


Fig 3.11. VO₂ 2.5D array first layer morphology. a, Surface structure of the VO₂ devices after ion beaming etching, scanned by AFM. b, The height profile acquired from the AFM scan.

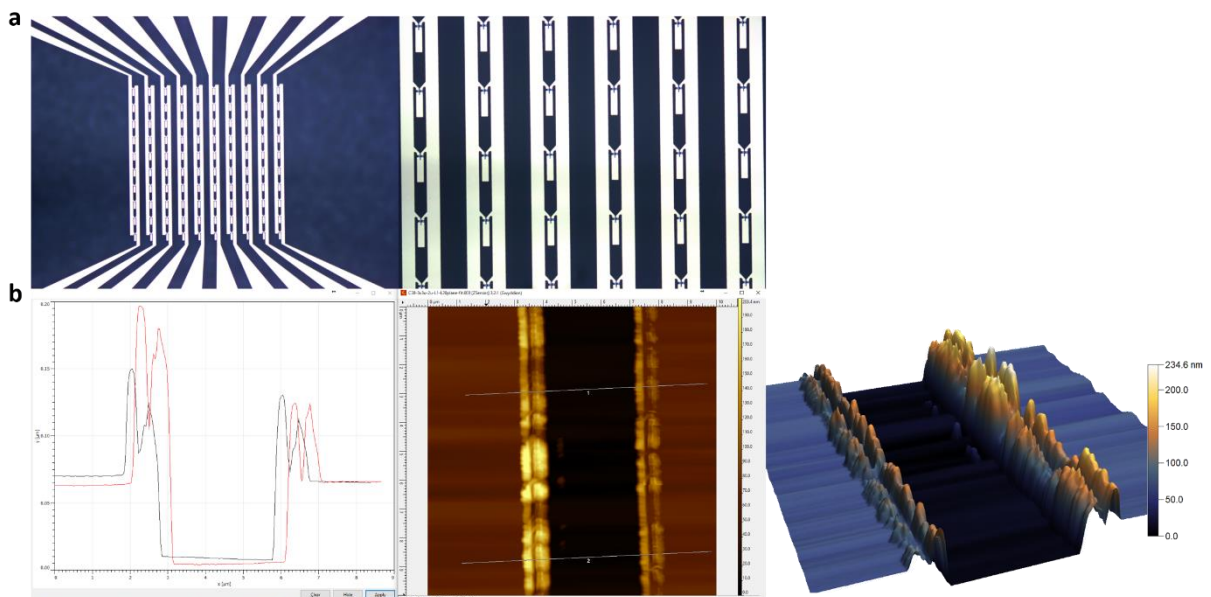


Fig 3.12. VO₂ 2.5D array second layer morphology. **a**, Optical microscope image of VO₂ devices, left and right signal lines, and ground line contact pad. **b**, The Surface structure and height profile acquired from the AFM scan.

Next, also same as introduced in section 3.3, positive tone photoresist (ARP-3540T, Allresist) was patterned on the VO₂ thin film to define the contact pad area (dose: 110, defocus: -6). And then the electrode (Ti-Au) was deposited by sputtering deposition in scia coat 200 sequentially to from the right signal line, left signal line, and ground line contact pad at the same time (shown in Fig 3.12a). It can be determined from the AFM height profile that the thickness of the deposited Ti and Au layer was about 70 nm. Besides, significant side-wall defect after the lift-off process cannot be omitted. From the AFM scan it can be observed that the side-wall of the Ti and Au layer can be as high as ~ 190 nm. Such defect will cause current shunting path/dielectric breakdown through the AlO_x insulating spacer layer if not properly addressed. As a result, post-processing like mechanical polishing that will remove the side-wall defects is required.

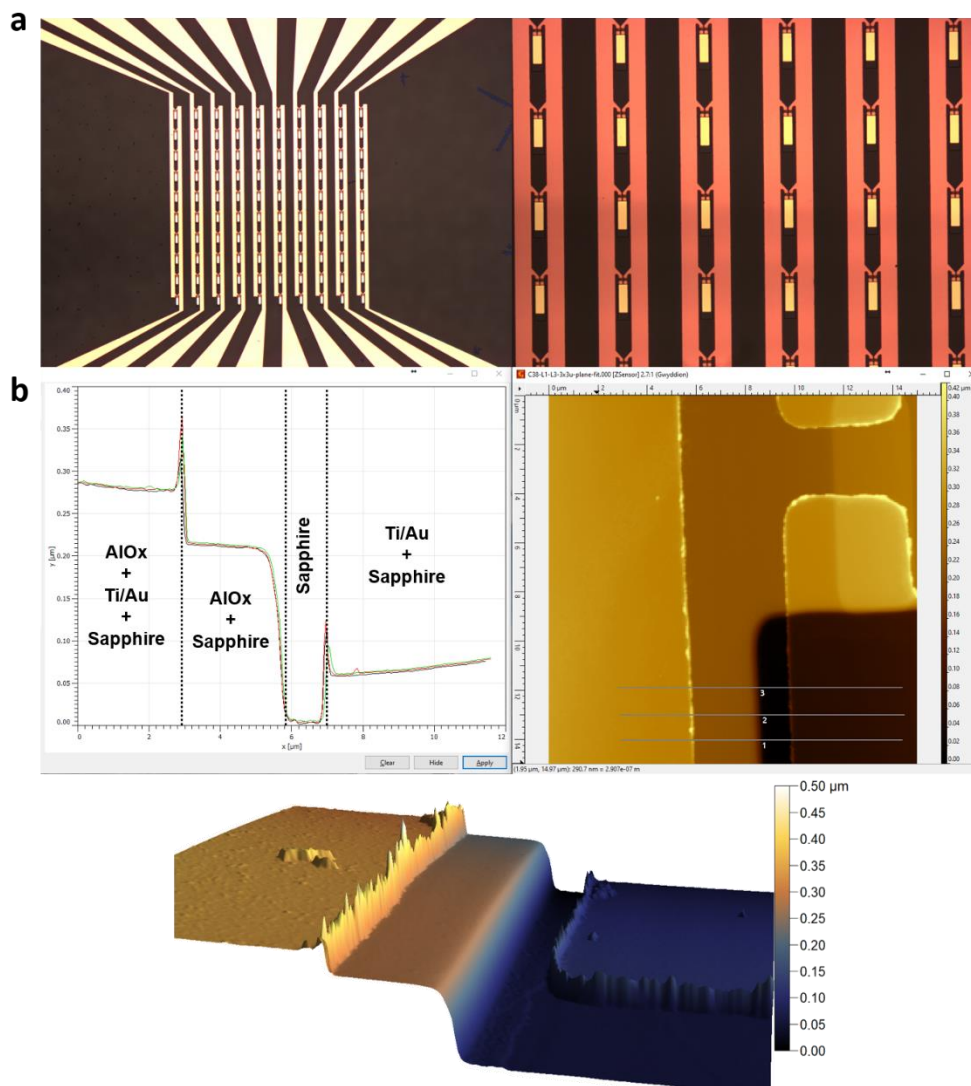


Fig 3.13. VO₂ 2.5D array third layer morphology. **a**, Optical microscope image of VO₂ devices, left and right signal lines, ground line contact pad with AlO_x insulating spacer layer. **b**, The Surface structure and height profile acquired from the AFM scan.

Next, the AlO_x insulating spacer layer will be deposited. In order to avoid the same side-wall defect caused by the positive tone photoresist, double layer resist with undercut structure was utilized. Negative tone photoresist (ARN-4340, Allresist) on the top of the Bottom Resist AR-BR 5480 was patterned cover the ground line contact pad area (dose: 230, defocus: -8). After that, the AlO_x insulating spacer layer was deposited by the AJA e-beam evaporator. After lift-off process, it can be determined from the AFM height profile that the thickness of the deposited AlO_x insulating spacer layer was about 220 nm. A smooth transition from the [sapphire substrate/AlO_x] region to [sapphire substrate] region without side-wall defect can be seen. However, residual side-wall defect can still be observed at the transition area between the [sapphire substrate/AlO_x] region and the [sapphire substrate/AlO_x/Ti/Au] region, and between the [sapphire substrate] region and the [sapphire substrate/Ti/Au] region, as shown in **Fig 3.13b**. Necessary polishing can be used to further remove the side-wall defect.

Finally, same as introduced in section 3.3, positive tone photoresist (ARP-3540T, Allresist) was patterned on the VO₂ thin film to define the ground line area (dose: 110, defocus: -6). And then Ti and Au (~ 100 nm) was deposited by sputtering deposition in scia coat 200 sequentially to from the ground line on the top (shown in **Fig 3.14**). (Test of multiple devices on the array see Appendix)

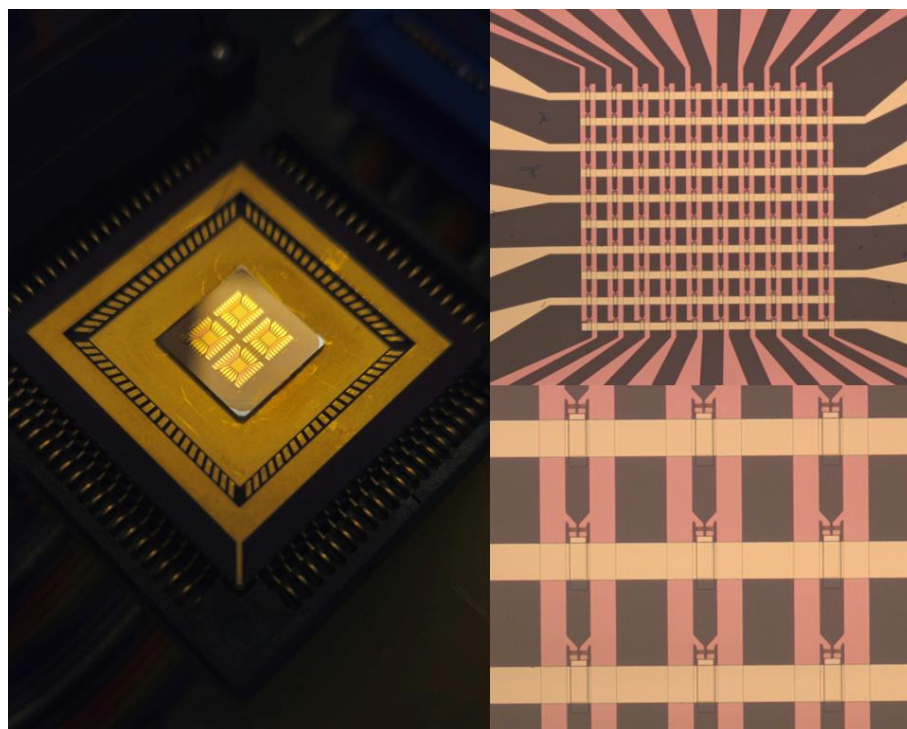


Fig 3.14. VO₂ 2.5D array. Left: 4 identical 10×10 VO₂ LIF neuron crossbar array on the test board. Right top and down: Optical microscope images of VO₂ crossbar array and devices. Left and right signal lines, ground lines can be clearly seen.

Chapter 4 Thermally Coupled VO₂ Oscillators for Boolean Computation

In this chapter, it will be demonstrated that without any extra electronic components needed, self-sustained VO₂ oscillators ranging by more than an order of magnitude in size from 6 μm to 200 nm can be thermally coupled together. A simple but effective mean to actively tune the thermal coupling between VO₂ oscillators will be introduced. And a multiplicity of synchronous oscillatory states with distinct frequencies and amplitudes generated by this effective tuning mechanism can be used for computation. Various oscillation states generated by pairs of coupled oscillators are utilized to realize 12 basic Boolean logic operations from AND, NAND and NOR gates.

4.1 Scalability of VO₂ Oscillators

Firstly, in order to investigate the scalability of VO₂ oscillator, $\rho - T$ (resistivity versus temperature) measurements are carried out to check the change of the typical hysteresis loop with VO₂ device dimension. For temperature dependent resistance measurements, a physical property measurement system (PPMS) was used with a conventional 4-point resistance measurement scheme, and a cooling and warming rate of 5 K/min (from 270 K to 395 K). For the 4-point measurements (Keithley 6221 ac/dc current source and 2182a nanovoltmeter), 1 μA DC current was applied to the sample to minimize the effect of Joule heating. $\rho - T$ Curves from devices with dimensions of 70×40 μm², 7×6 μm², 1×1 μm², and 600×700 nm² are shown in **Fig 4.1**. It shows that the $\rho - T$ hysteresis loop becomes smaller with decreasing dimension due to a spatial confinement effect. Such scaling effect in the $\rho - T$ loop originates from the coexistence of different numbers of metallic and insulating phase domains near the transition temperature. When there is a single domain (~ 20 nm), either in metallic or insulating phase, an ideal one-step change in resistivity around the metal-to-insulator transition (MIT) temperature can be observed [123]. However, direct observation of metallic and insulating phase domains mixture around the MIT temperature suggested that the MIT temperature of different domains also varies. When the phase transition region becomes larger (several hundred nm or μm), numerous metallic and insulating phase domains form the gradual resistivity change loop. The

distribution of the metallic phase domains around the MIT temperature can be statistically modeled as Gaussian function [123]:

$$f(T) = \frac{1}{\sqrt{2\pi\sigma^2}} \exp\left[-\frac{(T-T_{center})^2}{2\sigma^2}\right] \quad (4.1.1)$$

Where σ is the half width of the Gaussian distribution, and T_{center} is the temperature where the population of metallic phase domains is equal to that of insulating phase domains. When the dimension is increased, the distribution of metallic phase and insulating phase domains will become broader, which leads to a larger hysteresis loop.

When the VO₂ devices are scaled down, the resistivity is lower in the insulating state (smaller ρ - T hysteresis loop) reflects the smaller oscillation amplitude and higher oscillation frequency demonstrated in the following parts of the thesis.

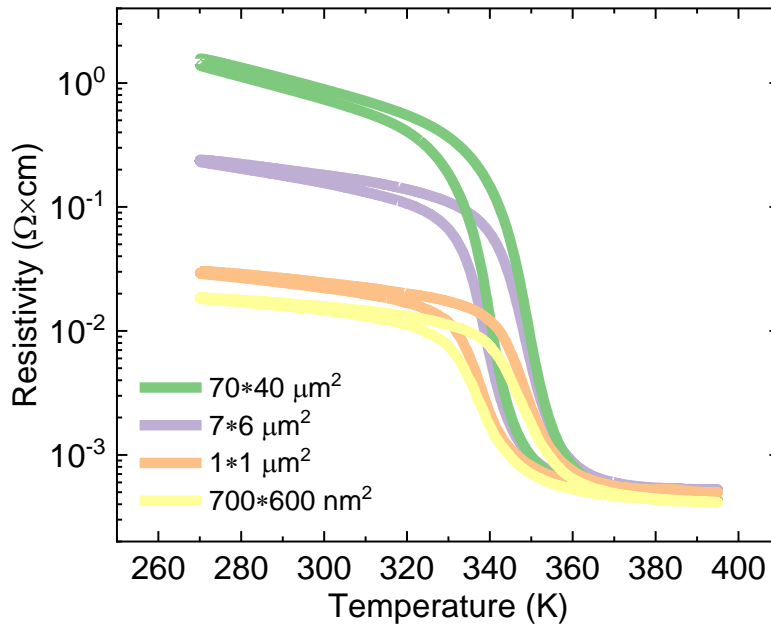


Fig 4.1. ρ - T curves of VO₂ devices with different sizes. Green: 70×40 μm^2 , purple: 7×6 μm^2 , orange: 1×1 μm^2 and yellow: 600×700 nm^2 . Data from [121].

The working principle of the self-sustained VO₂ oscillator driven by constant current source has been introduced in section 2.1.3: Joule heating ($I^2 \cdot R$) plays a critical role in raising the device temperature, and hence drives the oscillation process (between high resistance state and low resistance state). VO₂ device shows a negative differential resistance (NDR) region, where the voltage drops with increasing current, as shown in Fig 4.2. In this region the voltage across the device oscillates with a frequency that increases with the magnitude of the applied current. As introduced in Fig 4.1 where the ρ - T hysteresis loop becomes smaller with decreasing device size, the current (and critical voltage $V_c = I_c R$, where the device enters NDR region) needed to

lift the device temperature up to the vicinity of the MIT temperature also becomes significantly lower when the devices are scaled down from micro-size to nano-size, as shown in **Fig 4.2**.

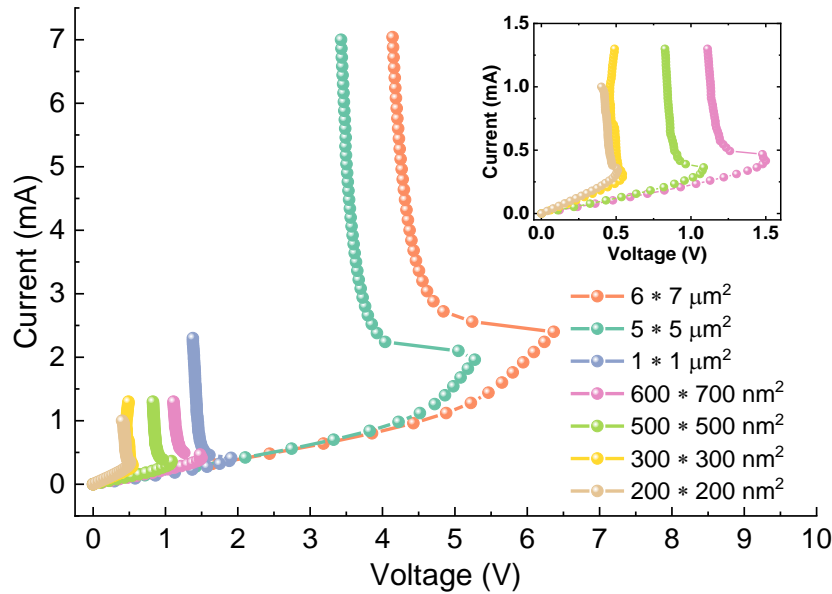


Fig 4.2. I-V curves of VO₂ devices with different sizes. *I-V* measurement (current is varied while measuring voltage) of a single VO₂ device from micron (6×7 μm²) to nanometer scale (200×200 nm²). Inset up right shows the zoom-in view of the *I-V* characteristic from nanoscopic devices. Data from [121].

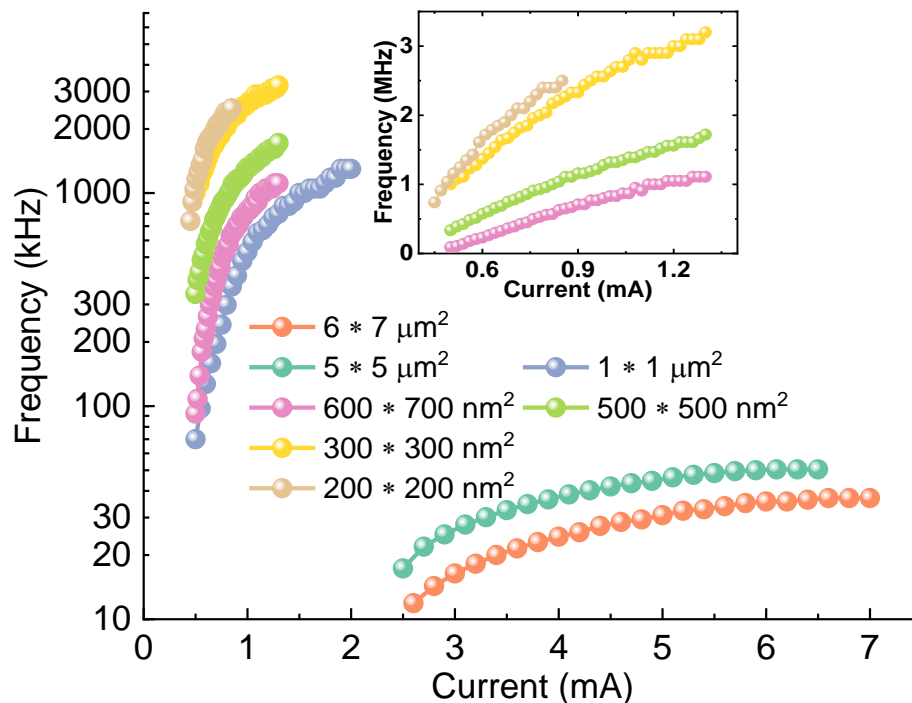


Fig 4.3. I-f curves of VO₂ devices with different sizes. *I-f* measurement (current is varied while measuring oscillation frequency) of a single VO₂ device from micron (6×7 μm²) to nanometer scale (200×200 nm²). Inset up right shows the zoom-in view of the *I-f* characteristic from nanoscopic devices. Data from [121].

As this self-sustained VO₂ oscillator (driven by constant current) is scaled down to 200 nm, a substantial increase in the oscillation frequency (**Fig. 4.3**) from kHz range to MHz range can be observed. The effect can be understood as due to the decreasing number of insulating phase domains when scaling down, the incubation time needed to switch them has become shorter, and hence the device oscillation period (total time of switching to low resistance state, and recovering back to high resistance state) becomes shorter. For the oscillation state measurements with various types of devices, the measurements were carried out in a multi-probe cryogenic probe station (Lakeshore) with 25 μm diameter W-tips. A current source (Keithely 6221 AC/DC current source) and a source meter (Keithely 2636B) were used to drive the oscillators and the thermal cell. The oscillating voltage was detected by an oscilloscope (DSO5052A, InfiniiVision) with home-built LV codes.

In **Fig. 4.4**, the minimum power for driving VO₂ cells into stable oscillation state vs. device size is plotted. It clearly shows a linear relationship between power and device size (fitted in orange dash line). The linear relationship is also confirmed in simulation (green dash line, see finite element simulation for detail in Appendix section). It is remarkable that the oscillation frequency increases above 1 MHz while power decreases down to micro watts with scale-down of the device's size - this clearly indicates faster speed and lower energy consumption with the reduced dimension of the VO₂ oscillator.

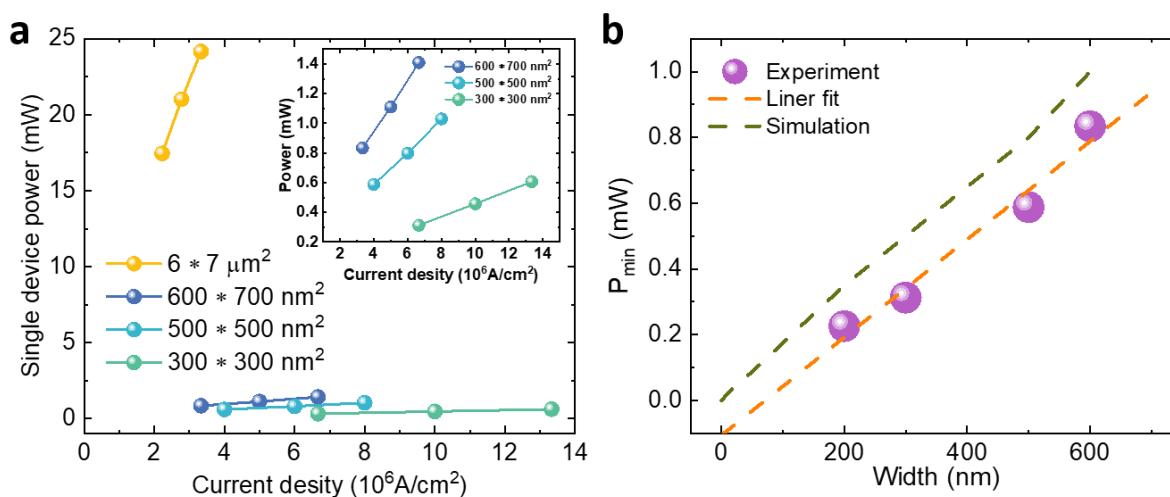


Fig 4.4. Driving power of VO₂ devices with different sizes. a, Single nanoscopic device from micron (6×7 μm²) to nanometer scale (300×300 nm²). Power versus supply current density. Inset up right shows the zoom-in view of the driving power from nanoscopic devices. **b**, The minimum power P_{min} to drive the VO₂ nano oscillator into stable oscillation with various sizes (Purple spheres: experimental data; Orange dashed line: Linear fit of experimental data; Green dashed line: Simulation results from Zhong Wang). Data from [121].

When two VO₂ oscillators are placed close enough, the heat that is released during one part of the oscillation cycle from one device can trigger the nearby device to oscillate, as shown in **Fig 4.5a**. Interestingly, this mechanism should lead to a time delay (or a phase difference) in the oscillations of the two devices. To explore this phenomenon, pairs of VO₂ oscillators of different sizes from 5×5 μm² to 200×200 nm² were fabricated. For a pair of VO₂ devices with the size of 5×5 μm² with a 2 μm spacing, device 1 was set in a stable oscillatory state using a driving current $I_1 = 2.8$ mA (400 μs pulse) above threshold, while device 2 was biased with a sub-threshold current $I_2 = 2.3$ mA. As shown in **Fig. 4.5c**, device 1 oscillates only within the current pulse window. It is intriguing that device 2 also oscillates at a sub-threshold current, triggered by the thermal energy exchange from the oscillating device 1 (consistent with COMSOL finite element simulation, see Appendix section). Note that the thermal energy exchange can be directly observed as follows: In the first half of the periodic driving cycle, I_1 is large enough to drive device 1 at a stable oscillation (green curve), and device 2 is triggered to oscillate (orange curve) at the same frequency as device 1. Then I_1 drops to 0 mA in the second half of the cycle and its voltage, V_1 , decreases to 0 V, while device 2 recovers to the sub-threshold transition state (high resistance state) and its voltage, V_2 , increases back to a high level. In the next cycle when I_1 is turned on, both devices will again start to oscillate at the same frequency, as shown in **Fig. 4.5d**. The trigger delay time between the drop of V_1 and that of V_2 can be seen from the bottom inset.

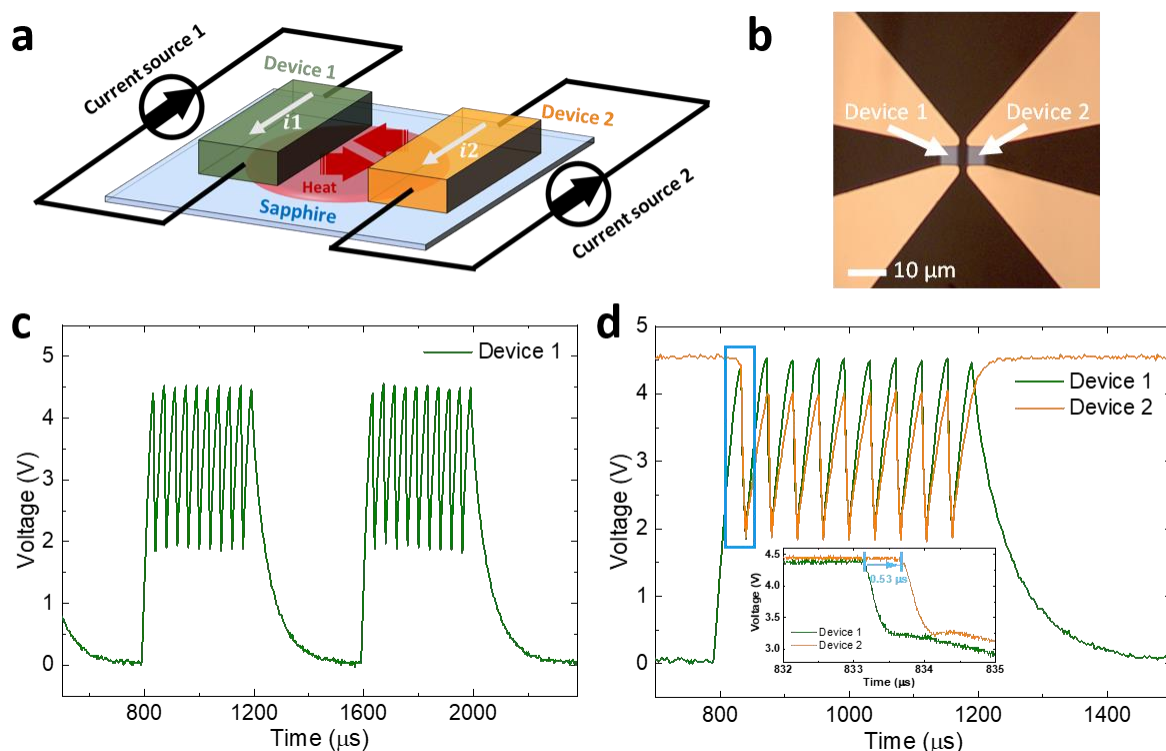


Fig 4.5. Direct observation of thermal coupling effect with trigger delay time between two coupled VO₂ oscillators. **a**, Schematic illustration of two thermally coupled VO₂ oscillators. **b**, Optical images of device 1 (5×5 μm²) and device 2 (5×5 μm²) separated by 2 μm. **c**, Stable oscillation when 400 μs long 2.8 mA current pulses (separated by 400 μs of zero current) are sent to device 1. **d**, Coupled oscillation behavior between device 1 and device 2 (both 5×5 μm²) with 2 μm spacing. Device 2 is excited by $I_2 = 2.3$ mA that is lower than the oscillation threshold current (2.5 mA). When device 1 is activated to oscillation state by a current pulse, device 2 starts to oscillate with the same frequency. Inset (bottom): 0.53 μs to trigger device 2 into oscillation. Data from [121].

Such a thermal triggering effect can be observed for pairs of devices ranging from 5 μm down to 200 nm in size. The trigger delay time increases with increased spacing, as shown in **Fig. 4.6**. For the smallest size (200 nm) the trigger delay time is about 98 ns.

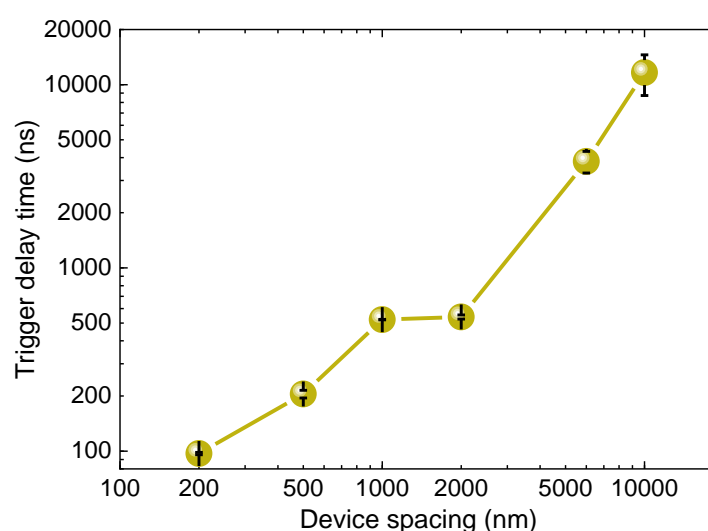


Fig 4.6. Driving power of VO₂ devices with different sizes. **a**, Single nanoscopic device from micron (6×7 μm²) to nanometer scale (300×300 nm²). Data from [121].

Fig 4.7 shows the details of measuring trigger delay time for two VO₂ devices with various device spacing. Same as introduced in **Fig 4.5**, device 1 was set in a stable oscillatory state using a driving current I_1 above threshold, while device 2 was biased with a sub-threshold current I_2 to be thermally triggered to oscillate by device 1. In the first column, optical images show device 1 (5×5 μm²) and device 2 (5×5 μm²) separated by **a**, 10 μm, **b**, 6 μm. SEM images of fabricated nanoscopic devices show two VO₂ device with different dimension and spacing **c**, 1×1 μm² (spacing = 1 μm), **d**, 500×500 nm² (spacing = 500 nm) and **e**, 200×200 nm² (spacing = 200 nm). Yellow shading indicates the VO₂ cells (Au contacts are in white). In the second and third columns show: **Fig 4.7a** - measurements ($I_1 = 2.8$ mA, $I_2 = 2.3$ mA) of the trigger delay time at 10 μm spacing, **Fig 4.7b** - measurement ($I_1 = 2.8$ mA, $I_2 = 2.3$ mA) of the trigger delay time at 6 μm spacing, **Fig 4.7c** - measurements ($I_1 = 600$ μA, $I_2 = 420$ μA) of the trigger delay time at 1 μm spacing, **Fig 4.7d** - measurements ($I_1 = 600$ μA, $I_2 = 460$ μA) of the trigger

delay time at 500 nm spacing, **Fig 4.7e** - measurements ($I_1 = 600 \mu\text{A}$, $I_2 = 460 \mu\text{A}$) of the trigger delay time at 200 nm spacing. The error bar of the trigger time delay is calculated from two measurements of the triggered oscillation.

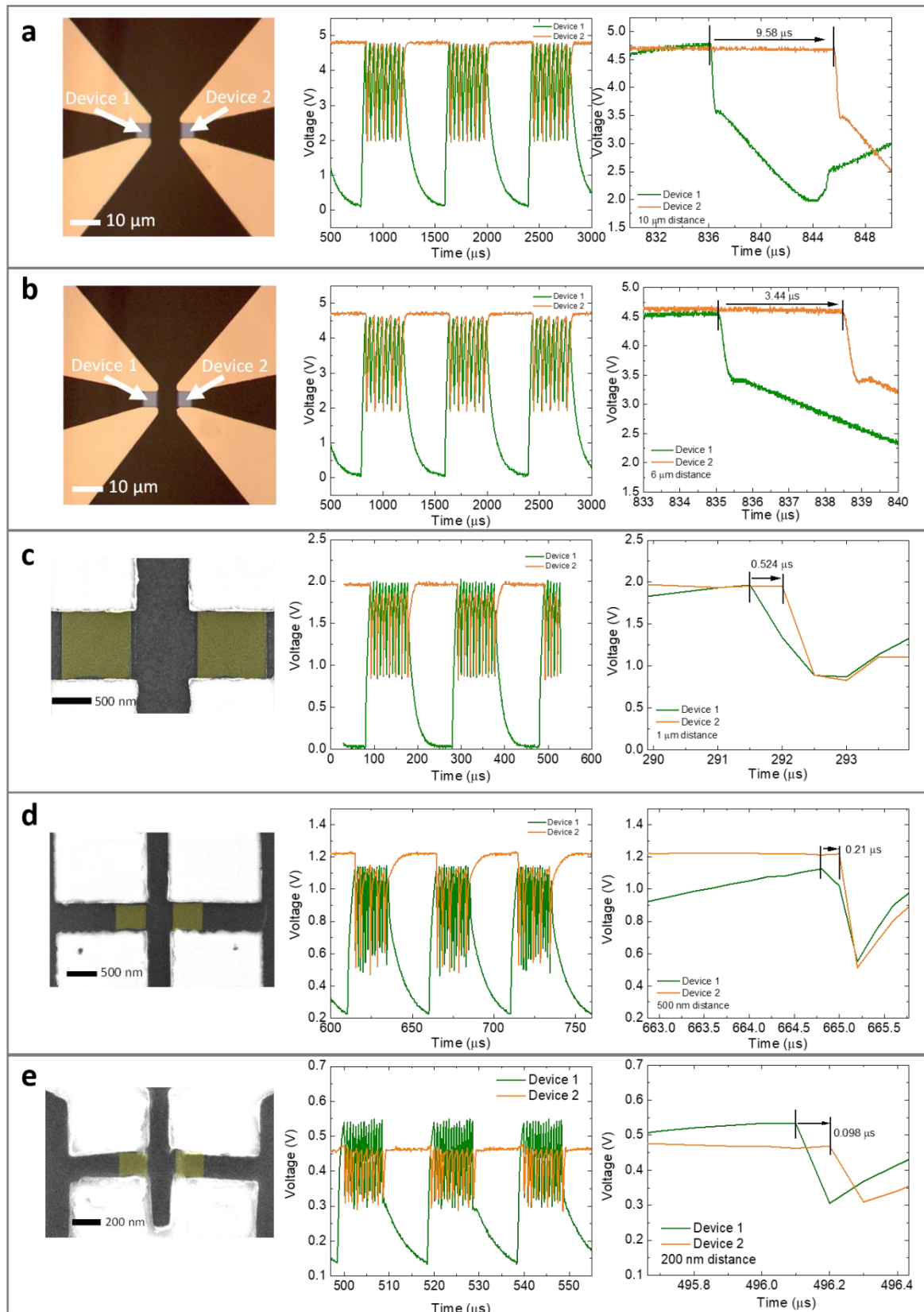


Fig 4.7. Measurement of trigger delay time for two VO₂ devices with various device spacing. Two VO₂ devices **a**, 5×5 μm² (spacing = 10 μm); **b**, 5×5 μm² (spacing = 6 μm); **c**, 1×1 μm² (spacing = 1 μm); **d**, 500×500 nm² (spacing = 500 nm), and **e**, 200×200 nm² (spacing = 200 nm). Data from [121].

4.2 Tunable Thermal Triggering

For a single set of VO₂ oscillators (two devices driven by two independent current sources), the further the devices are apart, the weaker is the thermal link. As shown in **Fig 4.8**, when the spacing between two VO₂ oscillators increases, the frequency locking range becomes smaller significantly. When two devices are far apart, the heat released from one device will dissipate entirely into the substrate before reaching the other device. The thermal coupling strength between the two devices is limited and can only maintain their synchronization within a certain frequency range.

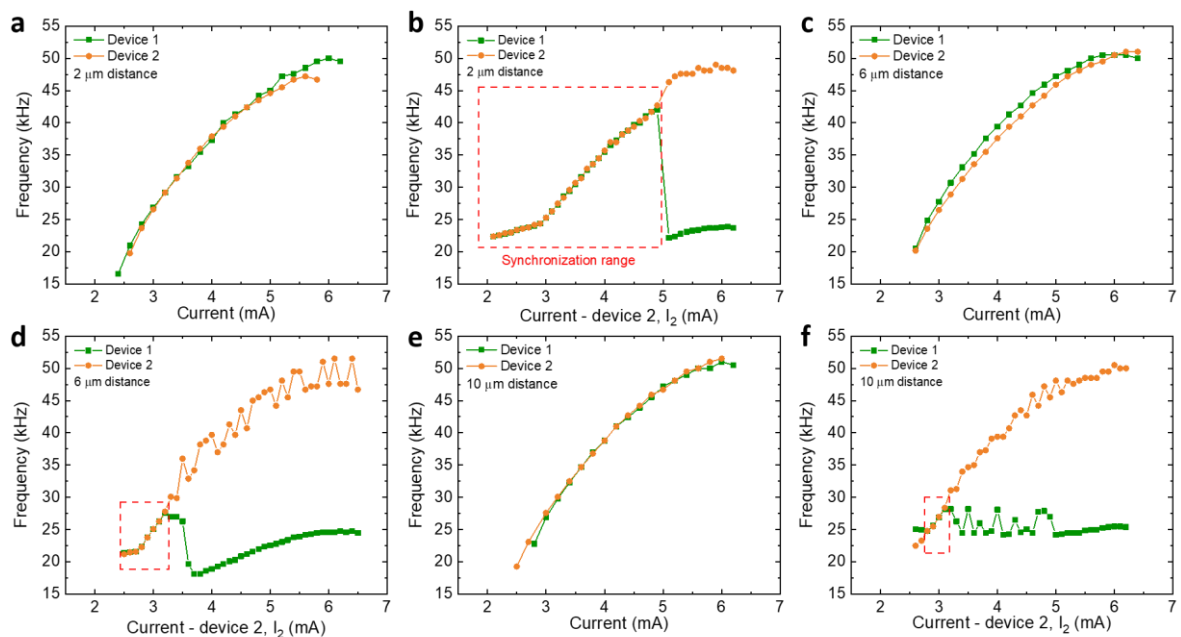


Fig 4.8. Thermal coupling strength versus device spacing. Frequency vs. applied current for device 1 (5×5 μm²) and device 2 (5×5 μm²) when they are oscillating independently with a spacing of **a**, 2 μm, **c**, 6 μm, and **e**, 10 μm. **b**, Frequency locking between device 1 and device 2 at a 2 μm spacing (I_1 fixed at 2.7 mA). **d**, Frequency locking between device 1 and device 2 at a 6 μm spacing (I_1 fixed at 2.6 mA). **f**, Frequency locking between device 1 and device 2 at a 10 μm spacing (I_1 fixed at 2.9 mA). As the spacing between the two VO₂ devices becomes larger (from 2 μm to 10 μm), the coupling strength becomes weaker, shown as a smaller frequency locking range (from 22 kHz to 42 kHz at 2 μm; from 21 kHz to 27 kHz at 6 μm; from 25 kHz to 28 kHz at 10 μm).

Next, in order to realize tunable thermal coupling, a VO₂ thermal cell was added between the two VO₂ devices. The device set morphology is shown in **Fig 4.9**.

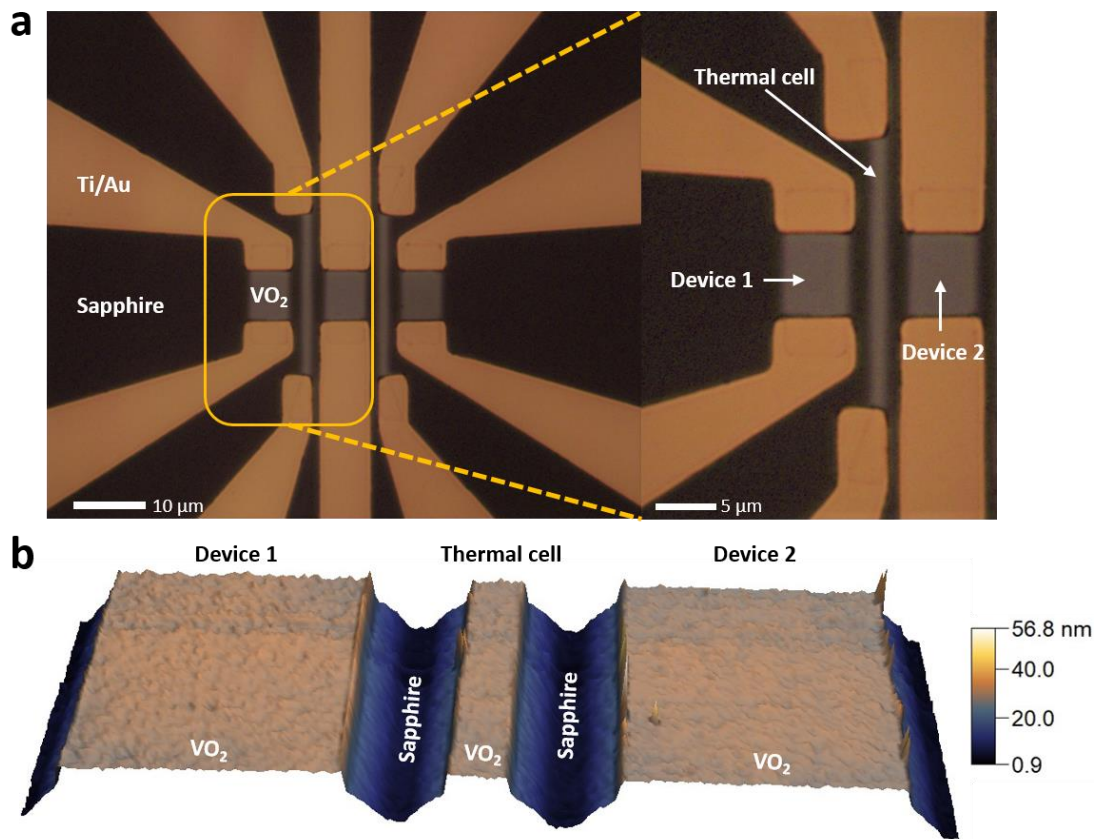


Fig 4.9. Tunable thermal coupling device set geometry. **a**, Optical microscopy images of device set for experiments, with overview (left) and zoomed-in view (right). A 1.5 μm wide (21 μm long) VO₂ stripe is placed as a thermal cell for enhancing the thermal coupling between two VO₂ devices with the dimensions of 7×6 μm². The distance between device 1 and device 2 is 5 μm. **b**, 3D geometry of device 1, device 2 and thermal cell scanned by AFM. Data from [121].

A microscopic picture with a corresponding circuit diagram is shown in **Fig 4.10a**. This thermal cell is designed to change the ambient thermal environment between device 1 and device 2. By applying different cell voltages V_{cell} that induce Joule heating, the ambient temperature between device 1 and device 2 can be changed. The higher the cell voltage V_{cell} , the higher is the ambient temperature, and, therefore, the lower is the threshold switching voltage (as shown in **Fig 4.10b** inset left) and the higher is the oscillation frequency (for the same current, as demonstrated in **Fig 4.10a** inset right) for a single device. This is because the starting point of the oscillation in the $\rho - T$ hysteresis loop has been biased to a higher temperature closer to T_c .

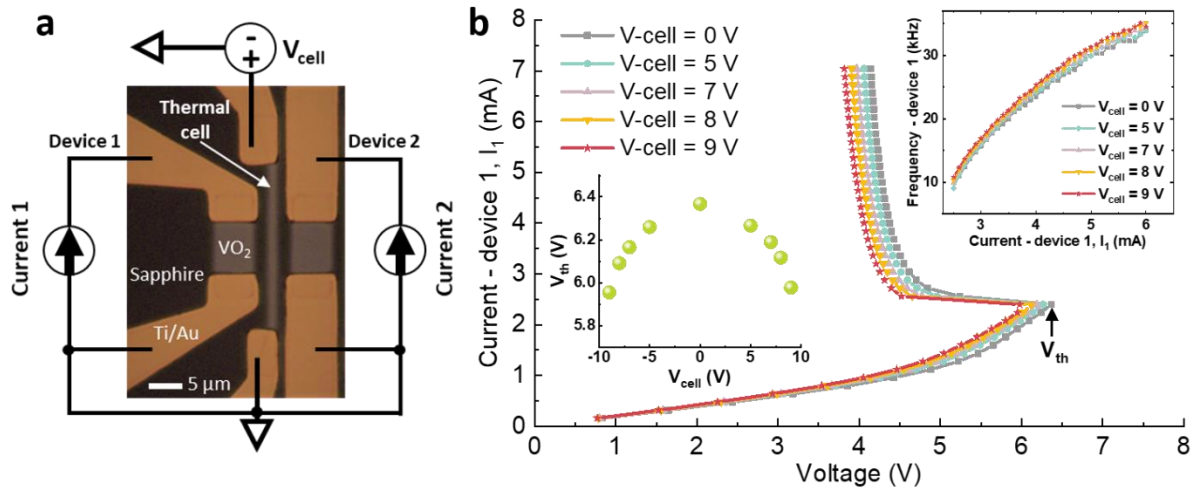


Fig 4.10. VO₂ oscillators with tunable thermal coupling strength. **a**, Optical microscopy image of a device set with schematic illustrations of the electrical connections. The device set includes a 1.5 μm wide (21 μm long) VO₂ stripe as a thermal cell between two VO₂ oscillators, each with dimensions of 7×6 μm². The distance between device 1 and device 2 is 5 μm. Device 1 and device 2 are driven by two independent current sources I_1 and I_2 , respectively. A voltage source V_{cell} is used to control the thermal cell. **b**, I - V measurements (sweep current and measure voltage) of device 1 for different thermal cell voltages (V_{cell}). Inset bottom left: The threshold voltage (V_{th}) where the device enters the NDR region reduces with increasing V_{cell} . Inset top right: I - f measurements (sweep current and measure frequency) from device 1 for different V_{cell} . With higher V_{cell} , f increases. Data from [121].

In the following, how the devices' ambient temperature plays a critical role for the oscillation coupling among neighboring devices including the thermal cell will be further discussed. When the ambient temperature is set at 295 K, 330 K, and at 360 K (above its MIT temperature ~ 340 K), it can be observed that the I - V characteristic changes significantly (**Fig 4.11a**). Below its MIT temperature, VO₂ device still shows a typical NDR region, where the critical current/voltage to enter the region decreases with increasing temperature. However, above its MIT temperature the I - V characteristic of the VO₂ device behaves like normal metal with linear and low resistance, indicating it has fully phase transitioned to metallic state. The other common behavior of VO₂ cell is that the oscillation frequency increases by increasing the ambient temperature while reducing the amplitude, as shown in **Fig 4.11b** and **c**. At the same temperature with different supply currents the oscillation amplitude hardly changes. At higher temperatures the amplitude becomes smaller (at 295 K: peak-to-peak value is about 4.1 V, while at 330 K: peak-to-peak value is about 3.2 V).

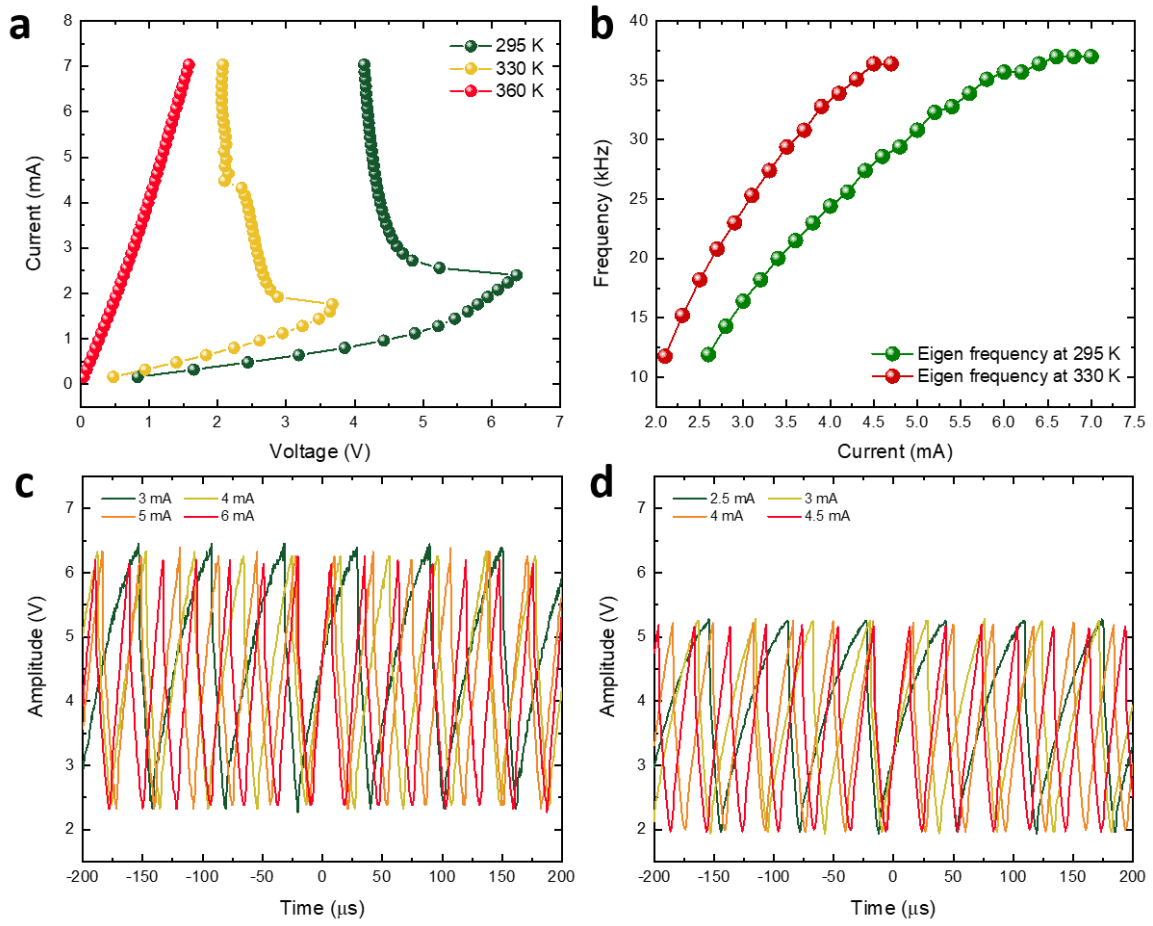


Fig 4.11. Temperature-dependent VO₂ oscillator characteristics. **a**, *I*-*V* measurements (sweep current and measure voltage, voltage compliance at 20 V) at 295 K, 330 K and 360 K. **b**, Oscillation frequency as a function of applied d.c. current (*I*-*f*) for VO₂ device (7×6 μm²) at 295 K and 330 K. At higher ambient temperature, with the same supply current the VO₂ device oscillates at a higher frequency but the tunable frequency range becomes narrower. Additionally, the threshold current value where VO₂ device starts to oscillate decreases at higher temperatures. **c**, Single device (7×6 μm²) oscillation waveform at 3 mA, 4 mA, 5 mA, 6 mA at 295 K. **d**, Single device (7×6 μm²) oscillation waveform at 3 mA, 4 mA, 5 mA, 6 mA at 330 K. Data from [121].

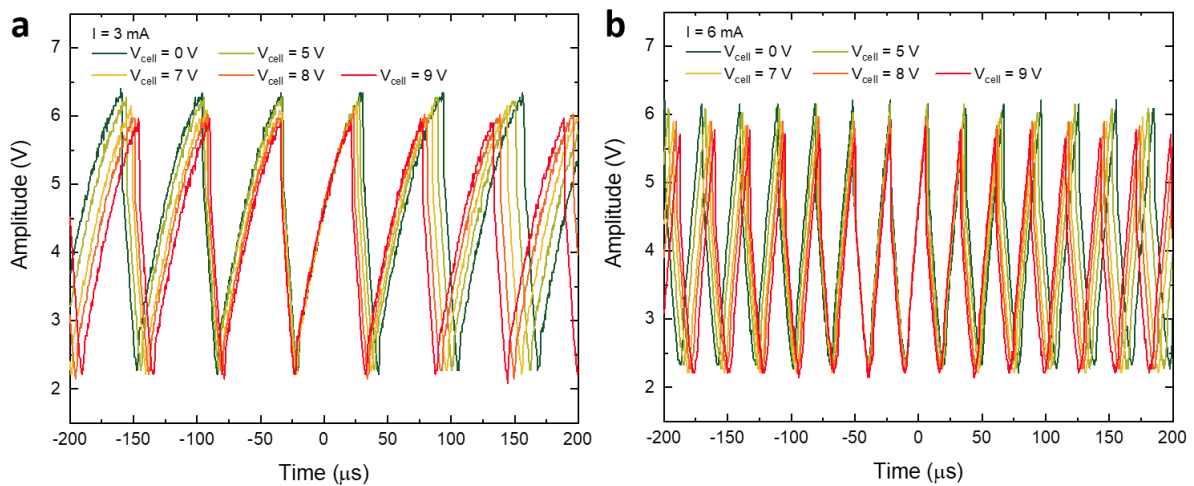


Fig 4.12. Single device oscillation waveform at different supply currents and thermal cell

voltages. a, Single device ($7 \times 6 \mu\text{m}^2$) oscillation waveform at 3 mA at 295 K for different thermal cell voltages V_{cell} . **b**, Single device ($7 \times 6 \mu\text{m}^2$) oscillation waveform at 6 mA at 295 K for different thermal cell voltage V_{cell} . Data from [121].

Applying a constant voltage to the thermal cell has the equivalent effects of raising the ambient temperature that increases the oscillation frequency while lowering the amplitude, as shown in **Fig 4.10a** and **Fig 4.12**. For higher thermal cell voltages, the device oscillates at a higher frequency with a smaller amplitude.

As a result, activating the thermal cell during synchronization helps device 1 (with a constant current I_1 that is lower than the oscillation threshold current) to oscillate at a higher frequency following device 2's frequency as I_2 is gradually increased. As shown in **Fig 4.13a** and **b**, activating the thermal cell will lead to an increase of the mutual synchronized frequency when device 1 and device 2 are already in a synchronized state. When device 1 and device 2 are already desynchronized, activating the thermal cell will lead to an increase of the oscillation frequency while lowering the oscillation amplitude of device 1, which enables device 1 to be synchronized to device 2, as shown in **Fig 4.13c** and **d**.

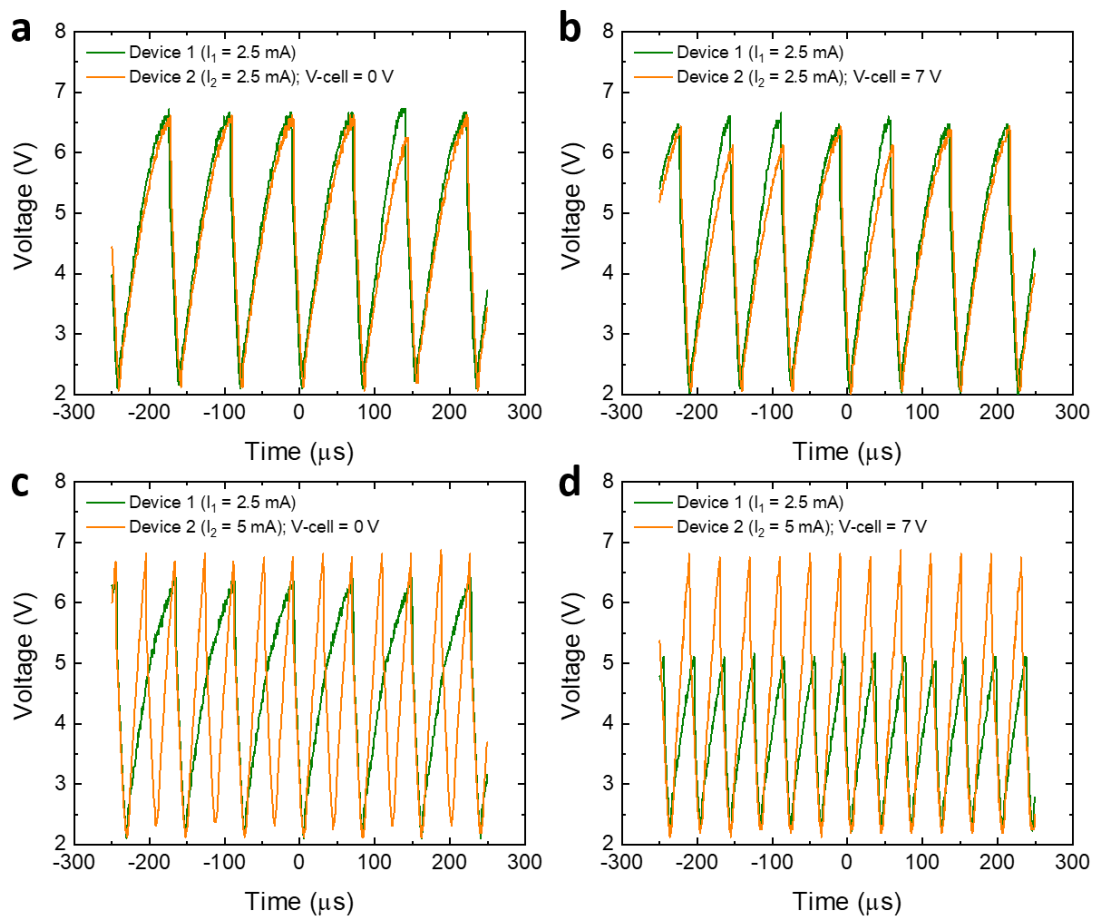


Fig 4.13. Double device oscillation waveforms under synchronization and desynchronization situations. a, Device 1 ($7 \times 6 \mu\text{m}^2$) and device 2 ($7 \times 6 \mu\text{m}^2$) synchronized

oscillation waveforms at $I_1 = I_2 = 2.5$ mA, $V_{cell} = 0$ V. **b**, Device 1 and device 2 synchronized oscillation waveforms at $I_1 = I_2 = 2.5$ mA, $V_{cell} = 7$ V. **c**, Device 1 and device 2 desynchronized oscillation waveforms at $I_1 = 2.5$ mA, $I_2 = 5$ mA, $V_{cell} = 0$ V. **d**, Device 1 and device 2 synchronized oscillation waveforms at $I_1 = 2.5$ mA, $I_2 = 5$ mA, $V_{cell} = 7$ V. Data from [121].

The tunable thermal triggering is presented as follows (shown in **Fig 4.14**): For the case where the thermal cell is not activated ($V_{cell} = 0$ V), device 1 was supplied with a constant low current I_1 (2.4 mA) and oscillates at a low frequency (11 kHz). By gradually increasing the supply current I_2 for device 2, the frequency of device 1 (f_1) and the frequency of device 2 (f_2) are synchronized until a critical frequency (here 23.5 kHz). When f_2 is further increased, due to the limited thermal coupling strength, f_1 first drops to a value that is about one half of f_2 and then increases slowly while maintaining a ratio of $f_1 : f_2$ of roughly 1 : 2, as shown in **Fig 4.14a**. For the case where the thermal cell is activated with a very strong thermal coupling strength ($V_{cell} = 8$ V), f_1 can now be fully locked to f_2 (until both devices are heated to their respective metallic states and don't oscillate anymore). The significant difference between the synchronization behavior of device 1 under weak/moderate ($V_{cell} < 8$ V) and strong ($V_{cell} = 8$ V) coupling effects can be observed, as shown in **Fig 4.14c**.

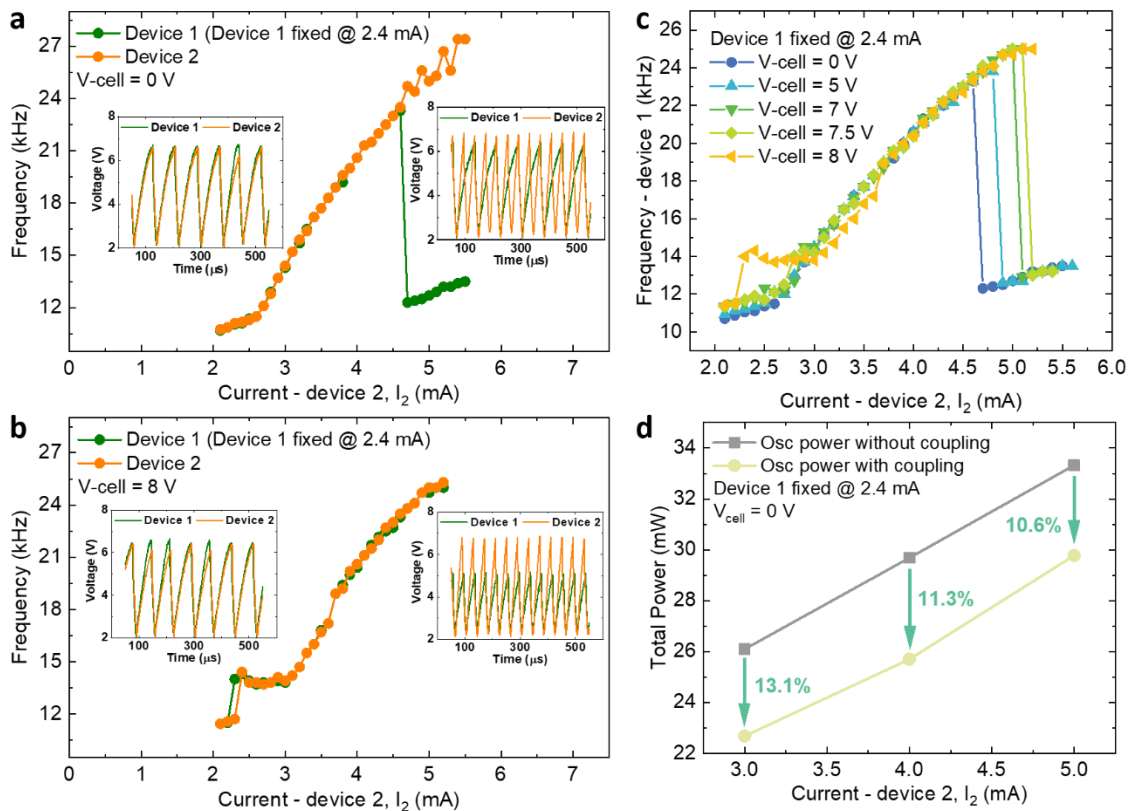


Fig 4.14. Tunable thermal triggering between two VO₂ oscillators. **a**, Frequency locking at $V_{cell} = 0$ V. I_1 is fixed at 2.4 mA while increasing I_2 . In this case, the frequency locking between device 1 and 2 holds until 23.5 kHz. Inset left: Synchronized waveforms of device 1 ($I_1 = 2.4$ mA) and device 2 ($I_2 = 2.5$ mA). Inset right: Desynchronized waveforms of device 1 ($I_1 = 2.4$

mA) and device 2 ($I_2 = 5$ mA). **b**, Frequency locking at $V_{cell} = 8$ V. The frequency locking breaks above 25.3 kHz. Inset left: Synchronized waveforms of device 1 ($I_1 = 2.4$ mA) and device 2 ($I_2 = 2.5$ mA). Inset right: Synchronized waveforms of device 1 ($I_1 = 2.4$ mA) and device 2 ($I_2 = 5$ mA). **c**, Comparison of synchronization frequency of device 1 (fixed at 2.4 mA) as V_{cell} is varied (from 0 to 8 V). **d**, Comparison of power consumption from device 1 and device 2 under different circumstances at $V_{cell} = 0$ V. Gray line shows the power summation when they are oscillating independently. Yellow line shows the power summation when they are oscillating with the coupling effect. Data from [121].

As mentioned in section 2.1.3, the energy-recycling mechanism - energy being reversibly converted, or reused, instead of being totally dissipated, is also a very attractive point for developing energy-efficient oscillatory computational network. Because in traditional CMOS circuit there is no such energy-recycling mechanism - power increases (proportionally) with the number of transistors. The power consumption from device 1 and device 2 when they are oscillating indecently, and when they are oscillating with a thermal coupling effect (as shown in Fig 4.14d) are plotted, respectively. The thermal energy exchange between device 1 and device 2 helps to reduce the power consumption both in the synchronization region (by 13.1 %) and the non-synchronization region (by 10.6 %), indicating higher energy efficiency. The power of a single oscillator is calculated as follows: The oscillating voltage waveform under a certain current value is collected. Then the voltage value is averaged over time (500 μ s) then multiplied by the current value to obtain the average power consumption. The power of the thermal cell is calculated approximately from the measurements in Fig 4.15.

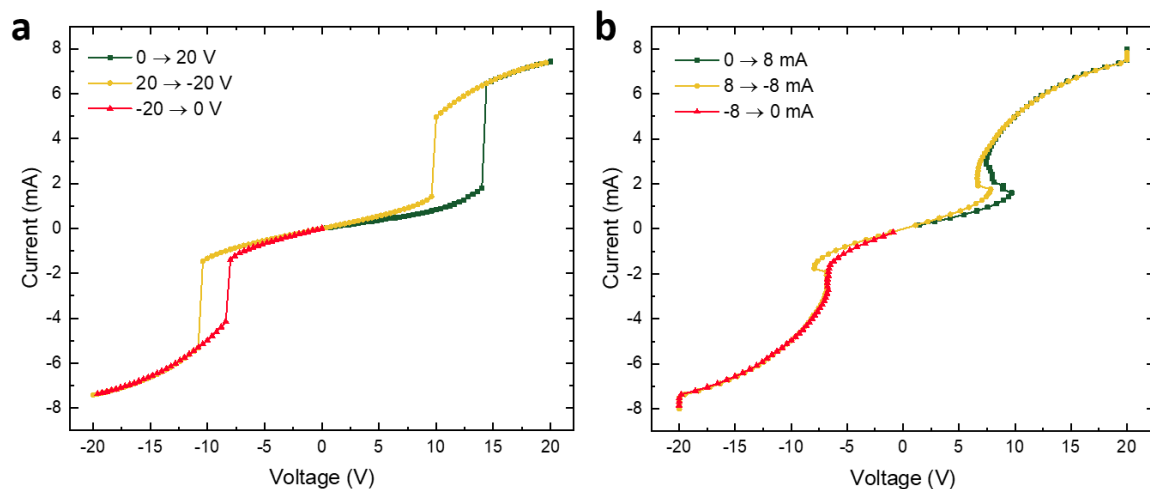


Fig 4.15. Voltage-mode (V-I) and current-mode (I-V) measurements for a thermal cell. a, Thermal cell V-I (sweep voltage and measure current, current compliance at 10 mA) and **b**, I-V (sweep current and measure voltage, voltage compliance at 20 V) curves. Data from [121].

Such oscillators with tunable synchronization behavior can be further scaled down to nano-scale as shown in Fig 4.16. The device set includes a 120 nm wide (2 μ m long) VO₂ nano wire as a thermal cell, and two VO₂ oscillators with dimensions of 700 \times 600 nm². The distance

between device 1 and device 2 is 600 nm. The distance between thermal cell and device 1 (or device 2) is 240 nm. Yellow shading indicates VO₂ cells (Au contacts in white).

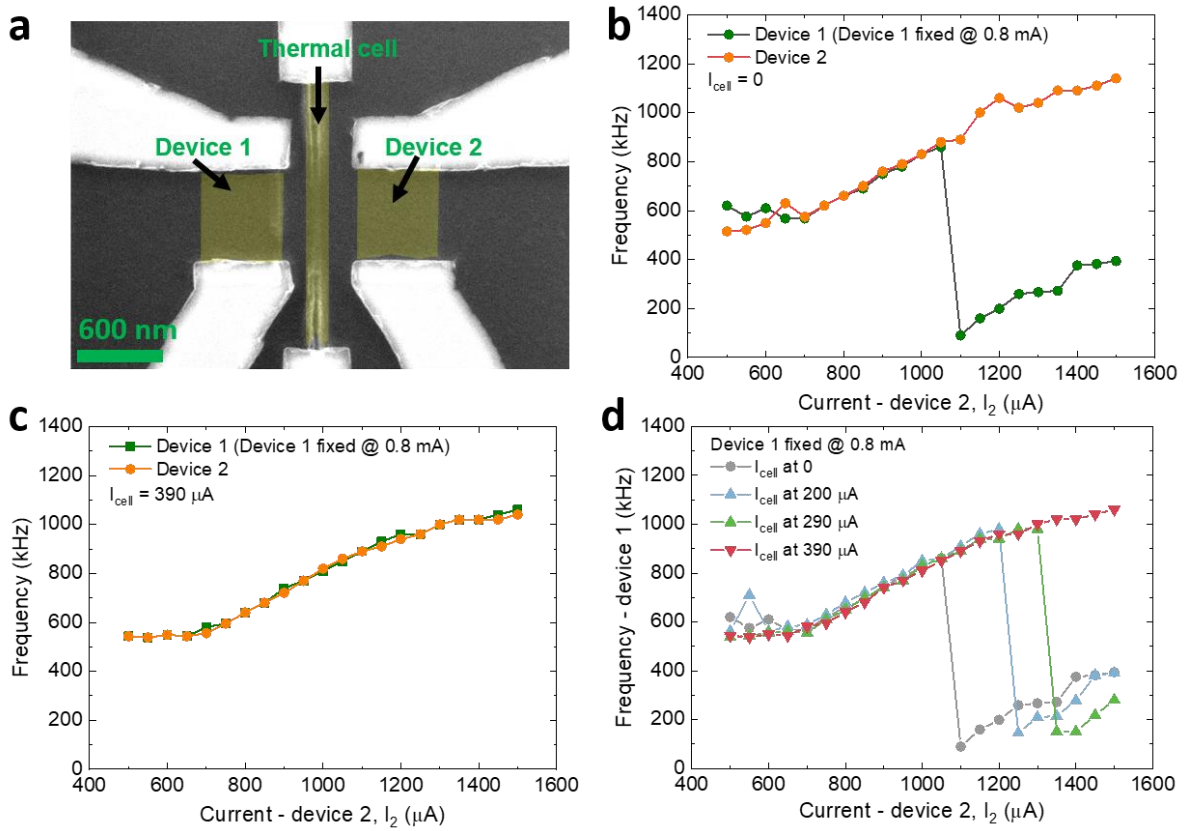


Fig 4.16. VO₂ nano oscillators with tunable thermal triggering. **a**, SEM image of a fabricated nanoscopic device. **b**, Frequency locking behavior at $I_{cell} = 0 \mu\text{A}$. For this measurement, the current to device 1 is fixed at 0.8 mA while the current to device 2 is increased. In this case, the frequency locking between device 1 and 2 holds from 700 kHz to 1.05 MHz and then breaks down. **c**, Frequency locking behavior at $I_{cell} = 390 \mu\text{A}$. In this case, the frequency locking breaks down above 1.5 MHz. **d**, Comparison of synchronization frequency of device 1 (fixed at 0.8 mA) as I_{cell} is varied (from 0 to 390 μA). Data from [121].

4.3 VO₂ Oscillator-based Boolean Logic Gates

Based on the above tunable thermal coupling mechanism, three different Boolean logic gates (AND, NAND and NOR) are realized by the set of VO₂ devices shown in **Fig 4.10a**. The oscillation state of a VO₂ device, which is represented by the oscillation frequency (f) and amplitude (A), is taken as state “0” or “1”. Here we define the threshold frequency f_{th} as the frequency where device 1 and device 2 desynchronize at $V_{cell} = 0 \text{ V}$ when I_1 is fixed at 2.5 mA while I_2 is gradually increasing ($f_{th} = 23.5 \text{ kHz}$ is taken for the following computation). A

frequency lower (higher) than f_{th} is defined as “low (high) frequency”. A peak-to-peak value $V_{pk-pk} = 1$ V is chosen as the threshold amplitude. An amplitude smaller (larger) than V_{pk-pk} is defined as “small (large) amplitude”. There are 4 kinds of oscillation states; high frequency with large amplitude, high frequency with small amplitude, low frequency with large amplitude and low frequency with low amplitude. Here, only the oscillation state with high frequency and large magnitude is taken as logic “1”, while the other states are taken as logic “0”, as shown in **Fig 4.17**.

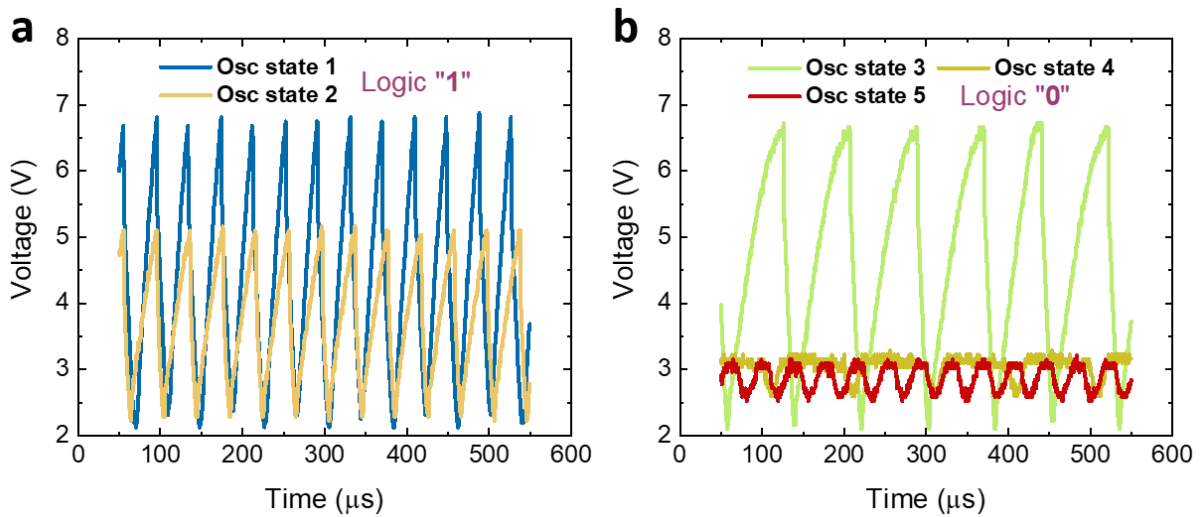


Fig 4.17. Oscillation states used for Boolean computation. a, Oscillation states defined as logic “1”. **b**, Oscillation states defined as logic “0”. Data from [121].

The key to generating different oscillation states is to use the supply current and thermal cell to bias the starting point of the oscillation cycle in the $\rho - T$ hysteresis loop. The oscillation state in **Fig 4.18a**: Device 1 is supplied with constant current of 2.5 mA while the thermal cell is deactivated. The ambient temperature isn’t significantly raised so device 1 oscillates at a low frequency with large amplitude; The oscillation state in **Fig 4.18b**: Device 1 is supplied with constant large current of 6.2 mA with the activated thermal cell. Meanwhile, device 2 is supplied with large current ($I_2 = 5$ mA) and oscillates at a high frequency. Due to the significant rise of ambient temperature by both synchronization and the thermal cell, the high resistance state of device 1 has been biased closely to the metallic point (in the $\rho - T$ hysteresis loop) and this results in a smaller peak-to-peak amplitude (< 1 V) and high frequency; The same also applies to the oscillation state in **Fig 4.18c** when device 1 is supplied with a constant current of 6.4 mA while the thermal cell is activated, and device 2 oscillates at a low frequency ($I_2 = 2.4$ mA); The oscillation state in **Fig 4.18d**: Device 1 is supplied with a constant current of 6.4 mA while device 2 is supplied with a large current ($I_2 = 5.2$ mA) and oscillates at high frequency.

The activation of the thermal cell will lead to overheating of both devices so they reach the metallic state. As a result, there will be no more oscillations, as shown in **Fig 4.18d**.

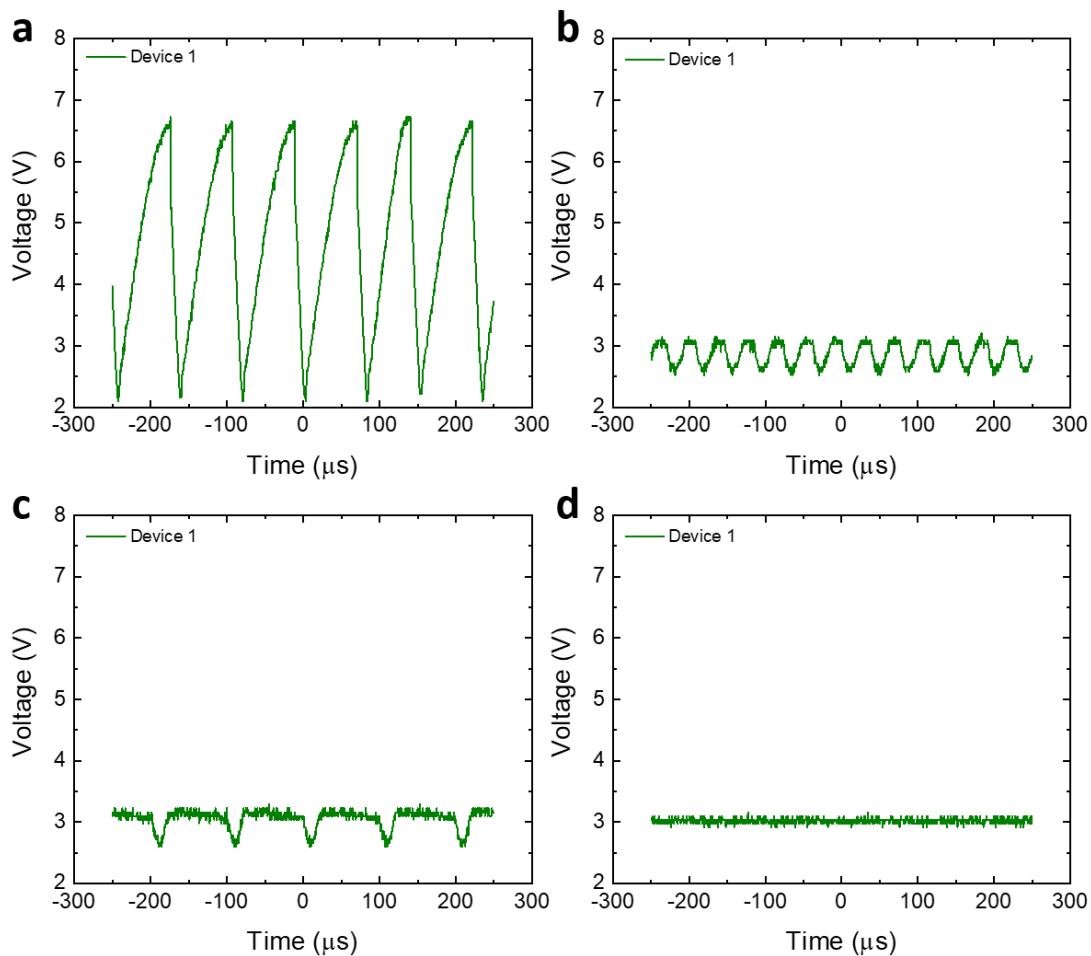


Fig 4.18. Logic “0” represented by different oscillation states of VO₂ device 2. a, Oscillation state with low frequency and large amplitude. **b**, Oscillation state with high frequency and small amplitude. **c**, Oscillation state with low frequency and small amplitude. **d**, No oscillation (fully metallic state). Data from [121].

The oscillation state of device 2 for various I_2 is taken as input A, while the thermal cell voltage V_{cell} represents the input B ($V_{cell} = 0$ (7) V stands for B = 0 (1)). The current through device 1 (I_1) is kept constant during each operation, while the oscillation state of device 1 under input A and input B is taken as the output. 12 Boolean operations from AND gate, NAND gate, and NOR gate are demonstrated in **Fig 4.19**. (Detailed output waveforms from devices 1 and 2 for different logic gates are shown in Appendix section. Boolean-logic calculation tables for AND, NAND, and NOR gate are given in Table. T2).

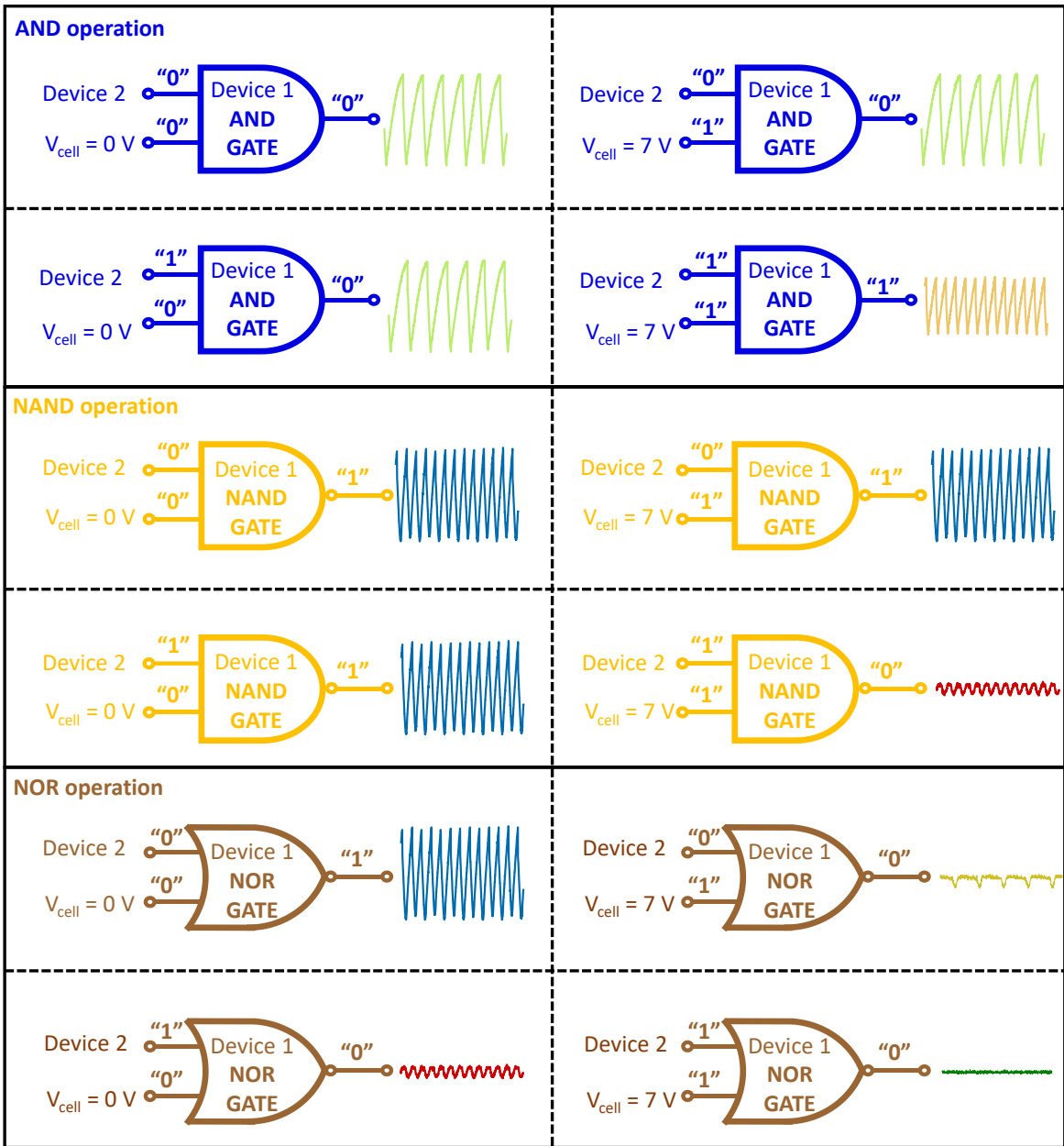


Fig 4.19. Boolean logic gates based on coupled VO₂ oscillators with tunable thermal coupling strength. Operations of AND, NAND, and NOR logic gates. Data from [121].

(a) AND operation:

| Input A (Device 2) | Input B (V_{cell}) | Output AB (Device 1 fixed at 2.5 mA) |
|---|------------------------------|---|
| 0 ($f = 11.9$ kHz, $V_{pk-pk} = 4.4$ V at 2.5 mA) | 0 ($V_{cell} = 0$ V) | 0 ($f = 11.9$ kHz, $V_{pk-pk} = 4.4$ V) |
| 0 ($f = 11.9$ kHz, $V_{pk-pk} = 4.4$ V at 2.5 mA) | 1 ($V_{cell} = 7$ V) | 0 ($f = 14.3$ kHz, $V_{pk-pk} = 4.4$ V) |
| 1 ($f = 30.8$ kHz, $V_{pk-pk} = 4.5$ V at 5 mA) | 0 ($V_{cell} = 0$ V) | 0 ($f = 12.7$ kHz, $V_{pk-pk} = 4.4$ V) |
| 1 ($f = 30.8$ kHz, $V_{pk-pk} = 4.5$ V at 5 mA) | 1 ($V_{cell} = 7$ V) | 1 ($f = 24.4$ kHz, $V_{pk-pk} = 2.7$ V) |

(b) NAND operation:

| Input A (Device 2) | Input B (V_{cell}) | Output \overline{AB} (Device 1 fixed at 6.2 mA) |
|---|------------------------------|---|
| 0 ($f = 11$ kHz, $V_{pk-pk} = 4.4$ V at 2.4 mA) | 0 ($V_{cell} = 0$ V) | 1 ($f = 30.3$ kHz, $V_{pk-pk} = 4.4$ V) |
| 0 ($f = 11$ kHz, $V_{pk-pk} = 4.4$ V at 2.4 mA) | 1 ($V_{cell} = 7$ V) | 1 ($f = 29.4$ kHz, $V_{pk-pk} = 4.1$ V) |
| 1 ($f = 30.8$ kHz, $V_{pk-pk} = 4.5$ V at 5 mA) | 0 ($V_{cell} = 0$ V) | 1 ($f = 30.3$ kHz, $V_{pk-pk} = 4.3$ V) |
| 1 ($f = 30.8$ kHz, $V_{pk-pk} = 4.5$ V at 5 mA) | 1 ($V_{cell} = 7$ V) | 0 ($f = 24.4$ kHz, $V_{pk-pk} = 0.6$ V) |

(c) NOR operation:

| Input A (Device 2) | Input B (V_{cell}) | Output $\overline{A + B}$ (Device 1 fixed at 6.4 mA) |
|---|------------------------------|--|
| 0 ($f = 11.9$ kHz, $V_{pk-pk} = 4.4$ V at 2.5 mA) | 0 ($V_{cell} = 0$ V) | 1 ($f = 31.3$ kHz, $V_{pk-pk} = 4.2$ V) |
| 0 ($f = 11.9$ kHz, $V_{pk-pk} = 4.4$ V at 2.5 mA) | 1 ($V_{cell} = 7$ V) | 0 ($f = 10.1$ kHz, $V_{pk-pk} = 0.6$ V) |
| 1 ($f = 32.3$ kHz, $V_{pk-pk} = 4.4$ V at 5.2 mA) | 0 ($V_{cell} = 0$ V) | 0 ($f = 27$ kHz, $V_{pk-pk} = 0.4$ V) |
| 1 ($f = 32.3$ kHz, $V_{pk-pk} = 4.4$ V at 5.2 mA) | 1 ($V_{cell} = 7$ V) | 0 (no oscillation) |

Table T2. Calculation table of Boolean logic gates. Output logic “0” and “1” are represented by different oscillation states of VO₂ device 1. **a**, AND gate. **b**, NAND gate. **c**, NOR gate. Data from [121].

Chapter 5 Spiking Neural Network based on VO₂ Neurons

In this chapter, it will focus on the applications of thermally coupled VO₂ oscillators in non-Boolean type computation, i.e. neuromorphic computing. Hardware implementations of the Hodgkin-Huxley (H-H) neuron and leaky integrate-and-fire (LIF) neuron, which have been introduced in chapter 2, directly by VO₂ oscillators without any additional electronic circuit elements will be demonstrated. Furthermore, complex spatiotemporal functions including temporal integration and modulation will be experientially demonstrated by multiple interacting VO₂ LIF neurons. In the last section, the performance of large-scale spiking neural networks based on such experimental VO₂ LIF neurons for recognition of MNIST hand-written digits will be presented.

5.1 VO₂ Oscillators-based H-H Neuron

As introduced in section 2.2.2, the Hodgkin-Huxley (H-H) neuron is one of the most sophisticated models that describes the structural, functional and dynamic properties of ion channels, ion permeation and selectivity etc. However, in order to realize the H-H neuron model with basic functions like regular spiking, spike-frequency adaptation, and bursting, a large number of electronic components are required to construct the circuit by traditional CMOS technology [124]. This not only increases the complexity to design a large-scale network architecture based on such neuron, but also limits the degree of freedom to tune the dynamics of the network during operation.

In the following, direct hardware implementation of the Hodgkin-Huxley (H-H) neuron by thermally linking three VO₂ oscillators will be presented. The device set is the same as in **Fig 4.10a**. The difference is that the thermal cell was operated in the I-mode, in which a constant current (I_{cell}) is applied to the thermal cell. This operation mode allows for cascade synchronization among the VO₂ oscillators and the thermal cell. This phenomenon occurs because the VO₂ thermal cell will also oscillate for I_{cell} within the NDR region, and the heat periodically released from it strongly links cell 1 and cell 2 to its own oscillation period. As shown in **Fig 5.1a**, cell 1, cell 2, and the thermal cell are excited with three independent current

sources. When supplied with $I_1 = 3.9$ mA, $I_2 = 4$ mA, and $I_{cell} = 2.3$ mA, frequency locking among the three devices can be observed in **Fig 5.1b**.

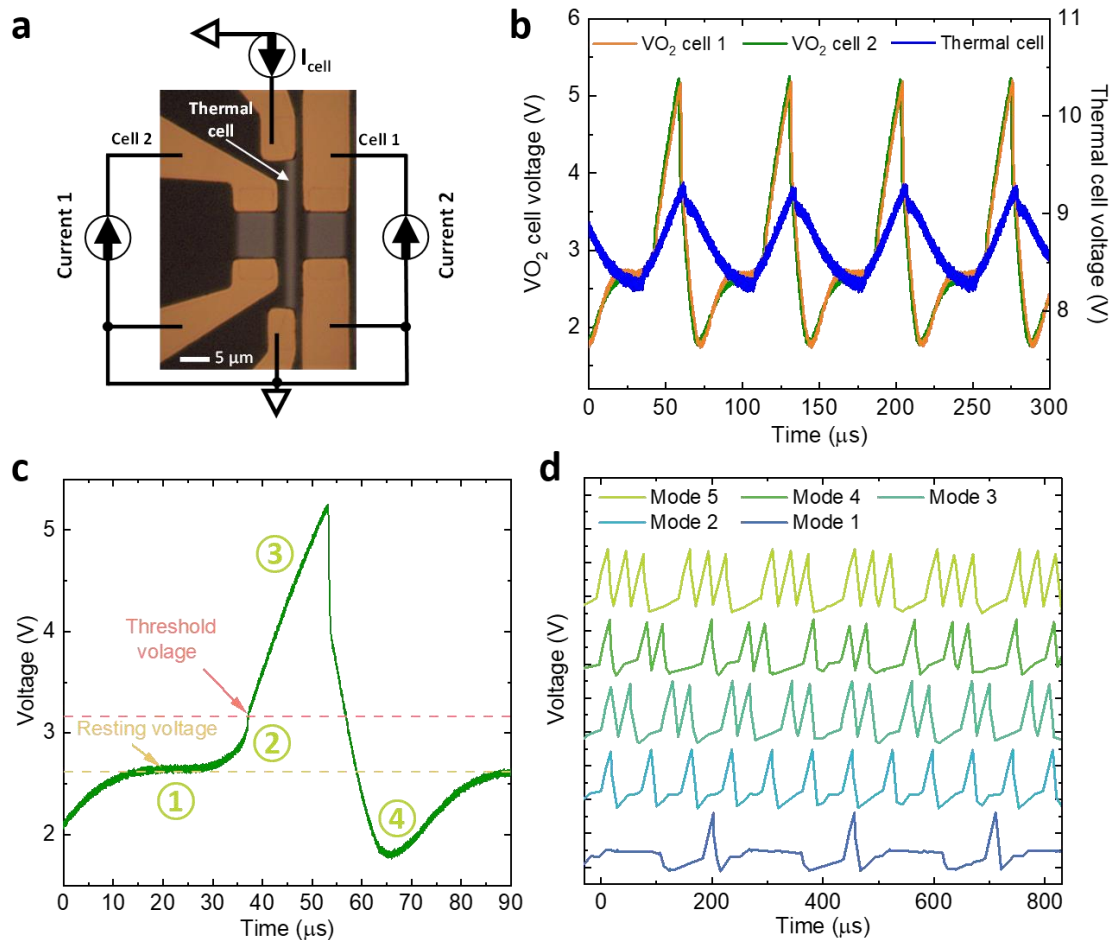


Fig 5.1. Thermal spike driven VO₂ oscillation with different firing modes. **a**, Optical image of the VO₂ device set used for the generation of a spiking potential. Cell 1, cell 2, and thermal cell are excited by three independent current sources. **b**, The oscillation waveform when cell 1 is excited at 3.9 mA, cell 2 is excited at 4.0 mA, and thermal cell is activated at 2.3 mA. **c**, The output waveform from cell 2 that is generated by the cascade synchronization among three cells. This behavior mimics the generation of the spiking potential in a neuron when it is stimulated; Region-1: Resting state; Region-2: Stimulation arrives; Region-3: Depolarization state; Region-4: Repolarization and hyperpolarization state (also known as refractory period). **d**, Different firing modes of the VO₂ neuron by simply changing the current of cell 1 (I_1 from 1 mA to 5.2 mA), while keeping the current to cell 2 ($I_2 = 4$ mA) and thermal cell ($I_{cell} = 2.3$ mA) fixed. Data from [121].

The output waveform of cell 2 is similar to the spiking potential of a neuron when it is stimulated. In biological systems, neurons possess abundant and complex responses to external stimuli so that various spiking neuron models have been established, including tonic spiking and bursting, phase spiking and bursting [125]. As demonstrated in **Fig. 4c**, the output waveform of cell 2 incorporates four typical regions equivalent to when a neuron transforms from a resting state to an excited state [13]. Region-1 corresponds to the resting state when the

neuron is not excited and its potential remains at the resting voltage level. Region-2 is when the stimulation arrives and triggers the neuron potential to rise. Region-3 corresponds to the depolarization state where the potential exceeds the threshold and releases a spike. Region-4 is the repolarization and hyperpolarization state (also known as refractory period) where the potential recovers back to the resting state. By simply adjusting the current through cell 1 (between 1 mA and 5.2 mA) while keeping the currents through cell 2 and the thermal cell fixed ($I_2 = 4$ mA, $I_{cell} = 2.3$ mA), different numbers of spikes (5 different neuron firing modes) can be generated within one firing period from cell 2, as shown in **Fig. 4d**. Among these 5 firing modes, mode 1 and 2 can be considered as tonic spiking neurons that fire one spike within one period, while mode 3, 4 and 5 can be compared to tonic bursting neurons that fire multiple spikes periodically [126 - 128]. Details of synchronous waveforms from cell 1, cell 2 and thermal cell are shown in Appendix.

Neural network based on the H-H neuron model with bursting properties like high frequency, high reliability, and strong stimulation to postsynaptic neurons, has the advantages of triggering responses very quickly by incoming signals compared with traditional computing platform, and has been applied in the robot system for avoidance control very recently [129].

5.2 VO₂ Oscillators-based LIF Neuron

Leaky integrate-and-fire (LIF) neuron, as introduced in section 2.2.2, is the simplified version the Hodgkin-Huxley (H-H) neuron with one channel dynamics. The advantages of using LIF neuron to construct large-scale spiking neural network (SNN) at current stage are that: 1. The neuron model has lower complexity, and hence will be easier to manipulate and tune its properties; 2. Abundant algorithms studied by previous works have made it straight forward to choose the most optimal computing architecture depending on different learning rules (supervised or unsupervised), as introduced in section 2.2.3. Thus, in the following sections, hardware implementation of LIF neuron by thermally coupled VO₂ oscillators, and large-scale SNN based on VO₂ LIF neurons will be studied and discussed.

A cross-section transmission electron microscopy (TEM) image of the VO₂ thin film sample on sapphire substrate is shown in **Fig 5.2a**. A schematic illustration of the LIF neuron realized by thermally coupled VO₂ oscillators is provided in **Fig 5.2b**. When the current is gradually increased across a VO₂ oscillator ($3 \times 3 \mu\text{m}^2$) the voltage starts to drop at ~ 1.2 mA, thereby showing negative differential resistance, as shown in **Fig 5.2c** inset down right. In the current

range between 2.5 mA and 4.9 mA, the voltage across the device oscillates with a frequency which increases with the magnitude of the current, as shown in **Fig 5.2c** middle. At higher current values (>5 mA) the device becomes fully metallic and no longer oscillates. When two VO_2 oscillators (each $3 \times 3 \mu\text{m}^2$) are closely spaced ($1.5 \mu\text{m}$), a very strong thermally coupled behavior can be observed. In **Fig 5.2d**, device 2 was set with a constant current $I_2 = 1.0$ mA, which is below the threshold current to oscillate (2.5 mA). By gradually increasing the current for device 1 (I_1 from 2.4 mA to 4.8 mA), device 2 can be thermally triggered to oscillate at the same frequency as device 1. **Fig 5.2d** shows synchronous waveforms at $I_1 = 2.4$ mA, $I_2 = 1.0$ mA (inset left), and $I_1 = 4.5$ mA, $I_2 = 1.0$ mA (inset right), respectively. The frequency of device 2 (f_2) and device 1 (f_1) can be synchronized from 7.5 kHz to 37.7 kHz, indicating a very strong thermal coupling between them. The current-driven self-sustained oscillation and thermal triggering effect between two oscillators has been discussed in the previous section **4.1**.

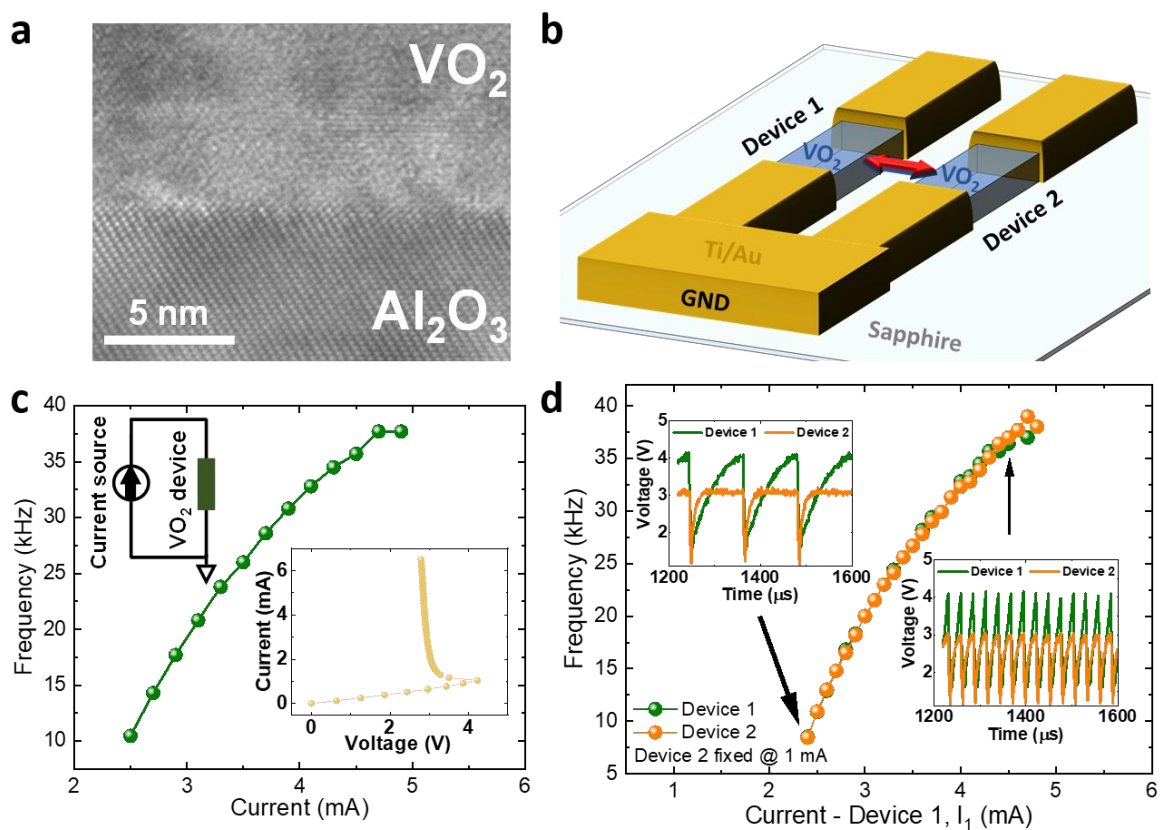


Fig 5.2. VO_2 leaky integrate-and-fire (LIF) neuron. **a**, TEM cross section image of a VO_2 device, provided by Zihan Yin. **b**, I - f curve of a single VO_2 device. The onset shows the I - V curve of the same device. **c**, Frequency locking of two VO_2 oscillators. Inset shows waveforms of two VO_2 devices which are thermally coupled.

Next, the LIF neuron functionalities from two thermally coupled VO_2 oscillators will be demonstrated. Device 2 (orange) is set at a constant current ($I_2 = -1.0$ mA) and acts as a trigger for output spikes. Device 1 (green) receives input spike currents and serves as the leaky

integrate-and-fire component. The input spike current to device 1 is defined by a ramp waveform: Offset at 1.93 mA, amplitude at 1.3 mA, frequency at 30 kHz, and duty cycle at 90%. **Fig 5.2a** to **Fig 5.2e** show the output response of the devices with increasing number of current spikes to device 1. When only one spike is sent (**Fig 5.2a**), the voltage of device 1 (V_1 , green curve) relaxes back to the offset level (3.3 V). Meanwhile, the voltage of device 2 (V_2 , orange curve) remains at its rest state. With increasing magnitude of the input spike V_1 gradually builds up and then the voltage relaxes back to the offset level when the incoming spikes are lifted, as shown in **Fig 5.2b** – which corresponds to “leaky integration” behavior. In **Fig 5.2c**, when V_1 reaches the threshold voltage (V_{th}) at 4.2 V after 6 input spikes, device 1 undergoes a phase transition to a low resistance state, thermally triggers device 2 to “fire” a spike (phase transition), and then device 1 slowly recovers back to its high resistance state. This long recovery time of device 1 can be taken as the “refractory period” of the LIF neuron. Interestingly, during the refractory period, it takes more input spikes (7 spikes) to integrate and trigger the second firing event, as shown in **Fig 5.2d** and **e**. By changing the amplitude or the offset level (or both) of the input spike current to device 1, the number of input spikes integrated by the VO₂ LIF neuron can be tuned, as summarized in **Fig 5.2f**. With larger amplitude (stronger stimuli), or higher offset level (more sensitive neuron), a smaller number of input spikes are needed for the VO₂ LIF neuron to integrate and fire.

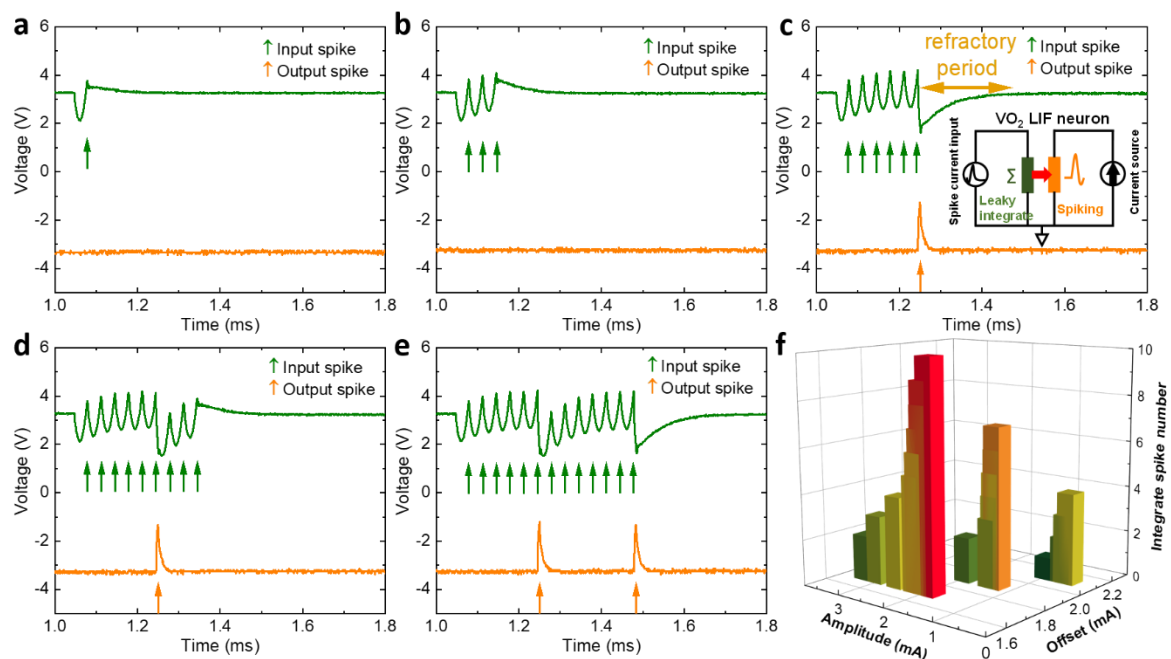


Fig 5.3. Operation and tunability of VO₂ leaky integrate-and-fire (LIF) neuron. VO₂ LIF neuron integrates (a) 1, (b) 3, (c) 6, (d) 9, and (e) 13 input spikes. f, Tunability (number of integrated spikes) of the VO₂ LIF neuron by different input spike amplitude and offset level.

Next, a temporal integration function realized by two VO₂ LIF neurons is demonstrated in **Fig 5.4**. An 8×10 μm² VO₂ spike generator (supplied with constant current at -0.74 mA) is used to integrate the spikes generated from two 4×6 μm² VO₂ LIF neuron at its left (2 μm spacing) and right (2 μm spacing) side, as shown in **Fig 5.4a** and **b**.

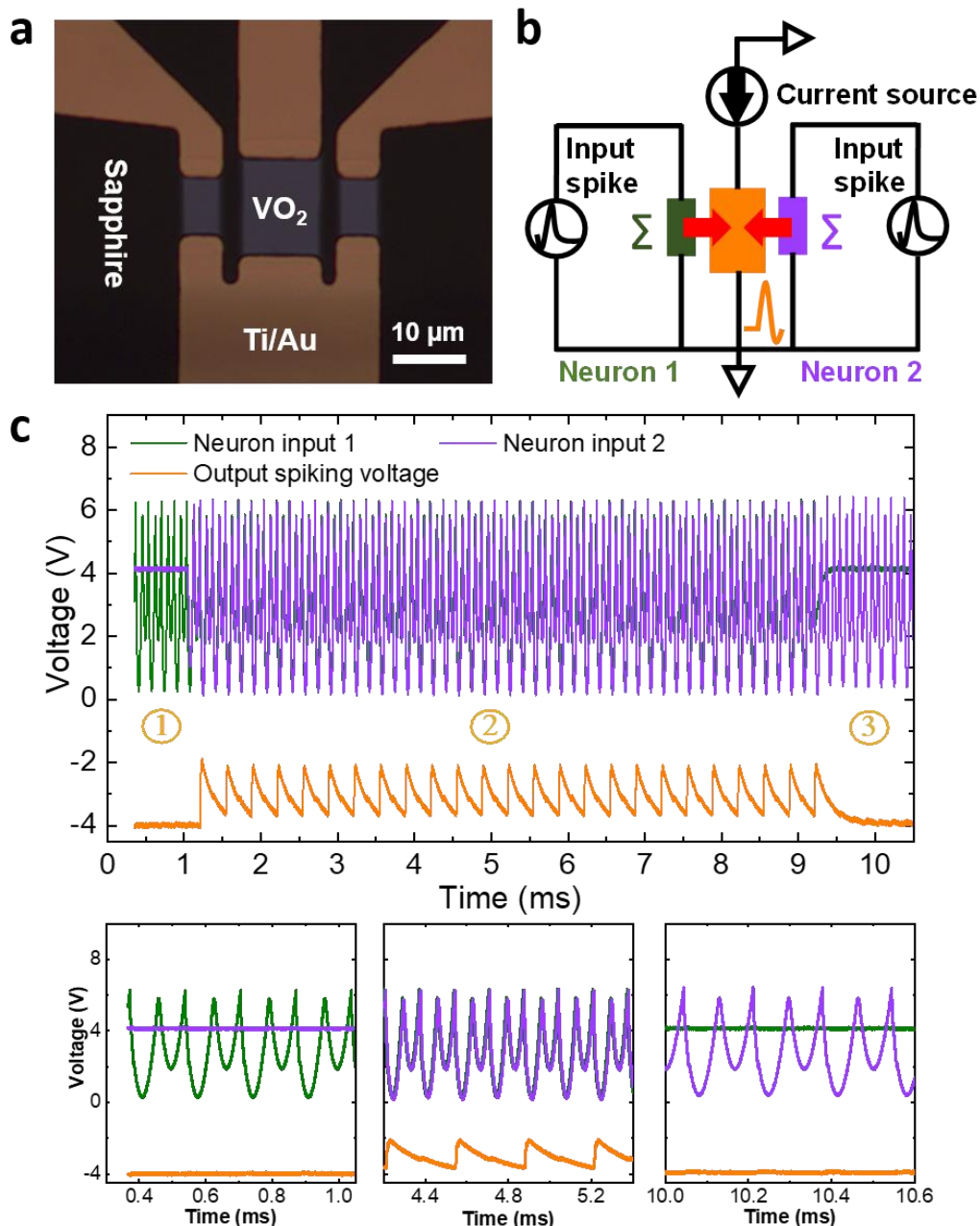


Fig 5.4. Temporal integration function realized by two VO₂ LIF neurons. a, Optical microscopy image of VO₂ LIF neurons. b, Schematic illustration of electrical connection. c, Post-LIF neuron output voltage (orange curve) integrates two pre-LIF neuron voltages (green and purple curves). Inset down left is sector 1, inset down middle is sector 2, inset down right is sector 3.

Both LIF neurons (green and purple curves) receive input spikes with the same frequency and amplitude (Ramp type, offset: 1.05 mA, amplitude: 4.0 mA, frequency: 12 kHz). Only when both LIF neurons are firing simultaneously (sector 2 in **Fig 5.4c**), the spike generator (orange curve) will be triggered to fire spikes. When only one LIF neuron is firing while the other one is at its rest state (sector 1 and 3 in **Fig 5.4c**), the spike generator will not be triggered to fire spikes.

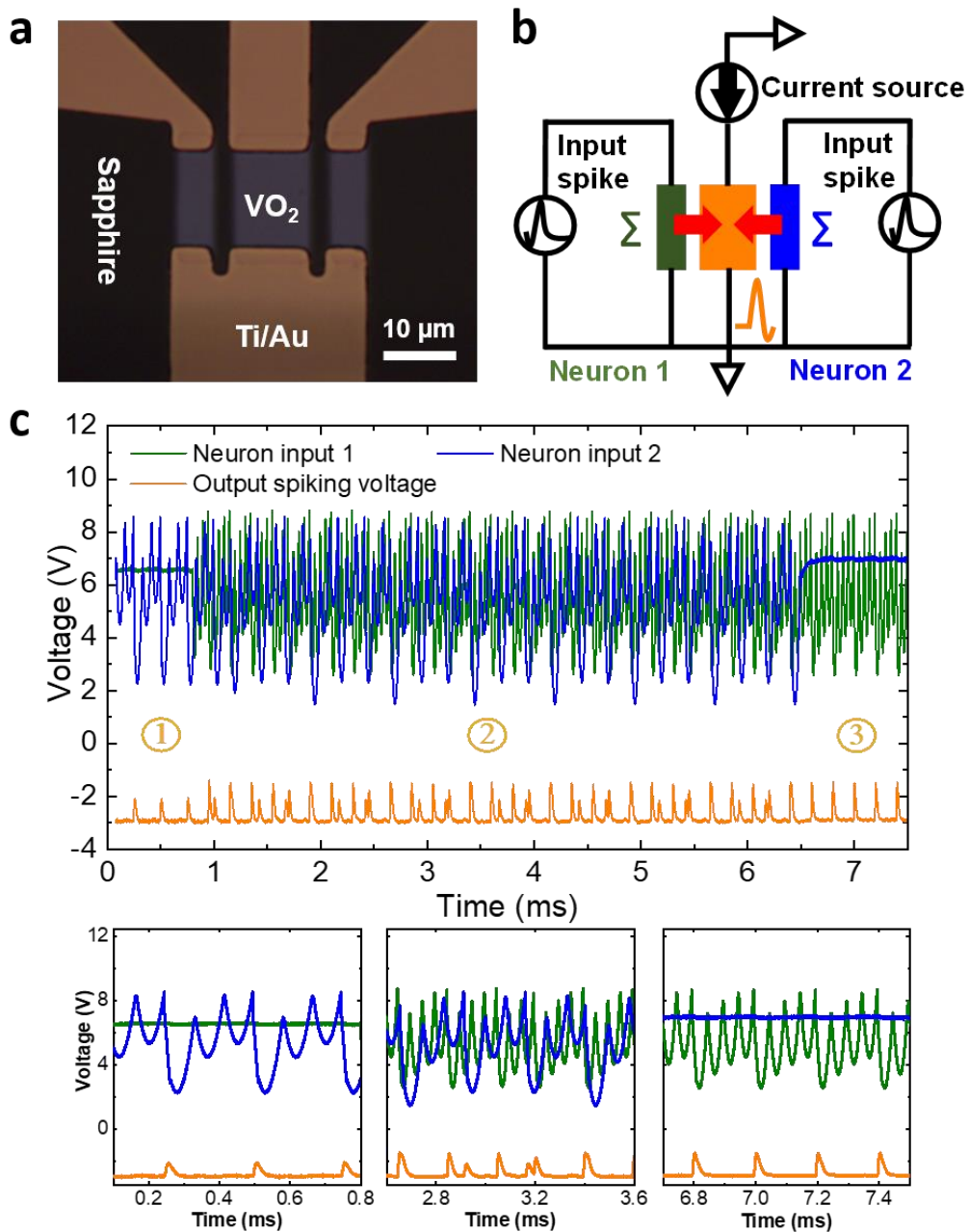


Fig 5.5. Temporal modulation function realized by two VO₂ LIF neurons. **a**, Optical microscopy image of VO₂ LIF neurons. **b**, Schematic illustration of electrical connection. **c**, Post-LIF neuron output voltage (orange line) modulates two pre-LIF neuron voltages (green and blue curves). Inset down left is sector 1, inset down middle is sector 2, inset down right is sector 3.

Next, a temporal modulation function is demonstrated in **Fig 5.5**. An $8 \times 10 \mu\text{m}^2$ VO₂ spike generator (set with a constant current at -0.5 mA) is used to integrate the spikes generated from two $4 \times 10 \mu\text{m}^2$ VO₂ LIF neuron at its left ($2 \mu\text{m}$ spacing) and right ($2 \mu\text{m}$ spacing) sides, as shown in **Fig 5.5a** and **b**. Two LIF neurons receive input spikes with different frequencies and amplitudes (Input to LIF neuron 1 (blue curve): Offset: 1.1 mA, amplitude: 6.7 mA, frequency: 20 kHz; Input to LIF neuron 2 (green curve): Offset: 1.2 mA, amplitude: 2.8 mA, frequency: 12 kHz. Both ramp type). Each LIF neuron can trigger the spike generator (orange curve) to spike at different frequencies and amplitudes, when the other one is at its rest state (sector 1 and 3 in **Fig 5.5c**). When both LIF neurons are firing at the same time (sector 2 in **Fig 5.5c**), the integrator will be triggered to fire spikes at a modulated frequency and amplitude.

5.3 Large-scale SNN based on VO₂ LIF Neurons

As introduced in section 2.2.3, spiking neural network (SNN) consists of leaky integrate-and-fire (LIF) neuron can use surrogate gradient-based supervised learning rule for training. In this section, the fitting for experimental data to extract two critical parameters for the LIF neuron: Leakage time constant and refractory period time constant, will be first carried out. Then, larger-scale SNN based on the extracted experimental data will be constructed by software program. Different network architectures, training parameters will be tested to evaluate the network performance on MNIST handwritten digits dataset.

The equivalent electric circuit of LIF neuron can be described in equation (2.2.2.2) for a resistor and capacitor connected in parallel. The neuron potential $U(t)$ (after the input is removed) during the relaxation process is fitted by the following equation:

$$U(t) = U_0 \cdot \exp\left(-\frac{t}{\tau_{leak}}\right) + U_{rest} \quad (5.3.1)$$

Where τ_{leak} is the leakage time constant, U_{rest} is the rest potential level, and U_0 is the neuron potential after input. **Fig 5.6** shows the fitting of experimentally measured potential of a VO₂ based LIF neuron after 3 input spikes. From the fitting, τ_{leak} is found to be 95 μs .

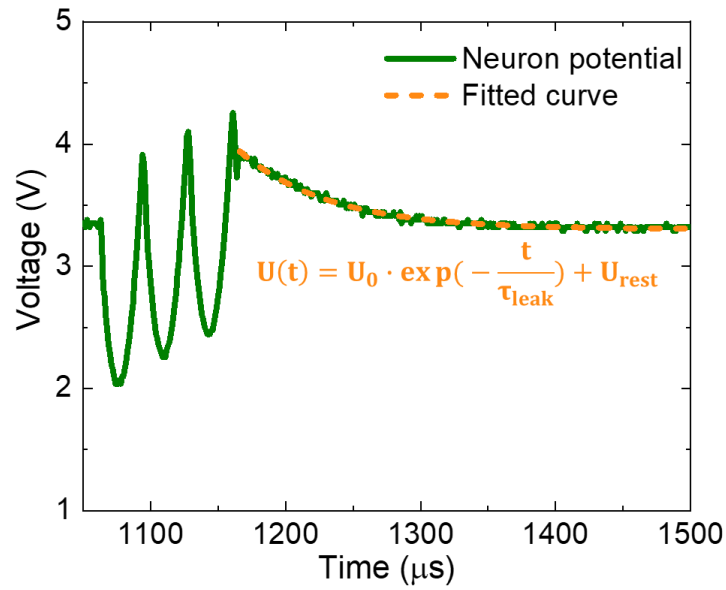


Fig 5.6. Experimental neuron potential and fitting of the relaxation process. Fitting of experimentally measured potential of a VO₂ based LIF neuron after 3 input spikes.

Fig 5.7 shows the measured potential of the LIF neuron after 6 input spikes. The neuron potential $U(t)$ during the refractory period is fitted by the following equation:

$$U(t) = U_{rest} - U_{reset} \cdot \exp\left(-\frac{t}{\tau_{ref}}\right) \quad (5.3.1)$$

Where τ_{ref} is the refractory period time constant, U_{rest} is the rest potential level, and U_{reset} is the reset constant after the neuron has fired. From the fitting, τ_{ref} is found to be 70 μ s.

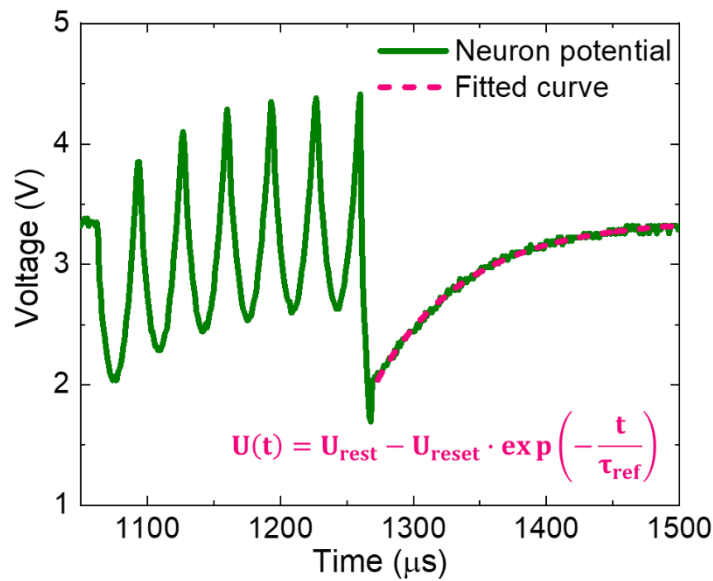


Fig 5.7. Experimental neuron potential and fitting of the refractory period. Fitting of experimentally measured potential of a VO₂ based LIF neuron after 7 input spikes.

The experimental data of the VO₂ LIF neuron are then used for constructing the one-layer large-scale SNN shown in **Fig 5.8a**. During the training process, every pixel (28×28 pixels) in the MNIST handwritten digit image was encoded into spike trains. The number of spikes in each spike train is proportional to the gray scale of the pixel (described by the Poisson distribution). After that, the spikes were injected into the LIF neuron layer through first synapse connection layer (simulated by the program). The output spikes from the LIF neuron layer then served as input and were injected into the output layer through the second synapse connection layer. The output layer consists of 10 output neurons, each of them was taught to recognized digit 0 to 9, respectively. Since the training process was governed by the supervised learning rule, each input digit already had a label indicating the desired output. As a result, during forward pass, where the data stream flowed from the input to output, the neurons in the output layer will give out different number of spikes depending on the input digit. Their output will then be compared with the target output, and the errors were then corrected during the backpropagation with surrogate gradient (introduced in section 2.2.3) through backward pass from the output layer to the first synapse connection layer, as shown in **Fig 5.8b**. After several training epoch, the system will reach the most optimal output that provide the minimum MSE (mean squared error).

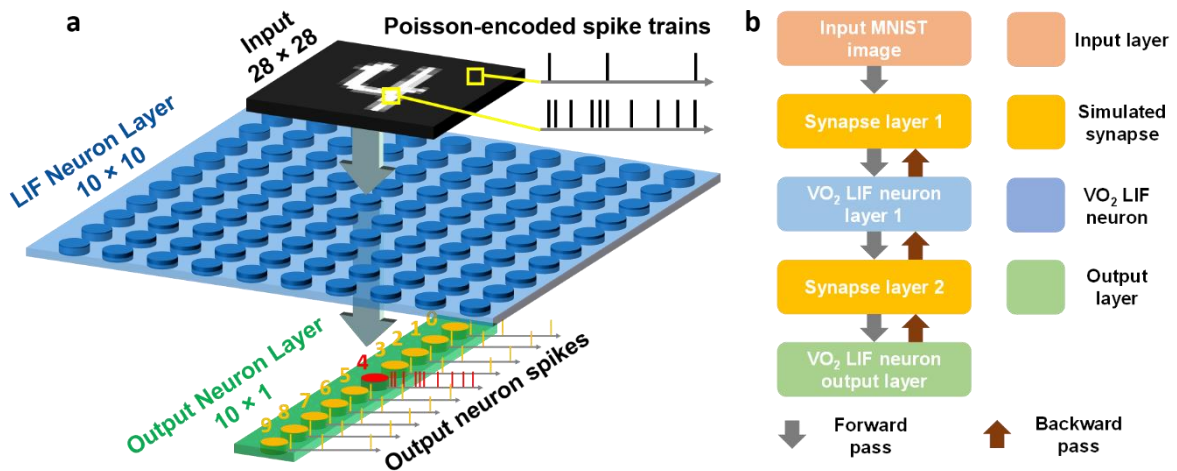


Fig 5.8. Large-scale spiking neural network based on VO₂ LIF neurons. a, Network architecture. **b**, Data flow in forward pass and backward pass during training.

As introduced in section 2.2.3, in order to reach global optimal solution, errors are described as loss function to be differentiated by every weight parameter. In this sense, one of the most critical training parameters is the learning rate α , which determines how large the update step (for a single parameter) is during training. It is defined as:

$$w_i := w_i - \alpha \frac{\partial}{\partial w_i} L(w_i) \quad (5.3.2)$$

Where w_i is the i^{th} weight parameter to be updated, $L(w_i)$ is the loss function that incorporates the parameter w_i defined in equation (2.2.3.9).

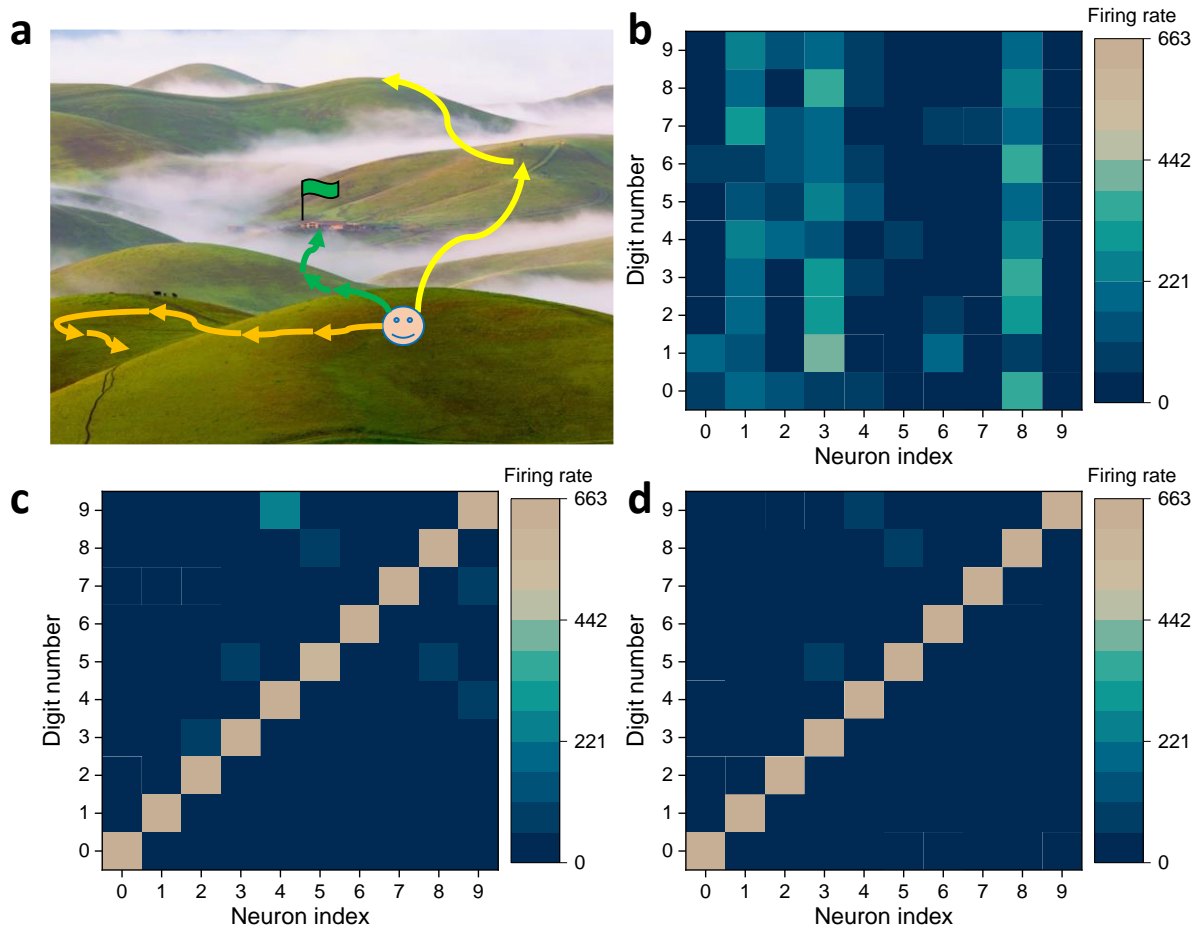


Fig 5.9. Tuning the learning parameter. **a**, Different conversion route in the minimizing the loss function set by different learning rates. **b**, Confusion matrix with a precision of 10%. **c**, Confusion matrix with a precision of 80%. **d**, Confusion matrix with a precision of 87%.

Imagine the loss function describes the system energy landscape, and the most optimal output is the global energy minimum point, shown as the village with green flag in **Fig 5.9a**. When the learning rate is set to be too large, the gradient decent might overshoot the minimum and fail to converge, or even diverge and end up at other high energy point, as shown in **Fig 5.9a** the yellow arrows. However, when the learning rate is set to be too small, the gradient decent could be too slow, or even be trapped in the local minimum surrounded by high gradients, causing it difficult to escape from them, as in **Fig 5.9a** the orange arrows. Only when the learning rate is set properly, the system can converge to the global energy minimum point, and provide the most optimal solution, as shown in **Fig 5.9a** the green arrows. **Fig 5.9b** to **Fig 5.9d** provide the results with different precision trained from different learning parameters. It is called the confusion matrix. “Neuron index” represents digit each neuron in the output layer is trained to learn, while the “Digit number” corresponds to the input digit needs to be recognize. In the most

optimal case, every neuron should fire with the highest firing rate when the input digit is the one it is supposed to recognize. **Fig 5.9b** shows the case when the learning rate was set to be too large, and the network only reached a precision of 10%. **Fig 5.9c** shows the case when the learning rate was set to be too small, and the network only reached a precision of 80%. **Fig 5.9b** shows the case when the learning rate was correctly set, and the network reached a precision of 87%. When the SNN is well trained, a clear diagonal line in the confusion matrix with small noise points should present.

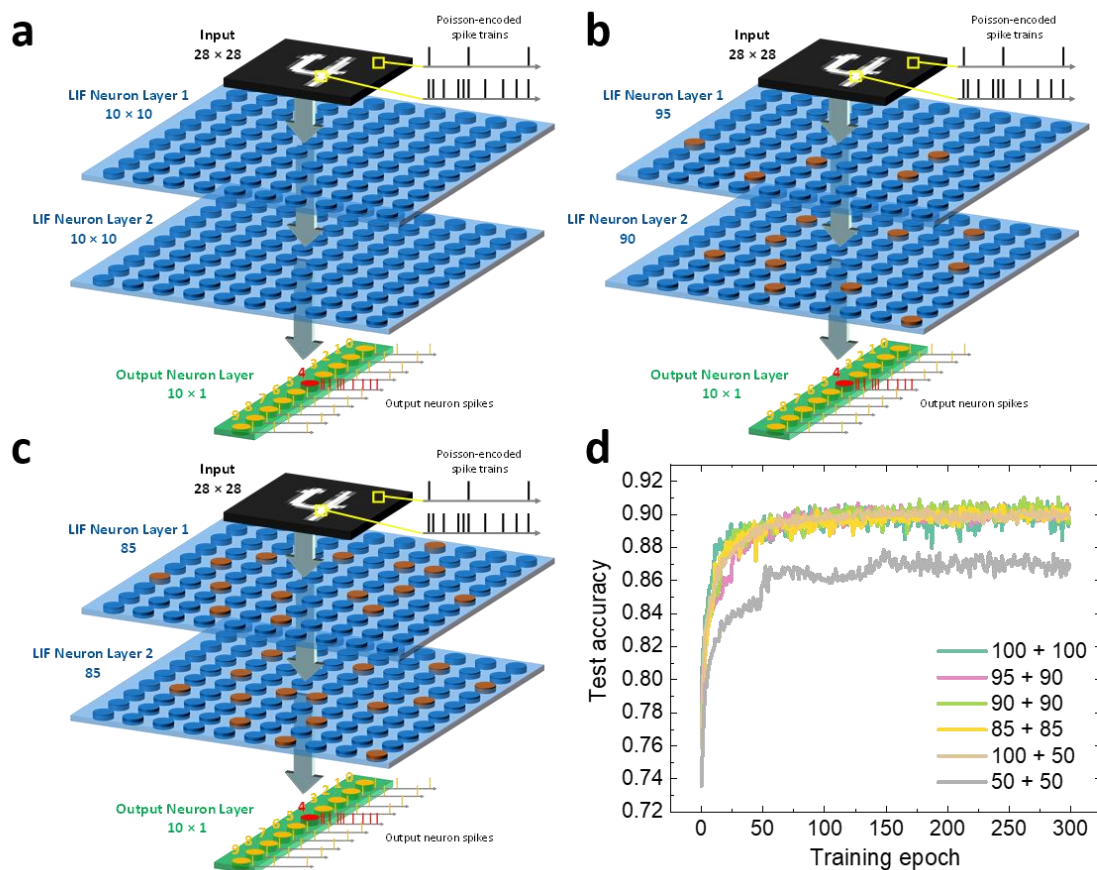


Fig 5.10. Training accuracy based on different percentage of defects. a, 2-layer spiking neural network architecture. **b**, 2-layer spiking neural network with 5% defect in the first layer and 10% defect in the second layer. **c**, 2-layer spiking neural network with 15% defect in the first layer and 15% defect in the second layer. **d**, Comparison of recognition precision of network with different numbers of defect points.

In order to improve the accuracy, one more layer of VO₂ LIF neurons was added to the network architecture, as shown in **Fig 5.10a**. Besides, in order to take device variability into account, i.e., defect devices that do not properly function: Different numbers of defect points (neuron is kept silent/removed) were introduced into both LIF neuron layers, as shown in **Fig 5.10b** and **c**. From the comparison of precision plotted in **Fig 5.10d**, it can be observed that, the system with up to 15% of defects in each LIF neuron layer can still maintain the performance of 90%

recognition accuracy, which has demonstrated good robustness against device variability. In order to have the least number of neurons with the least connection complexity, but with the same performance, the 2-layer architecture of SNN with 150 VO₂ LIF neuron was chosen, as shown in Fig 5.11.

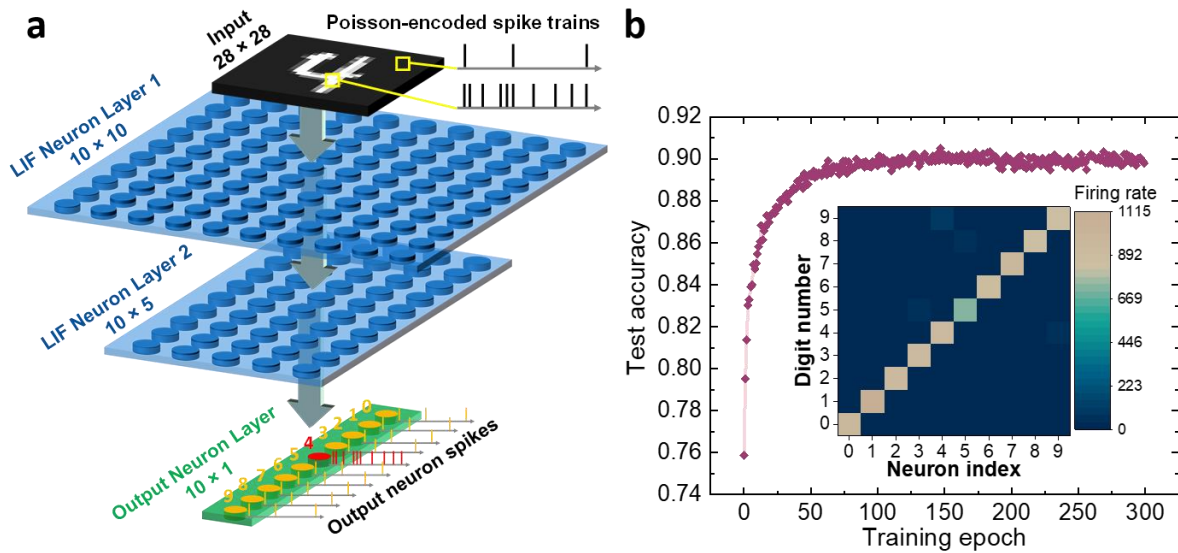


Fig 5.11. 2-layer SNN with 150 VO₂ LIF neuron. **a**, Schematic illustration of the spiking neural network with 150 VO₂ LIF neurons. **b**, Test accuracy (90%) and confusion matrix for MNIST digit recognition after 300 epochs of training.

Chapter 6 Conclusion and Outlook

This thesis provides an innovative approach for building energy-efficient oscillatory computational network. In the first part, the scalability of self-sustained VO₂ oscillators driven by a single constant current source have been experimentally demonstrated. VO₂ oscillators scaled with size down to 200 nm show substantially reduced energy consumption and higher operating frequency. A pair of thermally coupled VO₂ oscillators are used as computational elements – in which the exchange of thermal energy between oscillators increases the total energy efficiency. A tunable thermal coupling mechanism between two closely spaced VO₂ oscillators has been introduced in which any external electronic components are not required. By altering the excitation source (voltage or current) to the thermal cell placed between two VO₂ oscillators, the thermal coupling strength can be tuned and the range of synchronization frequency of the oscillators can be enlarged. Such synchronized oscillators with tunable thermal coupling were demonstrated for traditional Boolean-type computations as AND, NAND and NOR gates.

Conceptually, this thermally assisted frequency synchronization process can also be considered as the signal propagation in the neural system. The action potential that contains data is modulated in frequency (or amplitude, or both) and propagates from a pre-synaptic neuron to a post-synaptic neuron through a synapse [130, 131]. During this process, the action potential is transmitted through the synapse via releasing a neurotransmitter from the axon of the previous neuron to the dendrite of the next neuron [132]. One VO₂ oscillator (device 1) acts as a post-synaptic neuron while the other VO₂ oscillator (device 2) acts as pre-synaptic neuron, respectively. These two VO₂ neurons communicate via an oscillating potential, similar to the above-mentioned neurons in the biological system. Structurally, the thermal cell is equivalent to the synapse. The post-synaptic neuron is supplied with a constant low current and, thus, will only output a low frequency signal when it is not synchronized to the pre-synaptic neuron. Information is encoded in the domain above the threshold frequency where device 1 and device 2 desynchronize when synapse (thermal cell) is deactivated, and is fed into the presynaptic neuron as a continuously varying current (frequency-modulated). There is no synchronization between neurons in the frequency range where information is encoded. As a result, all information from the pre-synaptic neuron (device 2) is lost while propagating to the post-synaptic neuron, as shown in **Fig 6.1a**. When synapse (thermal cell) is activated, meaning that a neural link has been established and two VO₂ neurons are synchronized, the information can

be transmitted to the post-synaptic neuron, as shown in **Fig 6.1b**. Such a mechanism can also be applied for frequency modulated data transmission in an analog network for non-Boolean operations.

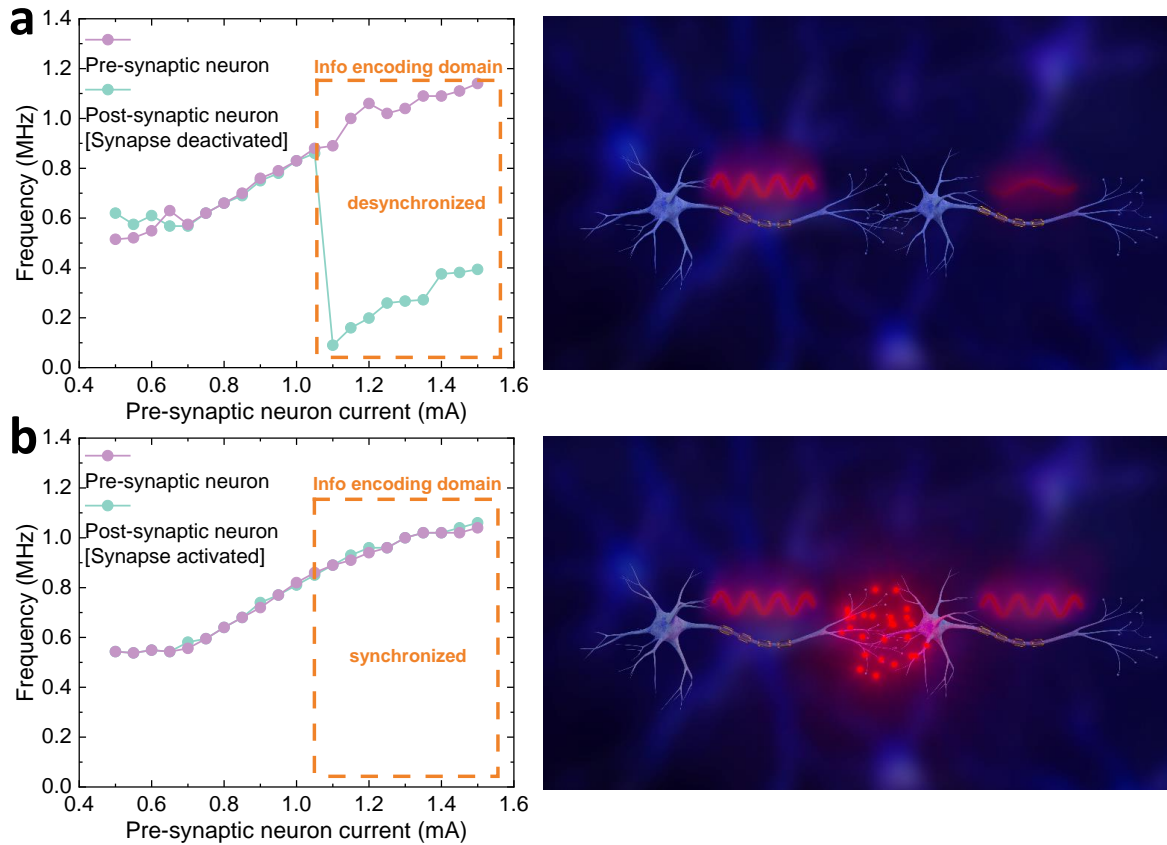


Fig 6.1. Frequency modulated information transmission in an oscillatory neural system.
a, Schematic illustration of the case when pre-synaptic neuron and post-synaptic neuron are desynchronized (synapse deactivated) at the frequency domain where information is encoded.
b, Schematic illustration of the case when pre-synaptic neuron and post-synaptic neuron are synchronized (synapse activated) at the frequency domain where information is encoded.

In the second part, cascade synchronization among three VO₂ cells have been demonstrated to realize the Hodgkin-Huxley (H-H) neuron model. By simply changing the current to one of the coupled VO₂ cells, which gives rise to the release of an oscillating thermal energy, five different firing modes including spiking and bursting can be generated from the coupled oscillators. Critical functionalities needed for a leaky integrate-and-fire (LIF) neuron including leaky integration, triggered spiking, and a refractory period is experimentally demonstrated by using thermally coupled VO₂ oscillators without any external electronic circuit components. In addition, the VO₂ LIF neuron shows good tunability for integrating different numbers of spikes. Simulation of a large-scale spiking neural network based on 150 VO₂ LIF neurons results in an accuracy of 90% for the recognition of hand-written digits. Furthermore, two complex functions: temporal integration and modulation can be directly realized by interacting VO₂ LIF neurons.

We believe that such a current-driven firing behavior and a tunable thermal triggering technique can be readily utilized for coding an artificial spiking neural network, in which the output spikes (numbers and firing time) depend on the intensity and spatiotemporal distribution of the input signal [133, 134]. Such a network of thermally coupled VO₂ oscillators with tunable interactions can also be highly useful for solving different types of computationally hard problems such as pattern classification and combinatorial problems [1, 135, 136].

The VO₂ oscillatory computational network developed in this thesis can be readily connected to non-volatile memories for storage of the output for further analysis. Magnetic memory with high storage density such as multi-bit racetracks [137] is a very promising candidate. Spikes generated from the VO₂ oscillatory computational network that incorporates with temporal information, can be directed injected into the racetrack memory, and later be traced and analyzed in the phase plane. Such computational system equipped with both short-term memory (VO₂ neuron) and long-term memory (memory; e.g., racetrack memory, memristor, etc.) can be further studied and developed to handle complex tasks that deal with temporally correlated data like natural language processing, time-series prediction and etc.

References

- [1] Romera, M., Talatchian, P., Tsunegi, S. et al. Vowel recognition with four coupled spin-torque nano-oscillators. *Nature* **563**, 230-234 (2018).
- [2] Raychowdhury, A., et al. Computing with Networks of Oscillatory Dynamical Systems. *Proc. IEEE* **107**, 73-89 (2019).
- [3] Yamazaki, K., Vo-Ho, V.-K., Bulsara, D., Le, N. Spiking Neural Networks and Their Applications: A Review. *Brain Sci.* **12**, 863 (2022).
- [4] Kim, R., Li, Y. and Sejnowski, T. J. Simple framework for constructing functional spiking recurrent neural networks. *PNAS* **116**, 45 (2019).
- [5] Yin, B., Corradi, F. and Bohté, S.M. Accurate and efficient time-domain classification with adaptive spiking recurrent neural networks. *Nat. Mach. Intell.* **3**, 905–913 (2021).
- [6] Maass, W. Networks of spiking neurons: The third generation of neural network models. *Neural Netw.* **10**, 1659–1671 (1997).
- [7] Asmara, T., Wan, D., Zhao, Y. et al. Tunable and low-loss correlated plasmons in Mott-like insulating oxides. *Nat. Commun.* **8**, 15271 (2017).
- [8] Gao, L., Chen, P. and Yu, S. NbO_x based oscillation neuron for neuromorphic computing. *Appl. Phys. Lett.* **4**, 103503 (2017).
- [9] McGee, R. et al. Sharpness and intensity modulation of the metal-insulator transition in ultrathin VO₂ films by interfacial structure manipulation. *Phys. Rev. Mat.* **2**, 034605 (2018).
- [10] Yang, T. et al. On growth of epitaxial vanadium oxide thin film on sapphire (0001). *J. Mater. Res.* **25**, 422–426 (2010).
- [11] Hattori, A. N. et al. Investigation of Statistical Metal-Insulator Transition Properties of Electronic Domains in Spatially Confined VO₂ Nanostructure. *Crystals* **10**, 631 (2020).
- [12] Jeong, J. et al. Suppression of Metal-Insulator Transition in VO₂ by Electric Field-Induced Oxygen Vacancy Formation. *Science* **339**, 1402-1405 (2013).
- [13] Yi, W. et al. Biological plausibility and stochasticity in scalable VO₂ active memristor neurons. *Nat. Commun.* **9**, 4661 (2018).
- [14] Corti, E. et al. Coupled VO₂ Oscillators Circuit as Analog First Layer Filter in Convolutional Neural Networks. *Front. Neurosci.* **15**, 628254 (2021).
- [15] Yuan, R., Duan, Q., Tiw, P.J. et al. A calibratable sensory neuron based on epitaxial VO₂ for spike-based neuromorphic multisensory system. *Nat. Commun.* **13**, 3973 (2022).
- [16] Núñez, J. et al. Oscillatory Neural Networks Using VO₂ Based Phase Encoded Logic. *Front. Neurosci.* **15**, 655823 (2021).
- [17] Lee, Y. et al. Metal-insulator transition-induced electrical oscillation in vanadium dioxide thin film. *Appl. Phys. Lett.* **92**, 162903 (2008).
- [18] Velichko, A., Belyaev, M., Putrolaynen, V., Perminov, V. and Pergament, A. Thermal coupling and effect of subharmonic synchronization in a system of two VO₂ based oscillators. *Solid-State Electron.* **141**, 40-49 (2018).

- [19] Qiu, E., Zhang, Y.-H., Ventra, M. D., Schuller, I. K. Reconfigurable Cascaded Thermal Neuristors for Neuromorphic Computing. *Adv. Mater.* **36**, 2306818 (2024).
- [20] Hebb, D. *The Organization of Behavior: A Neuropsychological Theory*. Wiley, 1949.
- [21] Hanslmayr S, Staeresina BP, Jensen O. Oscillatory brain mechanisms for memory formation: Online and offline processes. In: Kahana MJ, Wagner AD, eds. *The Oxford Handbook of Human Memory, Two Volume Pack: Foundations and Applications*. Oxford University Press, 711-739 (2024).
- [22] Buzsáki G, Wang XJ. Mechanisms of gamma oscillations. *Annu Rev Neurosci.* **35**, 203-225 (2012).
- [23] Buzsáki G, Draguhn A. Neuronal oscillations in cortical networks. *Science.* **304**, 1926-1929 (2004).
- [24] von Neumann, J. Non-linear capacitance or inductance switching, amplifying, and memory organs, *U.S. Patent* **2**, 815, 488 (1957).
- [25] Wigington, R. L. A new concept in computing. *Proc. IRE* **47**, 516–523 (1959).
- [26] Csaba, G., Porod, W. Coupled oscillators for computing: A review and perspective. *Appl. Phys. Rev.* **7**, 011302 (2020).
- [27] Hopfield, J. J. Neural networks and physical systems with emergent collective computational abilities. *Proc. Natl. Acad. Sci. U. S. A.* **79(8)**, 2554–2558 (1982).
- [28] Hoppensteadt, F. C. and Izhikevich, E. M. Oscillatory neurocomputers with dynamic connectivity. *Phys. Rev. Lett.* **82**, 2983 (1999).
- [29] Yu, Q., Tang, H., Hu, J., and Tan, K. C. Temporal learning in multilayer spiking neural networks through construction of causal connections. *Neuromorphic Cognitive Systems*, 115-129, Springer (2017).
- [30] Michel, A. N., Farrell, J. A. and Porod, W. Qualitative analysis of neural networks. *IEEE Trans. Circuits Syst.* **36**, 229–243 (1989).
- [31] Strogatz, S. H. From Kuramoto to Crawford: Exploring the onset of synchronization in populations of coupled oscillators. *Physica D* **143**, 1–20 (2000).
- [32] Acebrn, J. A., Bonilla, L. L., Vicente, C. J. P., Ritort, F. and Spigler, R. The Kuramoto model: A simple paradigm for synchronization phenomena. *Rev. Mod. Phys.* **77**, 137 (2005).
- [33] Checiu, D., Mathias, B. & Radwa, K. Reconstructing creative thoughts: Hopfield neural networks. *Neurocomputing* **575**, 127324 (2024).
- [34] Tanaka, G., Yamane, T., et. al. Recent advances in physical reservoir computing: A review. *Neural Networks* **115**, 100-123 (2019).
- [35] Dion, G., Mejaouri, S. and Sylvestre, J. Reservoir computing with a single delay-coupled non-linear mechanical oscillator. *J. Appl. Phys.* **124**, 152132 (2018).
- [36] Goto, E. The parametron, a digital computing element which utilizes parametric oscillation. *Proc. IRE* **47**, 1304–1316 (1959).
- [37] Gardner, D. S., Schrom, G., Paillet, F., Jamieson, B., Karnik, T. and Borkar, S. Review of on-chip inductor structures with magnetic films. *IEEE Trans. Magn.* **45**, 4760–4766 (2009).
- [38] Zhang, P. Design of CMOS LC Oscillators, *IEEE ICSICT* **8**, 1534-1537 (2006).

- [39] Farzeen, S., Ren, G. and Chen, C. An ultra-low power ring oscillator for passive UHF RFID transponders. *IEEE MWSCAS* **53**, 558–561 (2010).
- [40] Sahoo, B. D. Ring oscillator based sub-1V leaky integrate-and-fire neuron circuit. *IEEE ISCAS*, 1–4 (2017).
- [41] Feuer, M. D., Hendel, R. H., et. al. High-speed low-voltage ring oscillators based on selectively doped heterojunction transistors. *IEEE Electron Device Lett.* **4**, 306–307 (1983).
- [42] Landau, L. and Lifshitz, E. On the theory of the dispersion of magnetic permeability in ferromagnetic bodies. *Phys. Z. Sowjetunion* **8**, 153–169, 1935.
- [43] Gilbert, T. L. A Lagrangian formulation of the gyromagnetic equation of the magnetization field. *Phys. Rev.* **100**, 1243 (1955).
- [44] Slonczewski, J. Current-driven excitation of magnetic multilayers. *J. Magn. Magn. Mater.* **159**, 1–7 (1996).
- [45] Torrejon, J., Riou, M., Araujo, F. *et al.* Neuromorphic computing with nanoscale spintronic oscillators. *Nature* **547**, 428–431 (2017).
- [46] Kaka, S., Pufall, M., Rippard, W. *et al.* Mutual phase-locking of microwave spin torque nano-oscillators. *Nature* **437**, 389–392 (2005).
- [47] Lebrun, R., Tsunegi, S., Bortolotti, P. *et al.* Mutual synchronization of spin torque nano-oscillators through a long-range and tunable electrical coupling scheme. *Nat Commun* **8**, 15825 (2017).
- [48] Slonczewski, J. C. Excitation of spin waves by an electric current. *J. Magn. Magn. Mater.* **195**, L261–L268 (1999).
- [49] CMOS with a spin. *Nat Electron* **2**, 263 (2019).
- [50] Locatelli, N., Cros, V. & Grollier, J. Spin-torque building blocks. *Nature Mater* **13**, 11–20 (2014).
- [51] Qingjiang, L., Khiat, A., Salaoru, I. *et al.* Memory Impedance in TiO₂ based Metal-Insulator-Metal Devices. *Sci Rep* **4**, 4522 (2014).
- [52] Mercy, A., Bieder, J., Íñiguez, J. *et al.* Structurally triggered metal-insulator transition in rare-earth nickelates. *Nat Commun* **8**, 1677 (2017).
- [53] Riccò, S., Kim, M., Tamai, A. *et al.* In situ strain tuning of the metal-insulator-transition of Ca₂RuO₄ in angle-resolved photoemission experiments. *Nat Commun* **9**, 4535 (2018).
- [54] Andrews, J. L., Santos, D. A., Meyyappan, M., Williams, R. S. & Banerjee, S. Building brain-inspired logic circuits from dynamically switchable transition metal oxides. *Trends Chem.* **1**, 711–726 (2019).
- [55] A. Parihar, N. Shukla, S. Datta, and A. Raychowdhury, “Exploiting synchronization properties of correlated electron devices in a non-boolean computing fabric for template matching,” *IEEE J. Emerging Sel. Top. Circuits Syst.* **4**, 450–459 (2014).
- [56] Leroy, J., Crunteanu, A., Givernaud, J., Orlianges, J., Champeaux, C., and Blondy, P. Generation of electrical self-oscillations in two-terminal switching devices based on the insulator-to-metal phase transition of VO₂ thin films. *Int. J. Microw. Wirel. Technol.* **4**, 101–107 (2011).

- [57] Li, D. et al. Joule Heating-Induced Metal–Insulator Transition in Epitaxial VO₂/TiO₂ Devices. *ACS Appl. Mater. Interfaces*. **8**, 12908–12914 (2016).
- [58] Zimmers, A., et al. Role of thermal heating on the voltage induced insulator-metal transition in VO₂. *Phys. Rev. Lett.* **110**, 056601 (2013).
- [59] Kumar, S., Pickett, M. D., Strachan, J. P., Gibson, G., Nishi, Y. and Williams, R. S. Local temperature redistribution and structural transition during joule-heating-driven conductance switching in VO₂. *Adv. Mater.* **25**, 6128–6132 (2013).
- [60] Jessadaluk, S. et al. A tunable thermal switching device based on Joule heating-induced metal–insulator transition in VO₂ thin films via an external electric field. *Japn. J. Appl. Phys.* **58**, SDDE12 (2019).
- [61] Kumar, S. et al. Local temperature redistribution and structural transition during Joule-Heating-driven conductance switching in VO₂. *Adv. Mater.* **25**, 6128–6132 (2013).
- [62] Horrocks, G. A., Singh, S., Likely, M. F., Sambandamurthy, G. and Banerjee, S. Scalable Hydrothermal Synthesis of Free-Standing VO₂ Nanowires in the M1 Phase. *CS Appl. Mater. Interfaces*. **6**, 15726–15732 (2014).
- [63] Wu, C. et al. Direct hydrothermal synthesis of monoclinic VO₂ (M) single-domain nanorods on large scale displaying magnetocaloric effect. *J. Mater. Chem.* **21**, 4509 (2011).
- [64] Chen, Y. et al. Avalanche breakdown and self-stabilization effects in electrically driven transition of carbon nanotube covered VO₂ film. *J. Phys. D: Appl. Phys.* **50**, 255101 (2017).
- [65] Parihar, A., Shukla, N., Datta, S. and Raychowdhury, A. Exploiting synchronization properties of correlated electron devices in a non-boolean computing fabric for template matching. *IEEE J. Emerging Sel. Top. Circuits Syst.* **4**, 450–459 (2014).
- [66] Maher, O., Jiménez, M., Delacour, C. et al. A CMOS-compatible oscillation-based VO₂ Ising machine solver. *Nat Commun* **15**, 3334 (2024).
- [67] Maher, O., Bernini, R., Harnack, N. et al. Highly reproducible and CMOS-compatible VO₂-based oscillators for brain-inspired computing. *Sci Rep* **14**, 11600 (2024).
- [68] Petranikova, M. et al. Vanadium sustainability in the context of innovative recycling and sourcing development. *Waste Manag.* **113**, 521–544 (2020).
- [69] McCulloch, W. S., & Pitts, W. A logical calculus of the ideas immanent in nervous activity. *Bull. Math. Biol.* **5**, 115–133 (1943).
- [70] Rosenblatt, F. The perceptron: A probabilistic model for information storage and organization in the brain. *Psychol. Rev.* **65**, 386–408 (1958).
- [71] Minsky, M., & Papert, S. Perceptrons. *MIT Press* (1969).
- [72] Rummelhart, D. E. Learning representations by back-propagating errors. *Nature* **323**, 533–536 (1986).
- [73] Chauvin, Y., & Rumelhart, D. E. *Backpropagation: Theory, architectures, and applications*. Psychology Press (1995).
- [74] Lillicrap, T.P., Santoro, A., Marris, L. et al. Backpropagation and the brain. *Nat Rev Neurosci* **21**, 335–346 (2020).

- [75] Hodgkin, AL., Huxley, AF. Currents carried by sodium and potassium ions through the membrane of the giant axon of *Loligo*. *J. Physiol* **116**, 449–472 (1952).
- [76] Hodgkin, AL., Huxley, AF. The components of membrane conductance in the giant axon of *Loligo*. *J. Physiol* **116**, 473–496 (1952).
- [77] Hodgkin, AL., Huxley, AF. The dual effect of membrane potential on sodium conductance in the giant axon of *Loligo*. *J. Physiol* **116**, 497–506 (1952).
- [78] Hodgkin, AL., Huxley, AF. A quantitative description of membrane current and its application to conduction and excitation in nerve. *J. Physiol* **117**, 500–544 (1952).
- [79] Catterall, WA., et al. The Hodgkin-Huxley Heritage: From Channels to Circuits. *J Neurosci.* **10**, 14064-73 (2012).
- [80] Schultheiss, NW., Prinz, AA., Butera, RJ. Phase response curves in neuroscience. New York: Springer (2012).
- [81] Gouwens, NW., Zeberg, H., et al. Synchronization of firing in cortical fast-spiking interneurons at gamma frequencies: a phase-resetting analysis. *PLoS Comput Biol.* **6**, 9 (2010).
- [82] Ermentrout, B. Type I membranes, phase resetting curves, and synchrony. *Neural Comp.* **8**, 979–1001 (1996)
- [83] Abouzeid, A., Ermentrout, B. Type-II phase resetting curve is optimal for stochastic synchrony. *Phys Rev E* **80**, 011911 (2009).
- [84] Burkitt, A.N. A Review of the Integrate-and-fire Neuron Model: I. Homogeneous Synaptic Input. *Biol Cybern* **95**, 1–19 (2006).
- [85] Kistler, W. M., Gerstner, W. & van Hemmen, J. L. Reduction of the Hodgkin-Huxley equations to a single-variable threshold model. *Neural computation* **9**, 1015–1045 (1997).
- [86] Lapique, L. Recherches quantitatives sur l’excitation électrique des nerfs traitée comme une polarisation. *J Physiol Pathol Gen* **9**, 620–635 (1907).
- [87] Meffin, H., Burkitt, AN., Grayden, DB. An analytical model for the ‘large, fluctuating conductance state’ typical of neocortical neurons in vivo. *J Comput Neurosci* **16**, 159–175 (2004).
- [88] Diehl, P. U. & Cook, M. Unsupervised learning of digit recognition using spike-timing-dependent plasticity. *Front. Comput. Neurosci.* **9**, 99 (2015).
- [89] Deng, L. The MNIST Database of Handwritten Digit Images for Machine Learning Research [Best of the Web], *IEEE Signal Process. Mag.* **29**, 141-142 (2012).
- [90] Andrade-Talavera, Y., Fisahn, A. & Rodríguez-Moreno, A. Timing to be precise? An overview of spike timing-dependent plasticity, brain rhythmicity, and glial cells interplay within neuronal circuits. *Mol Psychiatry* **28**, 2177–2188 (2023).
- [91] Morrison, A., Aertsen, A., and Diesmann, M. (2007). Spike-timing-dependent plasticity in balanced random networks. *Neural Comput.* **19**, 1437–1467.
- [92] Zhang, W., and Linden, D. J. (2003). The other side of the engram: experience-driven changes in neuronal intrinsic excitability. *Nat. Rev. Neurosci.* **4**, 885–900.

- [93] Querlioz, D., Bichler, O., Dollfus, P., and Gamrat, C. Immunity to device variations in a spiking neural network with memristive nanodevices. *Nanotechnol. IEEE Trans.* **12**, 288–295 (2013).
- [94] Eshraghian, J. K., et al. Training Spiking Neural Networks Using Lessons From Deep Learning. *Proc of the IEEE* **111**, 1016–1054 (2023).
- [95] Pérez-Carrasco, J. A., et al. Mapping from frame-driven to frame-free event-driven vision systems by low-rate rate coding and coincidence processing-application to feedforward ConvNets. *IEEE Trans. Pattern Anal. Mach. Intell* **35**, 2706–2719 (2013).
- [96] Töckl, C., Maass, W. Optimized spiking neurons can classify images with high accuracy through temporal coding with two spikes. *Nat Mach Intell* **3**, 230–238 (2021).
- [97] Bohte, S. M., Kok, J. N. and Poutré, H. L. Error-backpropagation in temporally encoded networks of spiking neurons. *Neurocomputing* **48**, 17–37 (2002).
- [98] Comsa, I. M., Potempa, K., Versari, L., et al. Temporal coding in spiking neural networks with alpha synaptic function. *Proc. IEEE Int. Conf. Acoust., Speech Signal Process. (ICASSP)*, May 2020.
- [99] Shrestha, S. B. and Orchard, G. SLAYER: Spike layer error reassignment in time. *Proc. 32nd Int. Conf. Neural Inf. Process. Syst.*, 1419–1428 (2018).
- [100] Esser, S. K., et al. Convolutional networks for fast, energy-efficient neuromorphic computing. *Proc. Nat. Acad. Sci. USA* **113**, 11441–11446 (2016).
- [101] Kim, DH and Kwok, HS. Pulsed laser deposition of VO₂ thin films. *Appl. Phys. Lett.* **19**, 3188–3190 (1994).
- [102] Borek, M., Qian, F., Nagabushnam, V., Singh, R. K. Pulsed laser deposition of oriented VO₂ thin films on R-cut sapphire substrates. *Appl. Phys. Lett.* **13**, 3288–3290 (1993).
- [103] Shepelin, NA. A practical guide to pulsed laser deposition. *Chem. Soc. Rev.* **52**, 2294 (2023).
- [104] Muraoka, Y., Hiroi, Z. Metal–insulator transition of thin films grown on (001) and (110) substrates. *Appl. Phys. Lett.* **28**, 583–585 (2002).
- [105] Martens, K, et al. Improved metal-insulator-transition characteristics of ultrathin VO₂ epitaxial films by optimized surface preparation of rutile TiO₂ substrates. *Appl. Phys. Lett.* **24** 081918 (2014).
- [106] Yang, Y., Mao, X. Thickness effects on the epitaxial strain states and phase transformations in (001)-VO₂/TiO₂ thin films. *J. Appl. Phys.* **28**, 082508 (2019).
- [107] Garry, G., Durand, O. and Lordereau, A. Structural, electrical and optical properties of pulsed laser deposited VO₂ thin films on R-and C-sapphire planes. *Thin Solid Films.* **453**, 427 (2004).
- [108] Jian, J. et al. Continuous tuning of phase transition temperature in VO₂ thin films on c-cut sapphire substrates via strain variation. *ACS Appl. Mater. Interfaces* **9**, 5319–5327 (2017).
- [109] Geehan, G., Ritika, R., Winchester, C. Impact of nanofluids and specific frequency absorbers in parabolic trough collector solar furnaces. *PAM Review: Energy Sci Technol* **5**, 89–103 (2018).

- [110] Shao, Z., Cao, X., Luo, H. *et al.* Recent progress in the phase-transition mechanism and modulation of vanadium dioxide materials. *NPG Asia Mater* **10**, 581–605 (2018).
- [111] Schwingenschlögl, U. & Eyert, V. The vanadium Magnéli phases VnO_{2n-1} . *Ann. Phys.* **13**, 475–510 (2004).
- [112] Kasirga, T. S. *et al.* Photoresponse of a strongly correlated material determined by scanning photocurrent microscopy. *Nat. Nanotechnol.* **7**, 723–727 (2012).
- [113] Liu, K. *et al.* Giant-amplitude, high-work density microactuators with phase transition activated nanolayer bimorphs. *Nano Lett.* **12**, 6302–6308 (2012).
- [114] Bae, S. H. *et al.* The memristive properties of a single VO_2 nanowire with switching controlled by self-heating. *Adv. Mater.* **25**, 5098–5103 (2013).
- [115] Hu, B. *et al.* External-strain induced insulating phase transition in VO_2 nanobeam and its application as flexible strain sensor. *Adv. Mater.* **22**, 5134–5139 (2010).
- [116] Savo, S. *et al.* Reconfigurable anisotropy and functional transformations with VO_2 -based metamaterial electric circuits. *Phys. Rev. B* **91**, 134105 (2015).
- [117] Kats, M. A. *et al.* Vanadium dioxide as a natural disordered metamaterial: perfect thermal emission and large broadband negative differential thermal emittance. *Phys. Rev. X* **3**, 041004 (2013).
- [118] Wu, Y., Fan, L., Liu, Q. *et al.* Decoupling the Lattice Distortion and Charge Doping Effects on the Phase Transition Behavior of VO_2 by Titanium (Ti^{4+}) Doping. *Sci Rep* **5**, 9328 (2015).
- [119] Xu, C., Jin, C., Chen, Z. *et al.* Transient dynamics of the phase transition in VO_2 revealed by mega-electron-volt ultrafast electron diffraction. *Nat Commun* **14**, 1265 (2023).
- [120] Analytical Techniques in the Pharmaceutical Sciences.
- [121] Li, G., Wang, Z., Chen, Y. *et al.* Computational elements based on coupled VO_2 oscillators via tunable thermal triggering. *Nat Commun* **15**, 5820 (2024).
- [122] K. Inaba: The Rigaku Journal, 26(2) (2010).
- [123] Hattori, A. N. *et al.* Investigation of Statistical Metal-Insulator Transition Properties of Electronic Domains in Spatially Confined VO_2 Nanostructure. *Crystals*. **10(8)**, 631 (2020).
- [124] Indiveri, G. *et al.* Neuromorphic silicon neuron circuits. *Front. Neurosci.* **5**, 73 (2011).
- [125] Izhikevich, E. M. Which model to use for cortical spiking neurons. *IEEE Trans. Neur. Netw.* **15**, 1063-1070 (2004).
- [126] Weyand, T. G., Boudreaux, M. and Guido, W. Burst and tonic response modes in thalamic neurons during sleep and wakefulness. *J. Neurophysiol.* **85**, 1107–1118 (2001).
- [127] Gibson, J. R., Beierlein, M. and Connors, B. W. Two networks of electrically coupled inhibitory neurons in neocortex. *Nature* **402**, 75 (1999).
- [128] Gray, C. M. and McCormick, D. A. Chattering cells: superficial pyramidal neurons contributing to the generation of synchronous oscillations in the visual cortex. *Science* **274**, 109-113 (1996).

- [129] Yang, Y., Zhu, F., Zhang, X. *et al.* Firing feature-driven neural circuits with scalable memristive neurons for robotic obstacle avoidance. *Nat Commun* **15**, 4318 (2024).
- [130] Wyffels, F., Li, J., Waegeman, T. *et al.* Frequency modulation of large oscillatory neural networks. *Biol. Cybern.* **108**, 145–157 (2014).
- [131] Soman, K., Muralidharan, V. and Chakravarthy, V. S. An Oscillatory Neural Autoencoder Based on Frequency Modulation and Multiplexing. *Front. Comput. Neurosci.* **12**, 00052 (2018).
- [132] Faber, D. S. and Pereda, A. E. Two Forms of Electrical Transmission Between Neurons. *Front. Mol. Neurosci.* **11**, 00427 (2018).
- [133] Shaban, A., Bezugam, S.S. and Suri, M. An adaptive threshold neuron for recurrent spiking neural networks with nanodevice hardware implementation. *Nat. Commun.* **12**, 4234 (2021).
- [134] Yin, B., Corradi, F. and Bohté, S.M. Accurate and efficient time-domain classification with adaptive spiking recurrent neural networks. *Nat. Mach. Intell.* **3**, 905–913 (2021).
- [135] Mallick, A., Bashar, M.K., Truesdell, D.S. *et al.* Using synchronized oscillators to compute the maximum independent set. *Nat. Commun.* **11**, 4689 (2020).
- [136] Parrilla-Gutierrez, J.M., Sharma, A., Tsuda, S. *et al.* A programmable chemical computer with memory and pattern recognition. *Nat. Commun.* **11**, 1442 (2020).
- [137] Jeon, J.C., *et al.* Multicore memristor from electrically readable nanoscopic racetracks. *Science* **386**, 315–322 (2024).

Appendix

Electrical transport measurements of VO₂ 2.5D array

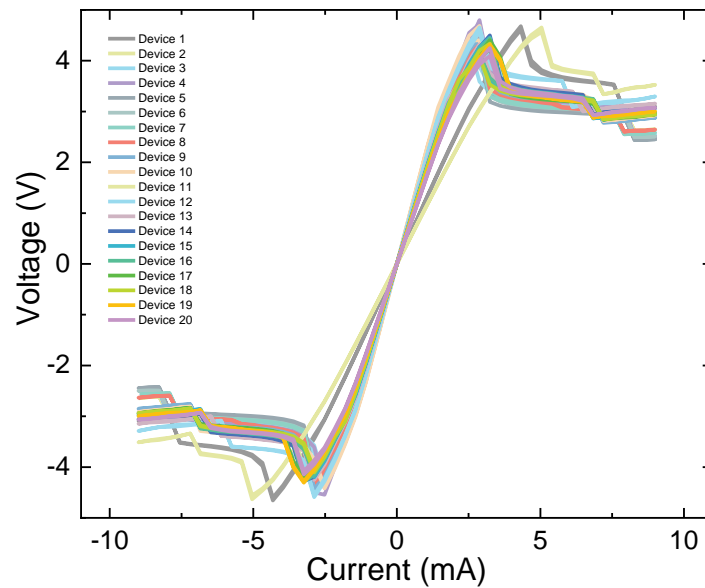


Fig A1. **I-V measurement from 20 VO₂ devices.** I-V measurement (current is varied while measuring voltage) of 20 VO₂ devices ($3 \times 3 \mu\text{m}^2$).

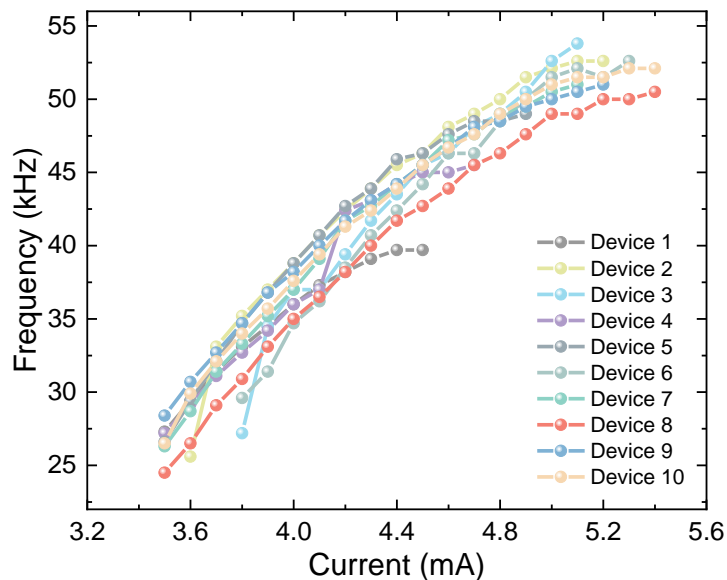


Fig A2. **I-f measurement from 10 VO₂ devices.** I-f measurement (current is varied while measuring oscillation frequency) of 10 VO₂ devices ($3 \times 3 \mu\text{m}^2$).

Finite element simulations of the thermal coupling between VO₂ devices

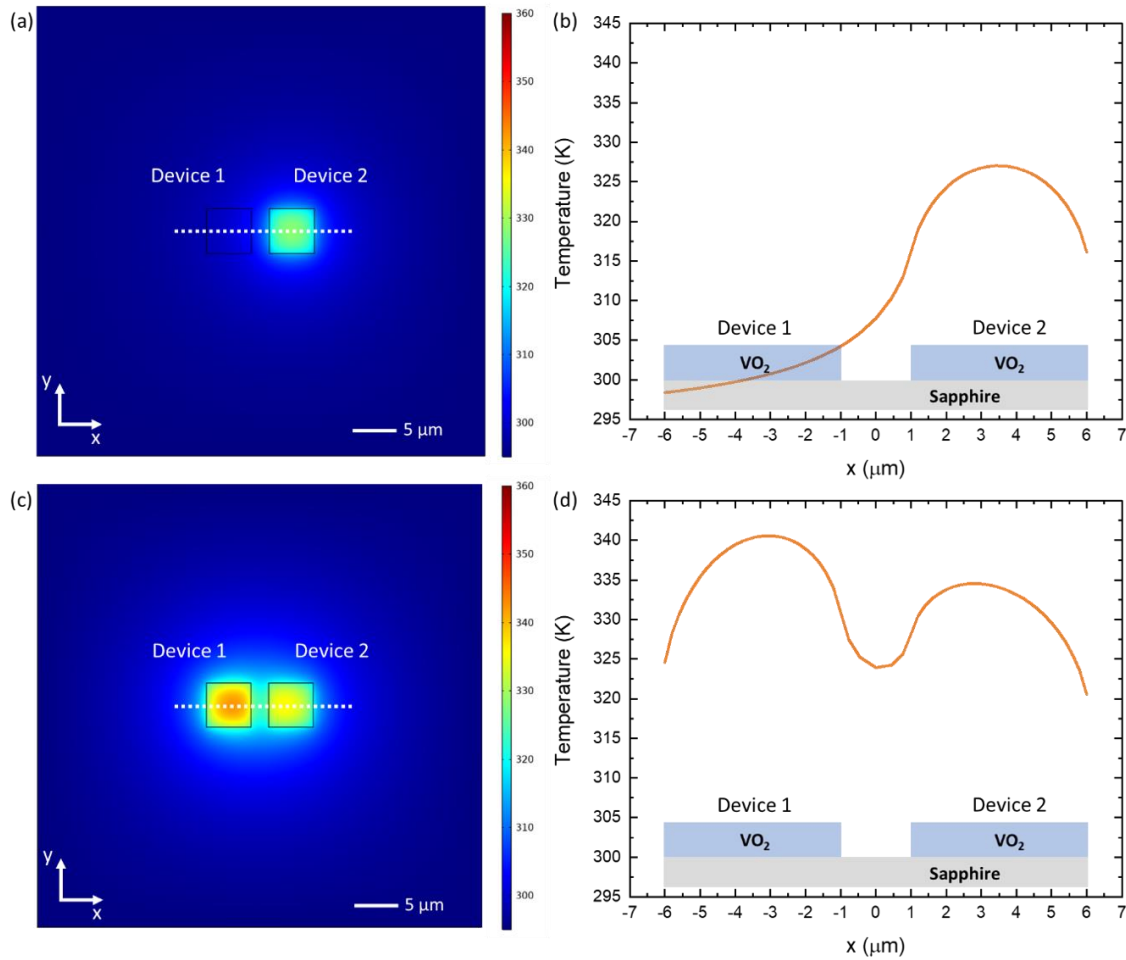


Fig A3. **Simulation of one VO₂ device in its sub-threshold transition state that is triggered to oscillate by a neighboring oscillating VO₂ device at a 2 μm spacing.** Temperature distribution of two VO₂ devices. **a**, Device 1 (5 μm × 5 μm × 30 nm) is supplied with 0 mA current (no oscillation), while device 2 (5 μm × 5 μm × 30 nm) is supplied with 2.3 mA current (sub-threshold transition state) at 295 K. Black squares correspond to the VO₂ devices. **b**, Temperature distribution versus x-axis (dashed line) in case **a**. When device 1 is turned off, the temperature of device 2 is ~327 K that is lower than the phase oscillation temperature range (330 - 360 K). **c**, Device 1 is supplied with 2.8 mA current (stable oscillation state), while device 2 is supplied with 2.3 mA current (sub-threshold transition state) at 295 K. **d**, Temperature distribution versus x-axis (dash line) in case **c**. Simulation shows that, due to the heat dissipated from device 1, the temperature of device 2 (334 K) has been raised to the phase oscillation temperature range (330 - 360 K). Data from [121].

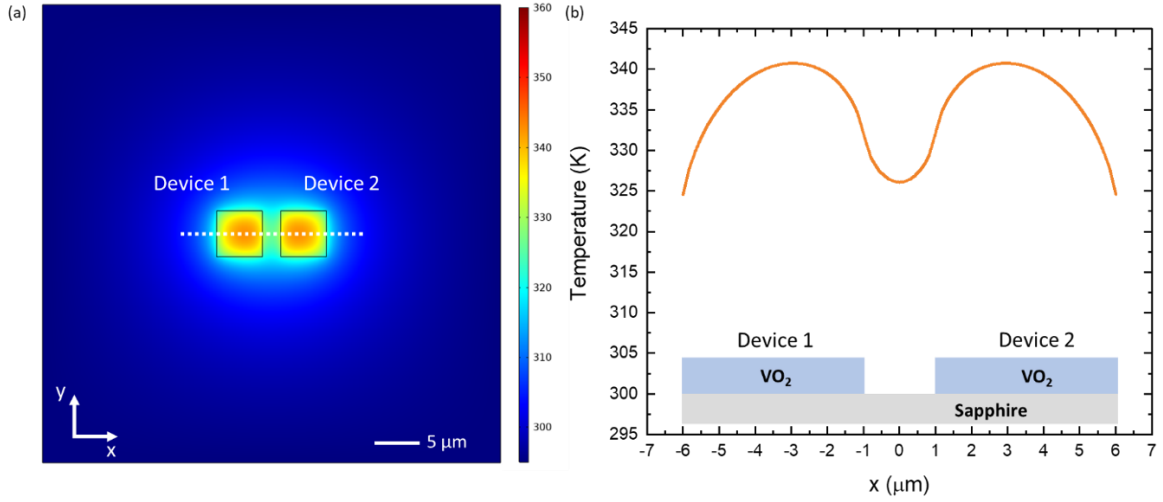


Fig A4. Simulation of two VO₂ devices in a stable oscillation state. **a**, Temperature distribution of two VO₂ devices (both 5 μm × 5 μm × 30 nm, with 2 μm spacing) when they are each supplied with 2.8 mA current ($I_1 = I_2$) at 295 K. Black squares correspond to the VO₂ devices. **b**, Temperature distribution versus x-axis (dash line). When both devices are in a stable oscillation state, their temperature (340.5 K) stays within the phase oscillation temperature range (330 - 360 K). Data from [121].

To study the steady effect of Joule heating, we numerically simulated the temperature distribution of a set of VO₂ devices each with dimensions of $w \times w \times t$. Here only $t = 30$ nm is considered. The VO₂ devices were placed on a sapphire (Al₂O₃) substrate that had the dimensions of 50 μm (length) × 50 μm (width) × 30 μm (thickness). The bottom and edges of the substrate were fixed at a constant temperature of 295 K. Only heat transfer between the sapphire and the VO₂ devices is considered. The steady-state heat transfer was modelled with:

$$-\nabla \cdot (\kappa \nabla T) = Q$$

Where κ , T , Q are the thermal conductivity, temperature, and heat density, respectively. The liner relationship between the power consumption of the entire device P and device width w can be solved from the above equation as:

$$P \propto 4\pi \cdot \Delta T \cdot \kappa \cdot w$$

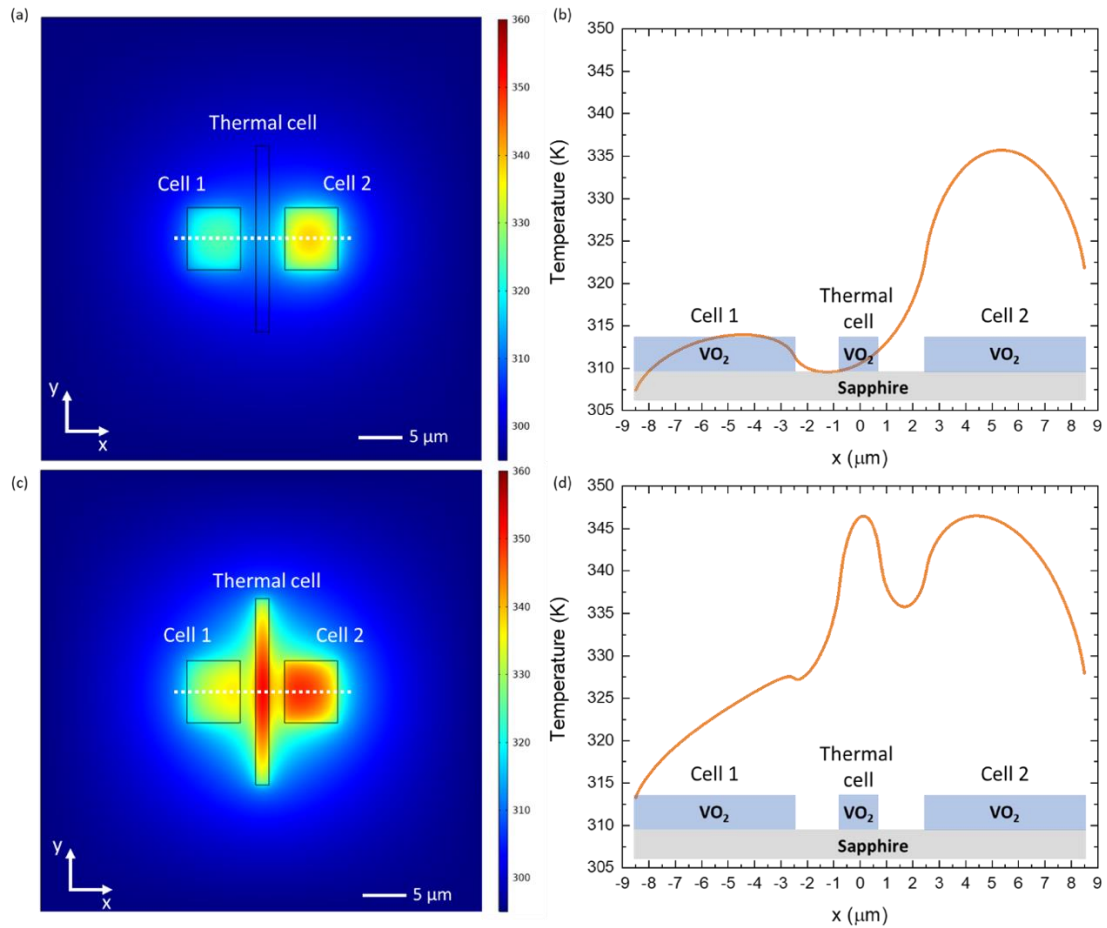


Fig A5. Simulation of VO₂ neuron firing mode 3. Temperature distribution of two VO₂ devices (with 5 μm spacing) and thermal cell. **a**, Device 1 (7 μm × 6 μm × 30 nm) is supplied with 1.7 mA current (no oscillation), while device 2 (7 μm × 6 μm × 30 nm) is supplied with 4 mA current (stable oscillation state) at 295 K. The thermal cell (21 μm × 1.5 μm × 30 nm) is off ($I_{cell} = 0$). Black squares correspond to the VO₂ devices and thermal cell. **b**, Temperature distribution versus x-axis (dash line) in case **a**. When the thermal cell is off, the temperature of device 1 (around 314 K) is lower than the phase oscillation range (330 - 360 K). **c**, Device 1 is supplied with 1.7 mA current, while device 2 is supplied with 2.3 mA current at 295 K. The thermal cell is on ($I_{cell} = 2.3$ mA). **d**, Temperature distribution versus x-axis (dash line) in case **c**. Simulation shows due to the heat dissipated from thermal cell, the temperature of device 2 (336 K) has been raised to the phase oscillation temperature range (330 - 360 K). Data from [121].

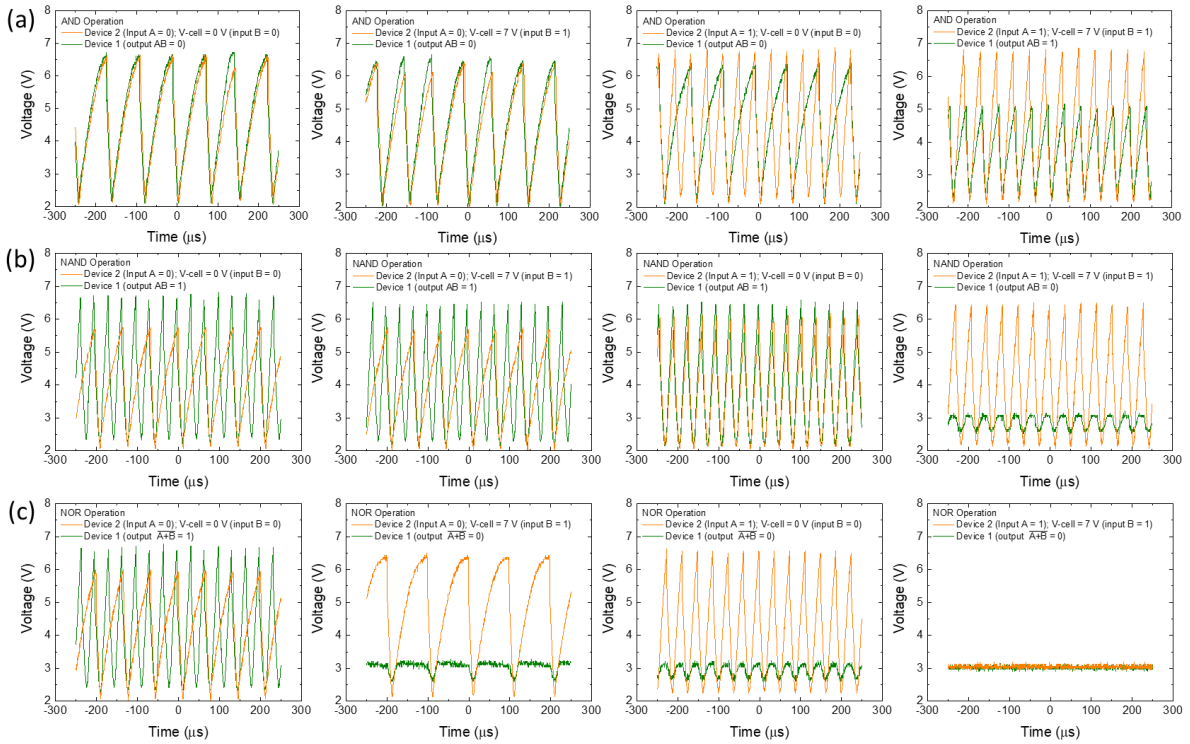


Fig A6. Output waveforms of Boolean logic gates. a, AND gate operation. b, NAND gate operation. c, NOR gate operation. Data from [121].

Cascade synchronization among VO₂ oscillators and the thermal cell

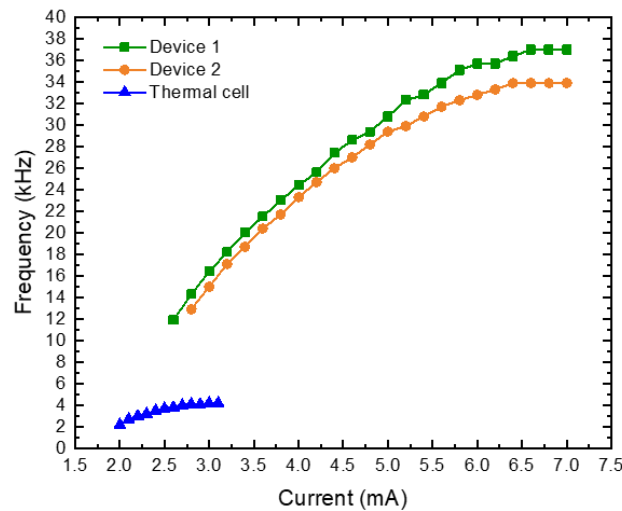


Fig A7. Oscillation frequency as a function of applied d.c. current (I - f). Device 1 (VO₂ cell 2, $7 \times 6 \mu\text{m}^2$) shown as green line, device 2 (VO₂ cell 1, $7 \times 6 \mu\text{m}^2$) shown as orange line and thermal cell ($1.5 \times 21 \mu\text{m}^2$) shown as blue line. Data from [121].

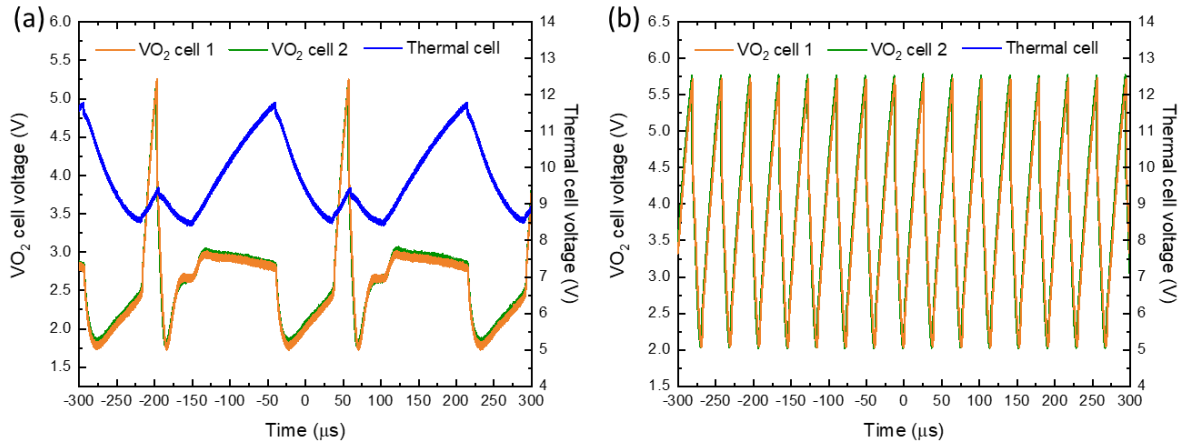


Fig A8. **VO₂ neuron firing mode 1.** **a**, Spiking neuron firing mode 1 at $I_1 = 4$ mA (supply current of VO₂ cell 1), $I_2 = 4$ mA (supply current of VO₂ cell 2) and $I_{cell} = 2.3$ mA (supply current of thermal cell). **b**, $I_1 = 4$ mA, $I_2 = 4$ mA and $I_{cell} = 0$ mA. Data from [121].

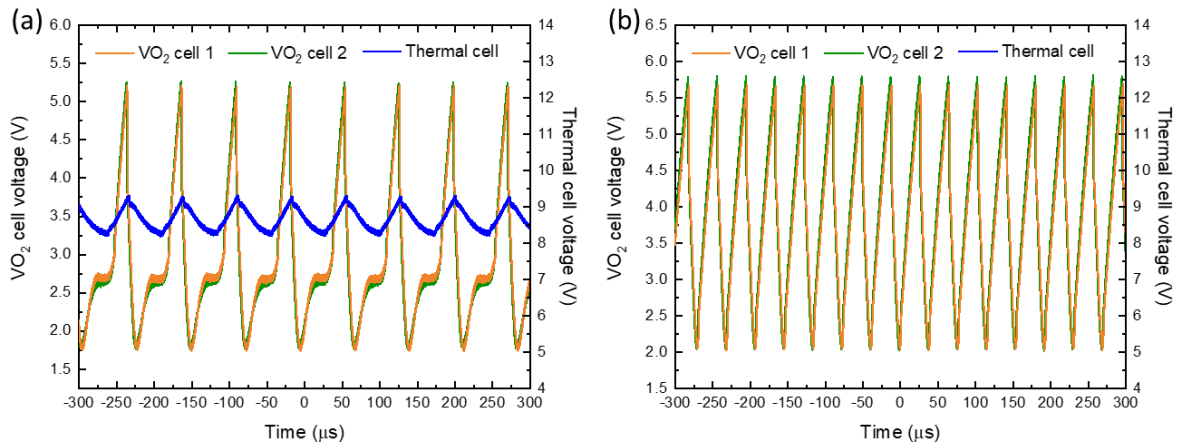


Fig A9. **VO₂ neuron firing mode 2.** **a**, Spiking neuron firing mode 2 at $I_1 = 3.9$ mA (supply current of VO₂ cell 1), $I_2 = 4$ mA (supply current of VO₂ cell 2) and $I_{cell} = 2.3$ mA (supply current of thermal cell). **b**, $I_1 = 3.9$ mA, $I_2 = 4$ mA and $I_{cell} = 0$ mA. Data from [121].

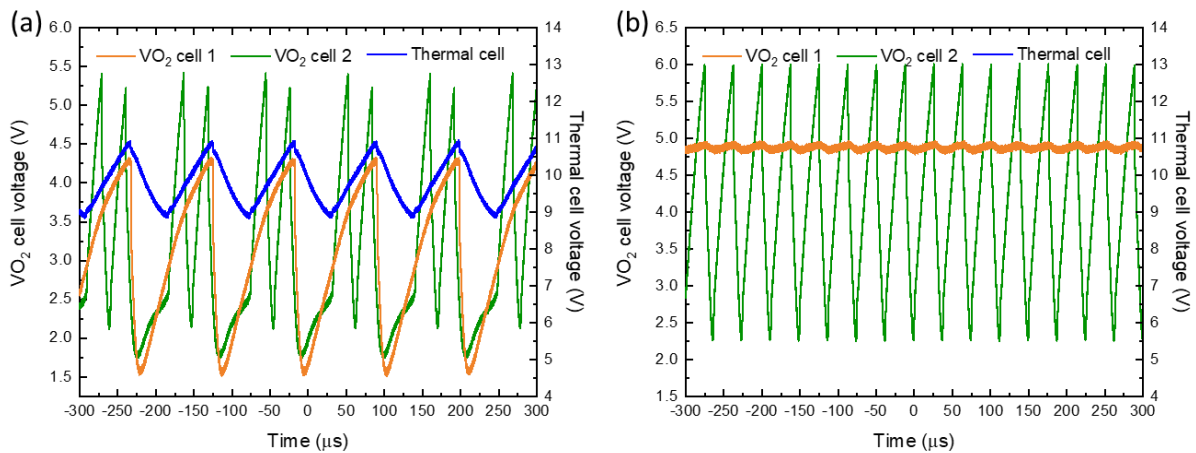


Fig A10. **VO₂ neuron firing mode 3.** **a**, Spiking neuron firing mode 3 at $I_1 = 1.7$ mA (supply current of VO₂ cell 1), $I_2 = 4$ mA (supply current of VO₂ cell 2) and $I_{cell} = 2.3$ mA (supply current of thermal cell). **b**, $I_1 = 1.7$ mA, $I_2 = 4$ mA and $I_{cell} = 0$ mA. Data from [121].

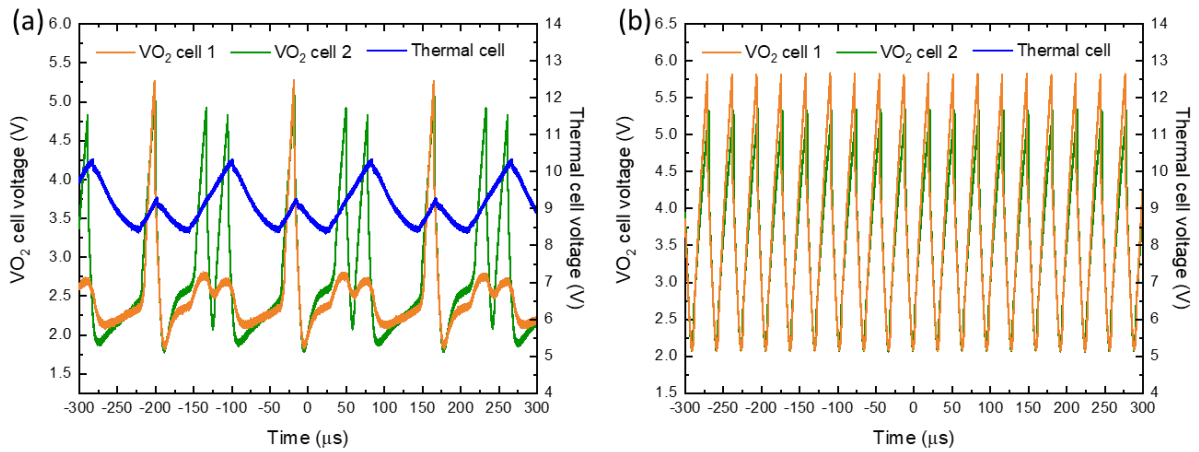


Fig A11. **VO₂ neuron firing mode 4.** **a**, Spiking neuron firing mode 4 at $I_1 = 5.2$ mA (supply current of VO₂ cell 1), $I_2 = 4$ mA (supply current of VO₂ cell 2) and $I_{cell} = 2.3$ mA (supply current of thermal cell). **b**, $I_1 = 5.2$ mA, $I_2 = 4$ mA and $I_{cell} = 0$ mA. Data from [121].

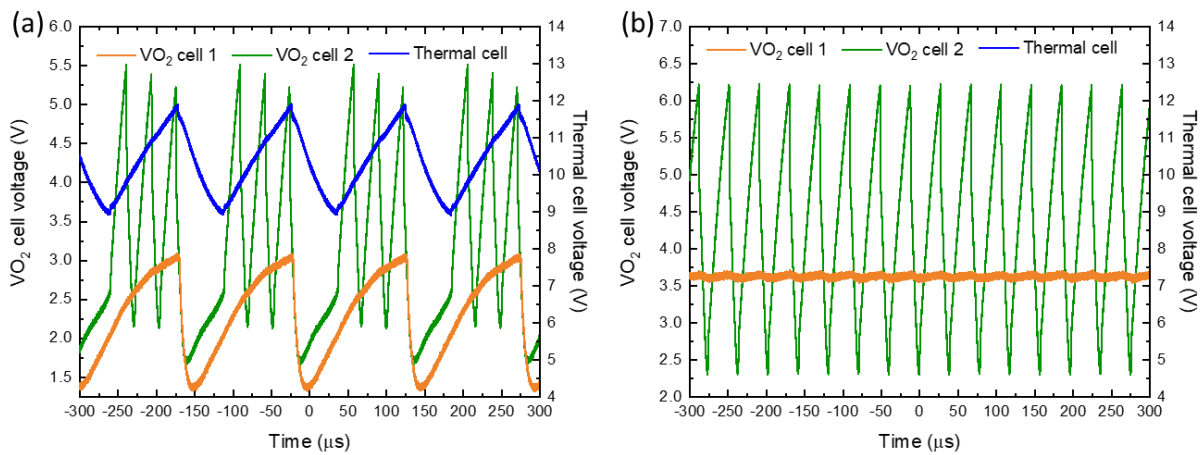


Fig A12. **VO₂ neuron firing mode 5.** **a**, Spiking neuron firing mode 5 at $I_1 = 1$ mA (supply current of VO₂ cell 1), $I_2 = 4$ mA (supply current of VO₂ cell 2) and $I_{cell} = 2.3$ mA (supply current of thermal cell). **b**, $I_1 = 1$ mA, $I_2 = 4$ mA and $I_{cell} = 0$ mA. Data from [121].

Acknowledgements

Firstly, I would like to express my most sincere gratefulness to my supervisor Prof. Dr. Stuart S. P. Parkin! I want to thank Stuart for offering me the freedom to pursue my PhD project on neuromorphic computing. During the research phase, I very enjoyed the discussion with him and has received a lot of inspiration, brand new ideas/concepts, and constructive advices from him. Stuart's enthusiasm and support for my new findings has made it possible to go for high-impact publication in a short time. Furthermore, Stuart's positive attitude towards failures in experiments has encouraged me to build up a stronger mindset when dealing with obstacles and problems in my work and personal life.

Secondly, special thanks to Dr. Jaechun Jeon and Dr. Yuliang Chen! Thanks to Jaechun, we have a 24/7 working scia system. He has prepared the multi-probe station with very good condition and LabVIEW programs for me to test my devices. And I would like to express my thanks to him for correcting my thesis. Yuliang assisted me to grow very nice VO₂ samples at the beginning of the project with his precious experience, which has saved me a lot of time for developing the technology. I would like to express my appreciation to both Jaechun and Yuliang for spending much time on fruitful discussion with me. Together, we managed to make achievements efficiently.

Thirdly, I would like to thank all employees and fellow-students at the Max Planck Institute of Microstructure Physics for creating a nice working environment. As one of the initiators of the PhD Committee, I want to express my thanks to my colleagues for organizing scientific/social events together, and the effort to improve the well-being of PhD students in our institute.

Last but not least, I want to thank my girlfriend Meiying for her support and accompany during my PhD. I want to thank my parents for raising me to be an independent and resilient person in the face of uncertainties, for their unwavering support for my education over the years, and for enabling my living and studies in Germany.

Academic Curriculum Vitae

First Name: Guanmin
Family Name: Li
Gender: Male
Nationality: Chinese

Education

May 2022 – September 2025 Max Planck Institute of Microstructure Physics (Germany)

- Doctor of Engineering (Supervisor: Prof. Dr. Stuart S. P. Parkin)
- PhD Thesis: Oscillatory Computational Networks based on Coupled VO₂ Oscillators via Tunable Thermal Triggering
- Cum Laude 1.0

September 2019 – March 2022 RWTH Aachen University (Germany)

- Master of Science in Physics, major in Nanoelectronics
- Master Thesis: Structural and Optical Investigations on textured Lead Selenide Thin Films (Supervisor: Prof. Dr. Matthias Wuttig)
- Overall grade 1,4 (Master thesis 1,0)

September 2015 - June 2019 Jilin University (China)

- Bachelor of Science in Physics
- Bachelor thesis: Improvement of Target Identification and Positioning Accuracy for the Binocular Stereo Vision System based on Convolutional Neural Network (Supervisor: Prof. Dr. Zhongchang Zhuo)
- GPA: 3.31/4.0

Ort, Datum

Guanmin Li

Publications and Conference Contributions

Publications

Guan, Y., Han, H., Li, F., **Li, G.**, Parkin, S. S. P., Ionic Gating for Tuning Electronic and Magnetic Properties. *Annual Review of Materials Research* 53, 25 - 51 (2023).

Li, G., Wang, Z., Jeon, J.C., Parkin, S. S. P., Electronic phase oscillation based logic devices via tunable thermal coupling gate. 1401-6720-WT / 24/001, issued on January 29th, 2024.

Li, G., Wang, Z., Chen, Y., Jeon, J.C., Parkin, S. S. P., Computational elements based on coupled VO₂ oscillators via tunable thermal triggering. *Nature Communications* 15, 5820 (2024).

Conference contributions

Li, G., Wang, Z., Chen, Y., Jeon, J.C., Parkin, S. S. P.: Computational elements based on coupled VO₂ oscillators via tunable thermal triggering. DPG-Frühjahrstagung, Berlin, 2024 (poster).

Li, G., Wang, Z., Chen, Y., Jeon, J.C., Parkin, S. S. P.: Spiking neurons based on coupled VO₂ oscillators via tunable thermal triggering. ICNCE, Aachen, 2024 (poster).

Li, G., Chen, Y., Jeon, J.C., Parkin, S. S. P.: Spiking neurons based on coupled VO₂ oscillators via tunable thermal triggering. Nature Conference, Beijing, 2024 (poster).

Eidesstattliche Erklärung / Declaration under Oath

Ich erkläre an Eides statt, dass ich die Arbeit mit dem Titel: **Oscillatory Computational Networks based on Coupled VO₂ Oscillators via Tunable Thermal Triggering** selbstständig und ohne fremde Hilfe verfasst, keine anderen als die von mir angegebenen Quellen und Hilfsmittel benutzt und die den benutzten Werken wörtlich oder inhaltlich entnommenen Stellen als solche kenntlich gemacht habe.

I declare under penalty of perjury that this thesis with the title: **Oscillatory Computational Networks based on Coupled VO₂ Oscillators via Tunable Thermal Triggering** is my own work entirely and has been written without any help from other people. I used only the sources mentioned and included all the citations correctly both in word or content.

Ort, Datum / Place, Date

Guanmin Li